University Bremen

Doctoral Thesis

Influence of the spin on the radiation of a spinning emitter orbiting compact objects

---

Author:
Jan-Menno Memmen

First reviewer:
PD. Dr. Volker Perlick
Second reviewer:
Prof. Dr. Domenico Giulini

Dem Fachbereich Physik und Elektrotechnik der Universität Bremen
zur Erlangung des akademischen Grades
Doktor der Naturwissenschaften (Dr. rer. nat.)

Submitted: Bremen, July 6, 2023
Colloqium: Bremen, October 10, 2023

"*All you really need to know for the moment is that the universe is a lot more complicated than you might think, even if you start from a position of thinking it's pretty damn complicated in the first place.*"

Douglas Adams, The Hitchhiker's Guide to the Galaxy

"*The most important step a man can take. It's not the first one, is it? It's the next one. Always the next step, Dalinar.*"

Brandon Sanderson, Oathbringer

"*How wonderful that we have met with a paradox. Now we have some hope of making progress.*"

Niels Bohr

UNIVERSITY BREMEN

Abstract

Department 01: Physics / Electrical Engineering

Doktor der Naturwissenschaften (Dr. rer. nat.)

Influence of the spin on the radiation of a spinning emitter orbiting compact objects

by Jan-Menno Memmen

In this thesis, I develop a theoretical description of the radiation of an extended, spinning light source on a circular orbit in the symmetry plane of a stationary, axially symmetric and asymptotically flat spacetime. The light source is assumed to be a test particle, in order to neglect its gravitational influence on the background spacetime. I derive the necessary transformations for a reference frame that is at rest on the surface of the rotating emitter, and link the emission angles, relative to the surface of the emitter, to the constants of motion of the light ray. Two emitter geometries are considered: a sphere and a Maclaurin spheroid, which is flattened as a result of its spin. In particular, I apply this theory to an emitter in orbit around a Schwarzschild object, as well as an emitter orbiting a Kerr black hole. In this context, I investigate the influence of the emitter spin on the observables, specifically the polarization plane, redshift and flux, as well as the influence of the black hole rotation. Notably, the position of the emitter orbit where the maximum flux is observed depends on the spin, and non-monotony is observed in the amount of observed flux, varying the spin of the emitter. This theory may find application in describing the emissions of spinning hot spots in accretion disks or neutron stars.

Acknowledgements

First, special thanks and gratitude has to be dedicated to my supervisor Volker Perlick. Your seemingly endless source of knowledge and overwhelming level of understanding in this field of science is inspiring and supported my own journey through the landscape that is theoretical physics. It is safe to say that without your help, this thesis would not have been possible.

To my colleagues and collaborators, in particular Oleg Tsupko, Felix Willenborg, Jan Scheumann, Jan Hackstein, Marian Cepok, Altin Shala, Dennis Philipp, Eva Hackmann, Christian Pfeifer: even in pandemic conditions, I want to appreciate the possibility of working with you! I am grateful for your support, in the field of physics and beyond, and for the open and warm, welcoming atmosphere you create.

To my parents, Marianne and Rolf, as well as my siblings, Hanno and Talea: none of this would be possible without the unconditional support along the journey of physics. I am forever grateful.

To Carmen: your constant reassurance and belief, even in times where I did not believe myself, helped me tremendously. You are my backbone and my biggest supporter, and I cannot express in words how much you mean to me.

To all of my friends: it was fun to share this experience with you! To Franzi, for transforming the work-at-home experience into a co-working-at-home one; to Piwo, for extending your play beyond your turn; to Ann-Marie, for the in-depth help on the English language; to Jonas, Jenny, Clara and all the others: for supporting me all the way.

The financial support by the DFG within the Project "Propagation of light signals near a black hole surrounded by a plasma" is gratefully acknowledged. Furthermore, I want to thank the project partners in Oleg Tsupko and Gennady Bisnovatyi-Kogan for their support and insight during the the first half of this PhD project, especially in the background of ongoing conflicts and its influence on the publishing process.

Contents

List of Figures

List of Abbreviations

MPD	**M**athisson-**P**apapetrou-**D**ixon equations
ZAMO	**Z**ero **a**ngular **m**omentum **o**server
LNRF	**L**ocal **n**on-**r**otating **f**rame
COM	**C**entre **o**f **m**ass (reference frame)
COMOM	**C**entre **o**f **mom**entum (reference frame)
SRF	**S**urface **r**est **f**rame

Chapter 1

Introduction

Whereas a few decades ago, black holes were considered merely hypothetical in nature, results allowed by Einsteins' theory of gravity, there is now strong observational evidence for their existence in this universe. The information of these heavy objects is gathered mainly by studying the effects of their strong gravitational influence on light signals in the vicinity of the black hole. Since the end of the previous millennium, observations produced increasing evidence of supermassive black holes at the centre of galaxies. This evidence was mainly based on infrared observations of stars in orbit close to the gravitational centre of our galaxy, see Ghez [1] and Gillisen [2]. This research effort culminated in the first image of a black hole, in particular the supermassive black hole in the centre of galaxy M87, by the Event Horizon Telescope Collaboration in 2019 [3]. The EHT is an international collaboration of synchronised radio observatories, investigating the light sources in the millimeter and submillimeter regimes. Additionally, the EHT produced images of SgrA*, the supermassive black hole in the centre of our galaxy [4]. Evidently, it becomes important to study the effect of strong gravitational fields on these sources of radiation.

One of the most fundamental concepts of physics is the conservation of angular momentum. Physical rotating objects, that decrease in size, e.g. stars under gravitational collapse, retain their angular momentum and thereby increase their angular velocity. Fast rotating, small and compact astrophysical objects may form the basis for realizations of this thesis in nature. Particularly, one may consider rotating hot spots in accretion disks around aforementioned black holes or neutron stars as possible applications.

Accretion disks form as matter around a compact object accelerates and falls towards the source of gravity, and the energy released in this process is received as light by terrestrial observers, mostly in the radio range. For a thorough discussion on this topic, see e.g. [5]. These disks, as sources of light, give insight on the properties of the central object that creates the gravitational field. Hot spots in these accretion disks are defined by their increased level of emissions, first theoretically discussed by Abramowicz et al. [6] and Mangalam and Wiita [7]. In principle, these hot spots may have a non-vanishing spin, as they are postulated to be formed via angular momentum conservation and the interaction with the surrounding magnetic field. They are a defining feature of accretion disks, and the increased emissions of the hot spots make them prime targets for studying the physics of strong gravity. The theoretical model of spinning light sources may be applied to study the effects of the spin and its origins for hot spots near strong sources of gravity, e.g. black holes.

Neutron stars are the remains of a core collapse of heavy stars between around 10 and 25 solar masses, see e.g. [8]. Neutron stars are extremely dense, having a mass of a few solar masses, while having only a size of only a few 10 kilometers. They were first postulated by Baade and Zwicky in 1934 [9], and the first evidence seen by Hewish and Bell in 1967 [10]. A upper limit on the mass of these objects was first introduced by Oppenheimer and Volkoff in 1939 [11]; if the star would pass this limit, it would collapse into a black hole. The theoretical

limit was placed approximately between 1.5 and 3 solar masses in 1996 [12], where current studies set this limit between 2 and 2.16 solar masses [13].

As a result of the conservation of angular momentum, these objects spin inherently fast, up to a quarter of the speed of light [14]. One mission dedicated to studying neutron stars is the Neutron star Interior Composition Explorer (NICER) mission, deployed by NASA [15]. Among other subjects, this mission aims to study the Xray emission and the polarization of said emissions of these dense objects. In particular, Bogdanov et al. [16, 17] created a model to describe the surface of fast spinning neutron stars. In contrast to the theory introduced in this thesis, the model has the spinning object as the source of gravity, and the main objective is to study the effect of the emitter gravity on the light that is observed. The observer is placed at infinity, and the gravitational field is modeled to be static. Therefore, the paper may be seen as a preparation to extend the theory, that is introduced in this thesis, to further include the effect of the emitter gravity on the light coming from a spinning light source in orbit around a central source of gravity.

From a theoretical point of view, radiation of light sources orbiting a black hole is usually calculated while neglecting the effect of the self-rotation, the so-called spin, of the emitter. To the best of our knowledge, the spin of the light source and its direct effect on the observed radiation is yet to be described theoretically in its entirety. Therefore, the goal of this thesis is to develop a theoretical description of spinning light sources in orbit around compact objects and the influence of their spin on the observed radiation.

More specifically, this thesis aims to establish a theory for strong sources of gravity, and then studying the effect of the spin on the radiation observed for specific examples of compact objects. For the simplest case of a light source in geodesic motion, the emitter cannot be closer to the source of gravity than the innermost stable circular orbit (ISCO). For non-spinning test-particles in Schwarzschild spacetime, which may be used to describe non-rotating black holes, the ISCO is well-known and lies at $r = 6M$, first found by Kaplan [18]. If the source of gravity, e.g. the black hole, is assumed to be rotating as well, one may consider the Kerr spacetime for describing its gravitational field. For this solution to Einsteins vacuum field equations, the position of the ISCO for non-spinning test particles lies at radii smaller than $6M$ for co-rotating orbits, reaching the horizon at $r = M$ for extreme Kerr solutions with $a/M = 1$, and increases beyond $6M$ for a counter-rotating orbit, reaching $9M$ in the extreme case [19, 20]. If the emitter is spinning and orbits in the equatorial plane, the distance of these orbits were determined by Jefremov, Tsupko and Bisnovatyi-Kogan [21], for the case where the spin axis is parallel or anti-parallel to the orbit angular momentum.

This thesis aims to develop a theoretical model of a spinning light source in the symmetry plane of general compact objects, establishing the notion of observables in this case, and studying the influence on the spin on these observables. In this context, this thesis is structured as follows:

The first chapter introduces the equations of motions for the orbit of a spinning test-particle, the Mathisson-Papapetrou-Dixon equations. Following a brief overview on this topic, the importance of the choice and influence of the supplementary condition on the trajectory of the test particle are discussed.

The second chapter then develops the theoretical description of a spinning light source in the symmetry plane of any compact that is axisymmetric, stationary and asymptotically flat. Specifically, the surface rest frame is established. Additionally, the observables, namely the polarization plane, redshift and flux, associated with the aforementioned light rays, are described. The chapter ends with the discussion on the numerical procedure in calculating the light ray that connects emitter and observer.

The third chapter deals with the geometry of the emitter. In the context of this thesis, two different geometries are discussed: a rigidly rotating sphere, and a rigidly rotating spheroid, described by the Maclaurin spheroid. In particular, the velocities of the surface elements and other properties implied are studied.

The fourth chapter applies the theory of spinning light sources to the Schwarzschild spacetime, a static and spherically symmetric solution to the Einstein vacuum field equations. After a brief introduction on this solution, the surface rest frame is established for an emitter orbiting a Schwarzschild object in the symmetry plane. The subsequent part of this chapter studies the effect of the spin on the different observables described in chapter 2 for a fixed configuration of emitter and observer.

The fifth chapter generalizes the source of gravity even further and applies the theory to the Kerr spacetime, which describes the exterior gravitational field of a rotating black hole. Structured similarly, this chapter first gives a brief overview over the properties of this solution, and then develops the surface rest frame for a spinning emitter in circular orbit around a Kerr black hole. Finally, an extended study of the aforementioned observables and the influence of the emitter spin on them concludes this section.

The last chapter is dedicated to summarizing the results of this thesis and giving an outlook about possible extensions and further studies regarding this topic.

In the context of this thesis, the metric is expressed as g with the convention of signature as $(-,\ +,\ +,\ +)$. Furthermore, all Greek indices run from 0 to 3 and Einsteins' summation convention is complied. Additionally, geometrized units, i.e. $c = G = 1$, are adopted. In order to differentiate the reference frames, each frame will be denoted with differing brackets.

Chapter 2

Mathisson–Papapetrou–Dixon equations

In this chapter, the theory on spinning test particles, the Mathisson-Papapetrou-Dixon equations, is discussed. First, a brief overview is given on the history and general approach to the equations of motion, and then the importance and influence of the choice of spin supplementary condition on the trajectory of the spinning test body is discussed. A thorough description may be found in e.g. [22, 23, 24].

2.1 General approach

In order to describe the motion of extended bodies, the Einstein field equations

$$G_{\mu\nu} = 8\pi T_{\mu\nu} \tag{2.1}$$

may be used, first introduced by Einstein, Infeld and Hoffmann [25]. Here, $G_{\mu\nu}$ is the Einstein tensor and $T^{\nu\mu}$ is the energy-momentum tensor describing the physical properties of the test body.

For studying the equations of motion of test particles, there exists a more suitable approach, developed by Fock [26] and Papapetrou [27]. In this context, the conservation law

$$\nabla_\nu T^{\nu\mu} = 0 \tag{2.2}$$

is used to determine the equations of motion instead. This conservation law follows directly from the field equations in Eq. (2.1), as well as from the second Bianchi identities

$$\nabla_\nu G^{\mu\nu} = 0\,. \tag{2.3}$$

The method to find the equations of motion by Papapetrou involves choosing a representative world line in the body, taking all multipole moments of Eq. (2.2) in the vicinity of that world line into account. Additionally, the n-pole particle approximation is used; if one assumes that the body is sufficiently small, all multipole moments of order $n + 1$ and higher shall be neglected. For a monopole particle, the motion of the test particle is described by the geodesic equation. In this regard, when spinning particles are of interest, all moments higher than the dipole moment are neglected, resulting in the equations of motion for a pole-dipole particle derived by Papapetrou.

2.2 Supplementary conditions

Up to this point, a world line through a distinguished point of the body is yet to be chosen; this choice is in general arbitrary. As a consequence, it becomes necessary to properly and uniquely specify a world line through the body; if not uniquely selected, the motion of the desired point of the body may not be determined fully. Thus, a supplementary condition, specifying the world line, is needed to determine the motion.

There are different kinds of supplementary conditions that have proven to be particularly convenient in describing a spinning test body in this pole-dipole test particle approximation. Specifically, the following two conditions are used most often in literature:

(i) Mathisson [28] and Pirani [29] (originally: Frenkel [30]) used the following supplementary condition, the so-called Mathisson-Pirani-Frenkel condition:

$$V_\mu S^{\mu\nu} = 0 \,, \tag{2.4}$$

where V^μ is the tangent vector to the world line Z^μ and $S^{\mu\nu}$ is the spin tensor. This fixes the reference world line to be the body's centre of mass as measured in the rest frame moving with four-velocity V^μ. However, the world line that is defined by this supplementary condition is not unique. Thus, special care needs to be taken when choosing such a world line, as, in general, the trajectory of spinning bodies that emerge while using this condition is represented by helical motions.

(ii) Dixon [23, 31, 32] and Tulczyjew [33] introduced another supplementary condition to fix the center of mass world line:

$$P_\mu S^{\mu\nu} = 0 \,. \tag{2.5}$$

This supplementary condition is frequently referred to as the Tulczjew-Dixon condition. Here, P_μ is the four-momentum of the object, and $S^{\mu\nu}$ is the spin tensor describing the spin of the object. This fixes the reference world line of the body's centre of mass as measured by an observer moving with four-velocity $U^\nu = P^\nu/\mu$, where μ is the mass of the object. Unless the spacetime is flat, this world line generally does not coincide with the centre of gravity, or proper centre of mass as defined by Moeller [34].

Throughout this thesis, the Tulczjew-Dixon condition will be used, as its unique choice of world line simplifies the description of the centre of mass reference frame, and also leads to an explicit expression of the four velocity V^μ in terms of the momentum p^μ, spin tensor $S^{\mu\nu}$ and world line Z^μ. Following Wald [22] and Dixon [32], this world line will be referred to as the centre of mass world line throughout this thesis.

For any choice of world line through the test body, one can derive the motion of a spinning test body in the procedure described before; this leads to the Mathisson-Papapetrou-Dixon equations:

$$\frac{\mathrm{D}}{\mathrm{D}\sigma} P^\mu = -\frac{1}{2} R^\mu{}_{\nu\rho\lambda} V^\nu S^{\rho\lambda} \tag{2.6}$$

$$\frac{\mathrm{D}}{\mathrm{D}\sigma} S^{\mu\nu} = P^\nu V^\mu - P^\mu V^\nu \,, \tag{2.7}$$

where $\mathrm{D}/\mathrm{D}\sigma$ denotes the covariant derivative along the world line,

$$R^\mu{}_{\nu\rho\lambda} = \partial_\rho \Gamma^\mu_{\nu\lambda} - \partial_\lambda \Gamma^\mu_{\nu\rho} + \Gamma^\mu_{\tau\rho}\Gamma^\tau_{\nu\lambda} - \Gamma^\mu_{\tau\lambda}\Gamma^\tau_{\nu\rho} \tag{2.8}$$

is the Riemann tensor and V^ν is the tangent vector to the world line.

Equations Eq. (2.6) and (2.7), together with the supplementary condition in Eq. (2.5), determine the motion of the spinning test body.

By contracting $S_{\mu\nu}$ in Eq. (2.7) and using Eq. (2.5), it is possible to find that

$$\hat{S}^2 = \frac{1}{2} S_{\mu\nu} S^{\mu\nu} \tag{2.9}$$

is conserved along the world line. In this context, $\hat{S}$ is the magnitude of the spin of the test particle. Another constant of motion, for the Tulcziew-Dixon condition, is the mass of the object μ, i.e.

$$\mu^2 = P_\nu P^\nu \ . \tag{2.10}$$

Additionally, the general definition of the specific spin vector will be of importance in the exact calculations of the trajectory of the spinning test particle on the equatorial plane of an Schwarzschild or Kerr object, i.e.

$$S^\nu = -\frac{\epsilon^\nu{}_{\kappa\alpha\beta} P^\kappa S^{\alpha\beta}}{2\mu} \ , \tag{2.11}$$

where $\epsilon^\nu{}_{\kappa\alpha\beta}$ is the four dimensional fully anti-symmetric tensor.

In the context of special relativity, Moeller [34] has shown that a body in self-rotation and mass μ, as well as positive energy density, i.e.

$$T_{\kappa\nu} \xi^\kappa \xi^\nu > 0 \text{ for all timelike vectors } \xi \ , \tag{2.12}$$

has to abide a limit on its scale of geometric extension r_0, as measured in the proper centre of mass reference frame; this limit arises from the fact that the emitters' peripheral velocity is only allowed up to subluminal speed, i.e.

$$r_0 \gtrsim \frac{\hat{S}}{\mu} \ . \tag{2.13}$$

Therefore, in order to describe spinning test bodies that are physically reasonable, one has to rigorously consider the geometrical extension in Eq. (2.13); in particular, this will be discussed in chapter 4.

Since the equations of motion in Eqs. (2.6) and (2.7) are invariant under reparametrization of the orbital parameter σ, one may choose σ such that

$$P^\nu V_\nu = -\mu \ . \tag{2.14}$$

There are some important remarks to be made about the relation between the tangent of the world line V^ν and the normalized four-momentum $U^\nu := P^\nu/\mu$. In general, if the test particle is spinning, U^ν and V^ν are not parallel anymore, see e.g. Ehlers and Rudolph [24]. However, in a space-time of constant curvature, e.g. flat space-time, the normalized four-momentum and the four-velocity are collinear. In this thesis, spinning emitters are discussed in curved spacetimes, specifically Schwarzschild and Kerr spacetimes, thus the non-parallelism of the two quantities is of importance. This will be discussed in detail in 3.1.3 for a general compact object that is stationary and axially symmetric, and in 5.2.3 and 6.2.3 for Schwarzschild and Kerr, respectively, as the surface rest frame is defined relative to the centre of momentum.

Chapter 3

Modelling the emission of a spinning light source in circular orbit in the symmetry plane of a compact object

3.1 Theoretical description of the radiation of spinning light sources

In this chapter, a theoretical description of a spinning light source in circular motion around a compact object described by any stationary, axisymmetric, asymptotically flat spacetime is considered. In this case, the metric of such an object can always be written in the form of

$$\mathrm{d}s^2 = -e^{2\nu}\mathrm{d}t^2 + e^{2\psi}(\mathrm{d}\varphi - \omega\mathrm{d}t)^2 + e^{2\mu_1}\mathrm{d}r^2 + e^{2\mu_2}\mathrm{d}\vartheta^2 \,, \tag{3.1}$$

see e.g. [19]. Evidently, if the quantity $\omega \to 0$, the spacetime becomes static, while in general remaining axisymmetric and asymptotically flat.

3.1.1 Static and stationary observers

In general relativity, there are infinitely many possibilities for the choice of coordinates in which to mathematically describe physical laws and quantities. For any stationary, axisymmetric, asymptotically flat spacetime, for which the metric can be written in the form given in Eq. (3.1), it is useful to introduce a set of local observers for which their angular momentum, as measured at infinity, vanishes. Incidentally, such reference frames are called ZAMO (**Z**ero **A**ngular **M**omentum **O**bservers) or LNRF (**L**ocally **N**on-**R**otating **F**rames); see Bardeen [19]. In this thesis, the ZAMO acronym is used to describe these observers. Naturally, if the quantity ω vanishes, the observers become static.

An observer is defined by its orthonormal tetrad, consisting of 4 vectors, that locally represent the set of basis vectors in which the spacetime is flat, i.e. pseudo-euclidean. Mathematically, physical observables are represented by projecting these quantities on the orthonormal tetrad.

The orthonormal tetrad of this frame (and its dual form, see e.g. [35]) is given by

$$\mathbf{e}_{(a)} = e^{\lambda}_{(a)}\,\partial_\lambda \,, \tag{3.2}$$

$$\mathbf{e}^{(a)} = e^{(a)}_{\lambda}\,\mathrm{d}x^\lambda \,, \tag{3.3}$$

where the tensors take form

$$e^{\lambda}_{(a)} = \begin{pmatrix} e^{-\nu} & 0 & 0 & \omega e^{-\nu} \\ 0 & e^{-\mu_1} & 0 & 0 \\ 0 & 0 & e^{-\mu_2} & 0 \\ 0 & 0 & 0 & e^{-\psi} \end{pmatrix}, \tag{3.4}$$

$$e^{(a)}_{\lambda} = \begin{pmatrix} e^{\nu} & 0 & 0 & 0 \\ 0 & e^{\mu_1} & 0 & 0 \\ 0 & 0 & e^{\mu_2} & 0 \\ -\omega e^{\nu} & 0 & 0 & e^{\psi} \end{pmatrix}. \tag{3.5}$$

Vector components that are expressed in a local stationary reference frame are denoted by round-bracketed latin indices, where $(a) \in \{0, 1, 2, 3\}$.

The components of the tetrad are chosen in such a way that the observer's angular momentum, as measured at infinity, vanishes, and also that the metric in the observer's reference frame is locally flat, i.e.

$$\eta_{(i)(j)} = e^{\mu}_{(i)} e^{\nu}_{(j)}\, g_{\mu\nu}\,, \tag{3.6}$$

where $\eta = \mathrm{diag}(-1,\ 1,\ 1,\ 1)$ is the Minkowski metric.

At any instance of time, the reference frame of any physical observer differs from the ZAMO reference frame only by a Lorentz transformation. Thus, if the relative velocity of another arbitrary observer to the ZAMO reference frame is known, the transformation formulae of special relativity (see e.g. [22] or [36]) can be used to describe such observers. This fact will be abused to describe the reference frame in which the observer is at rest on the surface of the spinning light source. Consequently, the centre of mass (COM) reference frame, which moves with the orbital velocity of the spinning light source around the source of gravity, is established first.

3.1.2 Centre of mass reference frame

In this subsection, the centre of mass reference frame is established. The light source is assumed to be on a circular orbit around the central object, with its four-velocity denoted by V^{ν}. If the light source is spinning, this four-velocity is the tangent to the world line $Z^{\nu}(\sigma)$, established in chapter 2, particularly section 2.2.

The centre of mass reference frame is obtained by a Lorentz transformation that boosts the above introduced ZAMO reference frame with the spin-dependent orbit 3-velocity of the spinning light source, as measured in the ZAMO reference frame. As the light source orbits the source of gravity on a circular orbit, there is only one non-vanishing spatial component of the four-velocity, thus the orbit velocity v can be calculated via

$$v := \frac{V^{(3)}}{V^{(0)}} = \frac{-\omega e^{\nu}\, V^{t} + e^{\psi}\, V^{\varphi}}{e^{\nu}\, V^{t}}\,. \tag{3.7}$$

In particular, it is important to note that $V^{(3)}$ and $V^{(0)}$ are the components of the four-velocity as measured in the ZAMO reference frame, while V^{t} and V^{φ} are its spacetime components.

This four-velocity is consequently dependent on the spin of the object and the background spacetime considered. For two specific cases in Schwarzschild and Kerr spacetimes, the analytic expression of these velocities is given in chapters 5.2.2 and 6.2.2 respectively.

The orthonormal tetrad of this frame, as well as its dual form, is given by the following transformation rule:

$$\mathbf{e}_{[b]} = \Lambda^{(a)}_{[b]}\, \mathbf{e}_{(a)} \,, \tag{3.8}$$

$$\mathbf{e}^{[b]} = \left(\Lambda^{-1}\right)^{[b]}_{(a)}\, \mathbf{e}^{(a)} \,, \tag{3.9}$$

where the Lorentz transformation is given by

$$\Lambda^{(a)}_{[b]} = \begin{pmatrix} \gamma & 0 & 0 & \gamma v \\ 0 & 1 & 0 & 0 \\ 0 & 0 & 1 & 0 \\ \gamma v & 0 & 0 & 1 + \frac{\gamma^2 v^2}{1+\gamma} \end{pmatrix} \tag{3.10}$$

and its inverse

$$\left(\Lambda^{-1}\right)^{[b]}_{(a)} = \begin{pmatrix} \gamma & 0 & 0 & -\gamma v \\ 0 & 1 & 0 & 0 \\ 0 & 0 & 1 & 0 \\ -\gamma v & 0 & 0 & 1 + \frac{\gamma^2 v^2}{1+\gamma} \end{pmatrix} . \tag{3.11}$$

In this context, the gamma-factor γ is defined as $\gamma = \left[1 - v^2\right]^{-1/2}$. Equivalently, for completion purposes, one can give the transformation formulae for the back transformation, i.e. transforming from the COM frame back into the ZAMO reference frame:

$$\mathbf{e}_{(a)} = \left(\Lambda^{-1}\right)^{[b]}_{(a)}\, \mathbf{e}_{[b]} \,, \tag{3.12}$$

$$\mathbf{e}^{(a)} = \Lambda^{(a)}_{[b]}\, \mathbf{e}^{[b]} \,. \tag{3.13}$$

Vector components that are expressed in the centre of motion reference frame are denoted by square bracketed latin indices, where $[b] \in \{0, 1, 2, 3\}$.

As the rest frame of the surface of the spinning emitter is defined with respect to the normalized four-momentum, instead of the tangent of the world line, there needs to be a reference frame that is co-moving with the normalized four-momentum.

3.1.3 Centre of momentum reference frame

In this subsection, the **c**entre **o**f **mom**entum (COMOM) reference frame is established. The rest frame in which the observer is at rest on the surface of the spinning light source is defined with respect to the normalized four-momentum U^ν. The reference frame described above, however, is co-moving the with the four-velocity V^ν of the spinning emitter. As the two velocities are generally not parallel if the emitter is spinning (see the discussion at the end of chapter 2), another reference frame, that is co-moving with the normalized four-momentum, needs to be established. For the remainder of this thesis, this reference frame will consequently be called the centre of momentum frame.

First, the relative velocity between the normalized four-momentum U^ν and the tangent of the world line V^ν has to be calculated. For any two normalized four-vectors X^ν and Y^ν that are not parallel to each other, the velocity $\mathcal{V}$ between those can be written as (see e.g. [36])

$$X^\nu Y_\nu = \frac{1}{\sqrt{1 - \mathcal{V}}} \,. \tag{3.14}$$

In the context of spinning particles, and in particular by using the Tulczjiew-Dixon supplementary condition, the tangent of the world line is not normalized, i.e. $V^\nu V_\nu \neq -1$. Thus, a normalized four-velocity

$$W^\nu := \frac{V^\nu}{\sqrt{-V_\nu V^\nu}} \tag{3.15}$$

is introduced. Using the fact that U^ν is normalized, i.e. $U^\nu U_\nu = -1$, and the normalization condition in Eq. (2.14), i.e. $U^\nu V_\nu = -1$, one can find the relative velocity between the normalized four-momentum and the tangent of the world line as

$$\frac{1}{\sqrt{1-\mathcal{V}^2}} = U_\nu W^\nu = \frac{1}{\sqrt{-V_\nu V^\nu}} \tag{3.16}$$

$$\Rightarrow \quad \mathcal{V}^2 = 1 + V_\nu V^\nu \, . \tag{3.17}$$

The exact form of this velocity depends on the position of the emitter, and, more generally, on the background spacetime considered. The relative velocity of an emitter orbiting in Schwarzschild and Kerr spacetimes will be given and discussed in chapters 5.2.3 and 6.2.3, respectively.

Now that the formula for the relative velocity has been established, the transformation from the centre of mass reference frame into the centre of momentum reference frame can be introduced:

$$\mathbf{e}_{\langle c\rangle} = \Lambda^{[b]}_{\langle c\rangle}\, \mathbf{e}_{[b]} \, , \tag{3.18}$$

$$\mathbf{e}^{\langle c\rangle} = \left(\Lambda^{-1}\right)^{\langle c\rangle}_{[b]}\, \mathbf{e}^{[b]} \, , \tag{3.19}$$

where the exact Lorentz transformation is dependent on the spin direction, relative to the motion of the spinning body. For an emitter on circular motion and spin parallel to the orbit angular momentum, the transformation can be written as

$$\Lambda^{[b]}_{\langle c\rangle} = \begin{pmatrix} \Gamma & 0 & 0 & \Gamma\mathcal{V} \\ 0 & 1 & 0 & 0 \\ 0 & 0 & 1 & 0 \\ \Gamma\mathcal{V} & 0 & 0 & 1+\frac{\Gamma^2\mathcal{V}^2}{1+\Gamma} \end{pmatrix} \tag{3.20}$$

and its inverse

$$\left(\Lambda^{-1}\right)^{\langle c\rangle}_{[b]} = \begin{pmatrix} \Gamma & 0 & 0 & -\Gamma\mathcal{V} \\ 0 & 1 & 0 & 0 \\ 0 & 0 & 1 & 0 \\ -\Gamma\mathcal{V} & 0 & 0 & 1+\frac{\Gamma^2\mathcal{V}^2}{1+\Gamma} \end{pmatrix} \, . \tag{3.21}$$

In this context, Γ is defined as $\Gamma = \left[1-\mathcal{V}^2\right]^{-1/2}$. Equivalently, for completion purposes, one can define the formulae for the back transformation, i.e. the transformation from the COMOM frame back into the COM frame, as

$$\mathbf{e}_{[b]} = \left(\Lambda^{-1}\right)^{\langle c\rangle}_{[b]}\, \mathbf{e}_{\langle c\rangle} \, , \tag{3.22}$$

$$\mathbf{e}^{[b]} = \Lambda^{[b]}_{\langle c\rangle}\, \mathbf{e}^{\langle c\rangle} \, . \tag{3.23}$$

Vector components that are expressed in the centre of momentum frame of the emitter are denoted by angular bracketed latin indices, where $\langle c\rangle \in \{0,1,2,3\}$.

An additional remark can be made in the general case of non-spinning particles. If the object of interest is not spinning, or the background spacetime is flat, the normalized four-momentum and the tangent to the world line are parallel, and the relative velocity vanishes. Consequently, the centre of mass and centre of momentum reference frames coincide in the case of a non-spinning emitter.

By establishing the centre of momentum reference frame, it is now possible to construct the surface rest frame.

3.1.4 Surface rest frame

The goal of this section is to construct a reference frame in which the observer is at rest on the surface of the spinning emitter. This can be accomplished by transforming from the centre of momentum reference frame via a Lorentz transformation, as established in the previous subsections.

To construct the components of the surface velocity, a relationship is required between the spin vector (see Eq. (2.11)) and the angular velocity of the spinning light source. Following Ehlers and Rudolph [24], the two quantities are related via the inertia tensor I of the object, i.e.

$$S^{\langle i\rangle} = I^{\langle i\rangle\langle j\rangle}\Omega_{\langle j\rangle} \,, \tag{3.24}$$

where Ω is the angular velocity vector and $i,\ j \in \{1,2,3\}$. Note that this equation holds only in the centre of momentum reference frame. Thus, it becomes necessary to transform the spin vector into the COMOM reference frame.

Since the spin angular momentum of the emitter is chosen to be (anti-)parallel to the orbit angular momentum, there is only one non-vanishing component of the spin vector as measured in the ZAMO reference frame, specifically $S^{(2)}$ (see in particular [37]). This fact considerably simplifies the transformation of the spin vector into the COMOM reference, as the Lorentz transformations established in Eqs. (3.10) and (3.20) leave the (2)- and $[2]$-component of any vector invariant, i.e. $S^{(2)} = S^{[2]} = S^{\langle 2\rangle}$.

Another consequence of the (anti-)parallelity of the spin angular momentum and the orbit angular momentum is that the angular velocity vector has to be orthogonal to the tangent of the world line of the light source, i.e.

$$U^{\langle c\rangle}\Omega_{\langle c\rangle} = 0 \,; \tag{3.25}$$

here, the scalar product is evaluated in the COMOM reference frame. This equation, combined with the fact that the spin vector, as measured in the COMOM reference frame, has only one non-vanishing component, determine that there is only one non-vanishing component of the angular velocity vector, too, namely

$$\Omega_{\langle c\rangle} = \begin{cases} \omega & c = 2 \\ 0 & \text{else} \,, \end{cases} \tag{3.26}$$

where we define the magnitude of this non-vanishing component of the angular velocity as $\Omega_{\langle 2\rangle} =: \omega_0$.

With the relationship between the spin vector and the angular velocity established, the non-vanishing components of the surface velocity $u^{\langle 1\rangle}$ and $u^{\langle 3\rangle}$, as measured in the COMOM reference frame, can be computed via

$$u^{\langle i\rangle} = -\varepsilon^{\langle i\rangle}{}_{\langle j\rangle\langle k\rangle} r^{\langle j\rangle}\Omega^{\langle k\rangle} \,, \tag{3.27}$$

where $r^{\langle j\rangle}$ is the three-dimensional vector that parametrizes the surface of the emitter as measured in the COMOM reference frame, pointing from the origin of the emitter to a point on the surface; $\varepsilon^{\langle i\rangle}{}_{\langle j\rangle\langle k\rangle}$ is the total anti-symmetric tensor and $i,\ j,\ k\ \in \{1,2,3\}$.

Since $\Omega^{\langle k\rangle}$ has only one non-vanishing component, there are only two non-vanishing components of the linear 3-velocity for each point on the surface, i.e.

$$u^{\langle i\rangle} = \begin{bmatrix} u^{\langle 1\rangle}\ , & 0\ , & u^{\langle 3\rangle} \end{bmatrix}, \qquad i \in \{1,\ 2,\ 3\}\ . \tag{3.28}$$

Note that the above formula denotes the components of the 3-velocity of any surface element in the centre of momentum reference frame, as indicated by the angular brackets.

The exact form of the components of the surface velocity depends on the chosen shape and geometry of the spinning light source. In the following chapter, the properties, geometry and surface velocity are discussed for two types of emitter shapes. In section 4.1, these are expressed for a spherical emitter; in section 4.2, the behavior and equations for an emitter taking the shape of a Maclaurin spheroid are given.

Now that the formulae for the surface velocities are established, the transformation from the centre of momentum reference frame into the surface rest frame (SRF) can be introduced:

$$\mathbf{e}_{\{d\}} = \Lambda^{\langle c\rangle}_{\{d\}}\ \mathbf{e}_{\langle c\rangle}\ , \tag{3.29}$$

$$\mathbf{e}^{\{d\}} = \left(\Lambda^{-1}\right)^{\{d\}}_{\langle c\rangle}\ \mathbf{e}^{\langle c\rangle}\ , \tag{3.30}$$

where the tensor of transformation is given by

$$\Lambda^{\langle c\rangle}_{\{d\}} = \begin{pmatrix} \gamma & \gamma u^{\langle 1\rangle} & 0 & \gamma u^{\langle 3\rangle} \\ \gamma u^{\langle 1\rangle} & 1+\frac{\gamma^2 (u^{\langle 1\rangle})^2}{1+\gamma} & 0 & \frac{\gamma^2 u^{\langle 1\rangle} u^{\langle 3\rangle}}{1+\gamma} \\ 0 & 0 & 1 & 0 \\ \gamma u^{\langle 3\rangle} & \frac{\gamma^2 u^{\langle 1\rangle} u^{\langle 3\rangle}}{1+\gamma} & 0 & 1+\frac{\gamma^2 (u^{\langle 3\rangle})^2}{1+\gamma} \end{pmatrix} \tag{3.31}$$

and the inverse transformation

$$\left(\Lambda^{-1}\right)^{\{d\}}_{\langle c\rangle} = \begin{pmatrix} \gamma & -\gamma u^{\langle 1\rangle} & 0 & -\gamma u^{\langle 3\rangle} \\ -\gamma u^{\langle 1\rangle} & 1+\frac{\gamma^2 (u^{\langle 1\rangle})^2}{1+\gamma} & 0 & \frac{\gamma^2 u^{\langle 1\rangle} u^{\langle 3\rangle}}{1+\gamma} \\ 0 & 0 & 1 & 0 \\ -\gamma u^{\langle 3\rangle} & \frac{\gamma^2 u^{\langle 1\rangle} u^{\langle 3\rangle}}{1+\gamma} & 0 & 1+\frac{\gamma^2 (u^{\langle 3\rangle})^2}{1+\gamma} \end{pmatrix}\ . \tag{3.32}$$

In this context, γ is defined as

$$\gamma = \left[1-(u^{\langle 1\rangle})^2-(u^{\langle 3\rangle})^2\right]^{-1/2}. \tag{3.33}$$

For completion purposes, the back transformation from the SRF to the COMOM reference frame can be defined as

$$\mathbf{e}_{\langle c\rangle} = \left(\Lambda^{-1}\right)^{\{d\}}_{\langle c\rangle}\ \mathbf{e}_{\{d\}}\ , \tag{3.34}$$

$$\mathbf{e}^{\langle c\rangle} = \Lambda^{\langle c\rangle}_{\{d\}}\ \mathbf{e}^{\{d\}}\ . \tag{3.35}$$

Vector components that are expressed in the rest frame of the emitter are denoted by curly bracketed latin indices, where $\{d\} \in \{0,1,2,3\}$.

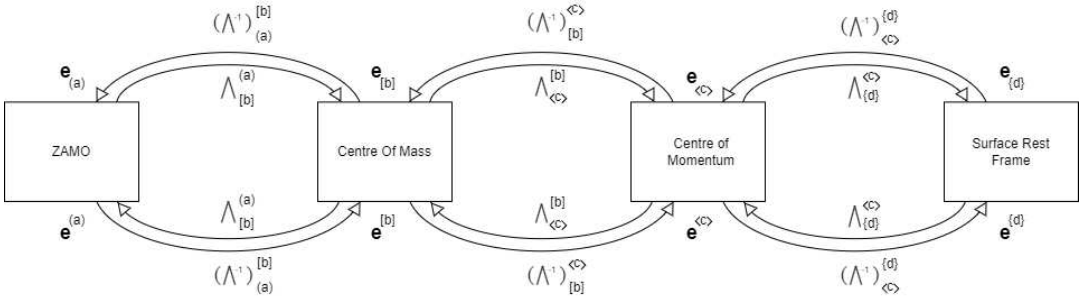

Figure 3.1: Overview over the introduced reference systems and the appropriate transformation tensors that link these frames of reference.

An additional remark has to be made for the components of the surface velocity. We require the surface of the emitter to move with subluminal speed, i.e.

$$1 - (u^{\langle 1 \rangle})^2 - (u^{\langle 3 \rangle})^2 > 0 \,, \tag{3.36}$$

which imposes a limit on the spin in relation to the notion of size of the object. The exact form of this limit is dependent on the geometry of the emitter, see e.g. [34] or [36], and will be discussed in more detail in chapter 4.

A graphical summary and overview of these reference frames and their connections to each other is given in figure 3.1. Following the definition of the reference frame which is co-moving with the surface of the emitter, it is possible to define the type of emission with respect to this reference frame, and relate the constants of motion of the light ray to the emission properties.

3.1.5 Relating the emission angles to the constants of motion

In this subsection, the relation between the quantities describing the emission and the constants of motion of the light ray itself is established. In this context, the solution of the geodesic equation for lightlike geodesics k^ν in terms of a set of constants of motion ζ_i is assumed to be known for the considered spacetime. The four-momentum of the lightlike geodesic can then be written as

$$p_\nu(\zeta_i) = g_{\nu\lambda} k^\lambda(\zeta_i) \,. \tag{3.37}$$

It is possible to relate the four-momentum of the lightlike geodesic in spacetime coordinates to the four- momentum as measured in the SRF reference frame, i.e.

$$e^\mu_{(a)}\, p_\mu \overset{!}{=} \left(\Lambda^{-1}\right)^{[b]}_{(a)} \left(\Lambda^{-1}\right)^{\langle c \rangle}_{[b]} \left(\Lambda^{-1}\right)^{\{d\}}_{\langle c \rangle} p_{\{d\}} \,. \tag{3.38}$$

Here, $p_{\{d\}}$ is the four-momentum of the photon with respect to the reference frame that is at rest on the surface of the emitter. For simplicity, *isotropic* emission is assumed, i.e.

$$p_{\{0\}} = -\chi \,, \tag{3.39}$$

$$p_{\{1\}} = \chi \, \cos\iota \sin\eta \,, \tag{3.40}$$

$$p_{\{2\}} = \chi \, \cos\eta \,, \tag{3.41}$$

$$p_{\{3\}} = \chi \, \sin\iota \sin\eta \,. \tag{3.42}$$

In this regard, ι corresponds to an azimuth emission angle, $\iota \in [0,\, 2\pi)$, η corresponds to an polar angle, $\eta \in [0, \pi]$, and χ is a normalization parameter. All physically relevant observables are independent on the normalization parameter. Finally, the constants of motion of the lightlike geodesic can be related to the emission angles as seen on the rest frame of the surface, by evaluating Eq. (3.38):

$$e^{-\nu}\, p_t + \omega\, e^{-\nu}\, p_\varphi = -\chi \cdot \gamma(b_0 + v b_3), \tag{3.43}$$

$$e^{-\mu_1}\, p_r = \chi \cdot c_1, \tag{3.44}$$

$$e^{-\mu_2}\, p_\vartheta = \chi \cdot \cos\eta, \tag{3.45}$$

$$e^{-\psi}\, p_\varphi = \chi \cdot \left(\gamma v\, b_0 + \left[1 + \frac{\gamma^2 v^2}{1+\gamma}\right] b_3\right), \tag{3.46}$$

with

$$b_0 = \Gamma[c_0 + \mathcal{V}\, c_3], \qquad b_3 = \Gamma\mathcal{V}\, c_0 + \left(1 + \frac{\Gamma^2\mathcal{V}^2}{1+\Gamma}\right) c_3\,, \tag{3.47}$$

and

$$c_0 = \gimel \cdot [1 + u^{\langle 1\rangle} \cos\iota \sin\eta + u^{\langle 3\rangle} \sin\iota \sin\eta], \tag{3.48}$$

$$c_1 = -\gimel\, u^{\langle 1\rangle} + \left(1 + \frac{\gimel^2\, (u^{\langle 1\rangle})^2}{1+\gimel}\right) \cos\iota \sin\eta \tag{3.49}$$

$$+ \left(\frac{\gimel^2\, u^{\langle 1\rangle} u^{\langle 3\rangle}}{1+\gimel}\right) \sin\iota \sin\eta\,, \tag{3.50}$$

$$c_3 = -\gimel\, u^{\langle 3\rangle} + \left(\frac{\gimel^2\, u^{\langle 1\rangle} u^{\langle 3\rangle}}{1+\gimel}\right) \cos\iota \sin\eta \tag{3.51}$$

$$+ \left(1 + \frac{\gimel^2\, (u^{\langle 3\rangle})^2}{1+\gimel}\right) \sin\iota \sin\eta\,. \tag{3.52}$$

The equations above are used to numerically solve the emitter-observer problem:

For every pair of emission angles $(\iota,\, \eta)$, it is possible to construct the corresponding light ray associated with the constants of motion. One may introduce an observer at any arbitrary position in spacetime, moving with arbitrary velocity. Now, the emission angles are varied such that the resulting light ray reaches the observer; this has to be done numerically, as there is no analytical solution to this kind of problem. The numerical procedure is discussed in detail in section 3.3.

There are some important remarks to be made. The emitter itself is assumed to be fully opaque; any light that passes through the emitter before reaching the observer is discarded. Throughout this thesis, the observer is assumed to be stationary, which is important for the discussion on the redshift associated with the light rays.

In the next section, some applications regarding observables of this formalism are discussed.

3.2 Observables

The vast majority of observational astrophysics is done by analyzing the properties of light coming from their respective emitters directly, or the effect of matter distributions effecting the light on its way to the observers. In this section, some observable quantities of light rays coming from spinning emitters on a circular orbit around a compact object are discussed, such that the influence of the spin on these observables can be studied.

The first section deals with the notion of a screen at the observer's position, adapted from Grenzebach et al. [38]. This notion will be used to visualize the results of the following subsections.

As a first application of the formalism introduced in the previous section, the second subsection is dedicated to calculating the shift of a polarization angle, if the light is assumed to be linearly polarized in the rest frame of the surface. The effect of the spin on the polarization angle for a spinning emitter in Schwarzschild and Kerr spacetime specifically are discussed in detail in sections 5.3.3 and 6.3.3, respectively.

In the third subsection, the redshift of a light ray coming from a spinning emitter in relation to a stationary observer is calculated and discussed in detail. In particular, this will be used to calculate and visualize the redshift distribution, as seen by an observer, for an emitter orbiting a Schwarzschild and Kerr object, see sections 5.3.2 and 6.3.2, respectively.

The ensuing subsection is dedicated to calculating the flux of the spinning emitter, as measured by an stationary observer. While, even with modern precision, the redshift distribution of a light source cannot be observed directly due to its small angular size at the observer, measuring the flux of such a light source is common practice, e.g. when studying the line emission from accretion disks around black holes [39]. In sections 5.3.4 and 6.3.2, the influence of the spin on the observed flux is studied for a spinning emitter in Schwarzschild and Kerr spacetime, respectively.

3.2.1 Celestial sphere coordinates at the observer

In order to derive an analytical formula describing the point of detection on the screen of the observer, the orthonormal tetrad of the observer must be fixed. Recall from section 3.1.1 that the observer is assumed to be stationary at a point in spacetime $(r_{\mathrm{obs}}, \vartheta_{\mathrm{obs}})$, and follows the definition of the ZAMO observer of 3.1.1, namely:

$$\mathbf{e}_{(0)} = e^{-\nu}\partial_t + \omega\, e^{-\nu}\partial_\varphi\,, \qquad \mathbf{e}_{(1)} = -e^{-\mu_1}\partial_r\,, \tag{3.53}$$

$$\mathbf{e}_{(2)} = e^{-\mu_2}\partial_\vartheta\,, \qquad \mathbf{e}_{(3)} = -e^{-\psi}\partial_\varphi\,. \tag{3.54}$$

Note that the signs in front of the basis vectors determine an observer whose radial direction $\mathbf{e}_{(1)}$ points towards the centre of the compact object. As usual, the timelike vector $\mathbf{e}_{(0)}$ is interpreted as the four-velocity of the observer.

For any light ray $\lambda(\sigma)$, the tangent vector at the position of the observer may be written either by using the coordinate basis or the tetrad introduced above, namely:

$$\dot{\lambda} = \dot{t}\partial_t + \dot{r}\partial_r + \dot{\vartheta}\partial_\vartheta + \dot{\varphi}\partial_\varphi \tag{3.55}$$

$$\dot{\lambda} = \zeta(-\mathbf{e}_0 + \cos\Theta\mathbf{e}_{(1)} + \cos\Phi\sin\Theta\mathbf{e}_{(2)} + \sin\Phi\sin\Theta\mathbf{e}_{(3)})\,. \tag{3.56}$$

Here, the celestial coordinates Φ and Θ are defined, where $\Phi \in [0,\ 2\pi)$ is the azimuth coordinate and $\Theta \in [-\pi/2,\ \pi/2)$ is the polar coordinate. In line with the argument introduced before, $\Theta = 0$ corresponds to the direction towards the compact object. The scalar factor ζ is

defined as

$$\zeta = g(\dot{\lambda}, \mathbf{e}_{(0)}) \,. \tag{3.57}$$

By comparing the coefficients in (3.55) and (3.56), it is possible to find the celestial coordinates in terms of the components of the four-velocity of the photon at the observer position:

$$\cos\Theta = -\frac{e^{\mu_1}\dot{r}}{\zeta} \,, \qquad \sin\Theta = \sqrt{1 - \frac{\dot{r}^2}{\zeta^2}} \,, \tag{3.58}$$

$$\cos\Phi = \frac{e^{\mu_2}\dot{\vartheta}}{\sqrt{\zeta^2 - \dot{r}^2}} \,, \qquad \sin\Phi = -\frac{e^{\psi}\dot{\varphi}}{\sqrt{\zeta^2 - \dot{r}^2}} \,. \tag{3.59}$$

Usually, the observer screen is given in flattened coordinates $(\alpha,\ \beta)$, which are Cartesian coordinates obtained by standard stereographic projection, i.e.

$$\begin{aligned} \alpha &:= -2\frac{(1-\cos\Theta)}{\sin\Theta}\sin\Phi \,, \\ \beta &:= 2\frac{(1-\cos\Theta)}{\sin\Theta}\cos\Phi \,. \end{aligned} \tag{3.60}$$

This notion of the celestial sphere and observer screen coordinates form the basis of simulating the observations and the influence of the spin and gravity on them. The following subsection deals with the theoretical description of the polarization angle in this context.

3.2.2 Polarization angle

In astronomy and astrophysics, the polarization angle of light is heavily studied, as it gives rise to information on the properties of its emitter. Emissions from accretion disks near compact objects are expected to be strongly polarized (see [40, 41, 42]), and studying the polarization may put constraints on the physical appearance and parameters of the compact source. Furthermore, there is interest in studying the polarization of light emitted by neutron stars and pulsars; these are of particular interest in the context of this thesis, as they are expected to have high angular velocities. Specifically, the NICER mission and instrument aboard the International Space Station will provide precise measurements of neutron stars, assisting in measuring the polarization of light emitted by them, see e.g. [43].

In this subsection, a notion for a polarization angle that is observed by an arbitrary observer is needed.

For simplicity, let $f^{\{d\}}$ be the polarization vector that is parallel to the $\mathbf{e}^{\{2\}}$ axis, as measured in the rest frame of the surface. This leaves two non-zero components for the polarization vector; in particular, one can write

$$f^{\{d\}} = N \cdot \Big(F^0 \,, \quad 0 \,, \quad F^2 \,, \quad 0 \Big) \,, \tag{3.61}$$

where N is a normalization constant that is to be fixed, and F^0 and F^2 are the components of the polarization vector yet to be determined.
The polarization vector is orthogonal to the four-momentum p of the photon, i.e.

$$p_{\{d\}}\, f^{\{d\}} = 0 \,, \tag{3.62}$$

where the product is evaluated in the reference frame that co-rotates with the surface of the emitter. As a consequence, there exists a relation between F^0 and F^2, namely

$$F^2 = -\frac{p_{\{0\}}}{p_{\{2\}}} \cdot F^0 \,. \tag{3.63}$$

Without loss of generalization, one may choose $F^0 := -1$. Thus, the polarization vector can be written as

$$f^{\{d\}} = N \cdot \left(-1 \,, \quad 0 \,, \quad \frac{p_{\{0\}}}{p_{\{2\}}} \,, \quad 0 \right) . \tag{3.64}$$

The normalization constant N can be fixed by requiring

$$g_{(a)(b)} f^{(a)} f^{(b)} = 1 \qquad \text{with} \qquad f^{(a)} = \Lambda^{(a)}_{[b]} \Lambda^{[b]}_{\langle c \rangle} \Lambda^{\langle c \rangle}_{\{d\}} f^{\{d\}} \,. \tag{3.65}$$

The scalar product is evaluated here in the ZAMO reference frame for convenience, as $g_{(a)(b)} = \eta_{(a)(b)}$. Then, the constant N can be written as

$$\begin{aligned} N = \Bigg(& \left[\gamma(\urcorner\Gamma + \urcorner u^{\langle 3 \rangle} \Gamma \mathcal{V}) + \gamma v (\urcorner \Gamma \mathcal{V} + \urcorner u^{\langle 3 \rangle} \Gamma) \right]^2 \\ & + (\urcorner u^{\langle 1 \rangle})^2 + \left(\frac{p_{\{0\}}}{p_{\{2\}}} \right)^2 \\ & + \left[\gamma v (\urcorner \Gamma + \urcorner u^{\langle 3 \rangle} \Gamma \mathcal{V}) + \gamma (\urcorner \Gamma \mathcal{V} + \urcorner u^{\langle 3 \rangle} \Gamma) \right]^2 \Bigg)^{-\frac{1}{2}} \end{aligned} \tag{3.66}$$

The physical quantity measured by an observer, however, is not the polarization vector itself, but rather the polarization angle. In general, to measure this polarization angle, the polarization vector is parallel transported to the position of the observer along the light ray. This would require the integration of the parallel transport equation, in addition to the geodesic equation. Nevertheless, it is possible to calculate the components of the polarization vector at any point in spacetime along the light's path due to the existence of another conserved quantity along the geodesic: the Penrose-Walker constant [44]. This constant is a complex number for which both real and imaginary parts are conserved along the light ray, and is well-known in both considered spacetimes, in Schwarzschild and Kerr, see e.g. [45, 46].

In addition to the normalization condition and the orthogonality condition in spacetime coordinates, namely

$$1 = g_{\lambda\nu} f^\lambda f^\nu \,, \tag{3.67}$$

$$0 = g_{\lambda\nu} k^\lambda f^\nu \,, \tag{3.68}$$

the conservation of the Penrose-Walker constant results in 4 non-trivial determining equations for the four components of the polarization vector at any point in spacetime [45], as long as the value of the constant and the four-velocity at the point of evaluation are known. Thus, the following procedure for calculating the polarization angle is established.

Procedure for calculating the polarization angle for an arbitrary stationary observer

The prerequisite for calculating the polarization angle is the numerical computation of the world line and its tangent of the light ray that connects the emitter and observer, following the procedure introduced in the previous subsection.

Then, in order to calculate f at an arbitrary point in spacetime, the components of the polarization vector, as measured in the SRF reference frame, have to be transformed to spacetime coordinates. This is where the effects of spin and orbital rotation come into play.

Afterwards, the four determining equations described above are used to determine all components of the polarization vector at the position of the observer in spacetime coordinates, using the components of the four-velocity calculated in the process of ray tracing.

Finally, the polarization vector is measured in the observer rest frame, projected onto the observer screen and then the angle between the polarization and some arbitrary axis on the screen is calculated.

For the projection of the polarization vector onto the celestial sphere of the observer, consider a toy light ray connected to the original light ray by the polarization vector. One may now repeat the process described in 3.2.1. The coordinate vector of the toy light ray $\lambda'(\sigma)$ can be constructed by

$$\lambda'(\sigma) = \lambda(\sigma) + \epsilon\delta(\sigma) \,, \tag{3.69}$$

where $\lambda(\sigma)$ is the coordinate vector of the original light ray, $\epsilon \ll 1$ is a small, real, positive factor and δ is connected to the polarization vector via

$$\dot{\delta}(\sigma) := f(\sigma) \,. \tag{3.70}$$

By again writing the tangent vector of the toy light ray in terms of the coordinate basis and the tetrad, one can obtain the celestial coordinates of the toy light ray in terms of the four-velocity of the original photon and the components of the polarization vector at the position of the observer, i.e.:

$$\cos\Theta = -\frac{e^{\mu_1}(\dot{r} + \epsilon f^r)}{\zeta} \,, \qquad \sin\Theta = \sqrt{1 - \frac{(\dot{r} + \epsilon f^r)^2}{\zeta^2}} \,, \tag{3.71}$$

$$\cos\Phi = \frac{e^{\mu_2}(\dot{\vartheta} + \epsilon f^\vartheta)}{\sqrt{\zeta^2 - (\dot{r} + \epsilon f^r)^2}} \,, \qquad \sin\Phi = -\frac{e^{\psi}(\dot{\varphi} + \epsilon f^\varphi)}{\sqrt{\zeta^2 - (\dot{r} + \epsilon f^r)^2}} \,. \tag{3.72}$$

The polarization angle is then found by stereographic projecting the celestial coordinates of the toy light ray into the Cartesian (α, β) coordinates (see Eq. (3.60)) and simple geometry. The polarization angle is defined as the angle of the line connecting the toy light ray and the original light ray on the observer screen with the positive β axis, which corresponds to the axis $\Phi = 0,\ \Theta > 0$.

For Schwarzschild and Kerr, as mentioned before, the Penrose-Walker constant is known. The components of the polarization vector at any point in spacetime are rather unhandy, and are given in the appendix (for more detail, see sections 5.3.3 and 6.3.3, respectively). The distribution of this angle on the observer's screen can then be examined; for a light source orbiting a Schwarzschild object, this is done in detail in section 5.3.3, and for a light source orbiting a Kerr black hole, the results can be found in section 6.3.3.

3.2.3 Redshift

For any given point on the surface of the spinning emitter, it is possible to determine the light ray that reaches the observer, as described in the previous section. An important observable of this light ray is its redshift, relative to the observer. In the context of general relativity, the redshift z of a light ray is commonly defined as

$$z = 1/g - 1 \,, \tag{3.73}$$

where $g =: \nu_{\rm obs}/\nu_{\rm em}$ is the energy- or frequency ratio. The redshift of a light ray is generally influenced by the gravitational field(s) and the velocity of the emitter and observer; for further discussions on this, see e.g. [36]. In general, the energy ratio can be written as

$$g = \frac{E_{\rm obs}}{E_{\rm em}} = \frac{-p_\kappa \, \mathcal{U}^\kappa_{\rm obs}\Big|_{\rm obs}}{-p_\sigma \, \mathcal{U}^\sigma_{\rm em}\Big|_{\rm em}} \,, \tag{3.74}$$

where $\mathcal{U}$ is the four-velocity of the observer and emitter, depending on the subscript.

In the context of this thesis, the observer is in general assumed to be stationary, thus its local observation frame is also described as a ZAMO frame at the position of the observer, which may be chosen arbitrarily. Then, the energy of a light ray, as measured in the rest frame of the observer, can simply be written as

$$E_{\rm obs} = -p_{(0)}\Big|_{\rm obs} = -e^t_0 \, p_t - e^\varphi_0 \, p_\varphi\Big|_{\rm obs} = -e^{-\nu} p_t - \omega e^{-\nu} p_\varphi\Big|_{\rm obs} \,, \tag{3.75}$$

where $p_\kappa := g_{\kappa\lambda} k^\lambda$ denotes the four-momentum of the photon, and k^λ is the four-velocity of the photon. It is important to remember that e^t_0 and e^φ_0 are the components of the local tetrad (cf. Eq. (3.5)), while $e^{-\nu}$ are the metric factors, as defined in Eq. (3.1).

Similarly, it becomes necessary to evaluate the product in Eq. (3.74). This product is independent on the choice of reference frame, thus it may be chosen arbitrarily. The reference frame, in which the four-velocity $\mathcal{U}_{\rm em}$ takes the simplest form, is in the COMOM reference frame, where the velocity can be written as

$$\mathcal{U}^{\langle 0\rangle}_{\rm em} = \beth \,, \qquad \mathcal{U}^{\langle 1\rangle}_{\rm em} = \beth \, u^{\langle 1\rangle} \,, \tag{3.76}$$

$$\mathcal{U}^{\langle 2\rangle}_{\rm em} = 0 \,, \qquad \mathcal{U}^{\langle 3\rangle}_{\rm em} = \beth \, u^{\langle 3\rangle} \,. \tag{3.77}$$

Thus, in order to calculate the product of the four-velocity of the emitter and the four-momentum of the light ray, it is imperative to transform the four-momentum into the COMOM reference frame, with the transformation procedure as described in the previous section. Accordingly, the energy of the light ray at emission can then be calculated to be

$$\begin{aligned} E_{\rm em} = -\Bigg[& (e^{-\nu} p_t + \omega e^{-\nu} p_\varphi) \cdot \left(\gamma \left(\beth\Gamma - \beth \, u^{\langle 3\rangle} \Gamma \mathcal{V} \right) - \gamma v \left(-\beth\Gamma\mathcal{V} + \beth \, u^{\langle 3\rangle} \left(1 + \frac{\Gamma^2 \mathcal{V}^2}{1+\Gamma} \right) \right) \right) \\ & + e^{-\mu_1} p_r \cdot \beth u^{\langle 1\rangle} + e^{-\psi} p_\varphi \cdot \left(-\gamma v \left(\beth\Gamma - \beth \, u^{\langle 3\rangle} \Gamma \mathcal{V} \right) \right. \\ & \left. + \left(1 + \frac{\gamma^2 (v)^2}{1+\gamma} \right) \cdot \left(-\beth\Gamma\mathcal{V} + \beth \, u^{\langle 3\rangle} \left(1 + \frac{\Gamma^2 \mathcal{V}^2}{1+\Gamma} \right) \right) \right) \Bigg]_{\rm em} \,. \end{aligned} \tag{3.78}$$

The energy fraction g is then the fraction of the energy of the light ray, as measured by the observer, in Eq. (3.75), over the energy of the light ray at the point of emission in Eq. (3.78). The redshift follows accordingly, see Eq. (3.73).

Evidently, as the velocities and the four-momentum of the photon itself depend on the choice of background spacetime, so too does the redshift. In section 5.3.2, the redshift is calculated for a spinning light source in Schwarzschild spacetime, and the effect of the spin on the redshift distribution on the observer's screen is studied. Similarly, in section 6.3.2, the same is done for a spinning light source orbiting a Kerr black hole.

If the redshift distribution of the image of the spinning light source on the observer's screen is calculated, then the associated flux can be determined. The theoretical basis for the calculations is discussed in the following subsection.

3.2.4 Flux

The spectrographic observation of astrophysical light sources is a widely used tool to investigate the physics of the emitter and its surroundings. Examples range from x-ray line profiles of accretion disks for investigating the properties of the environment immediately surrounding a black hole (e.g. [47, 39]), to extracting information about the atmosphere of transiting extrasolar planets (see e.g. [48]). While it is hardly possible to observe the redshift distribution of astrophysical light sources directly, it is common practice to measure the energy flux of these emitters.

First, some basic concepts and equations of radiation theory need to be recapitulated. Further details can be found in any standard introductory textbook on astrophysics, e.g. [49]. Assume there is some radiation passing through a surface, and consider an element of that surface $\mathrm{d}A$. The amount of energy entering a solid angle $\mathrm{d}\omega$ within a small frequency range $\mathrm{d}\nu$ in a time $\mathrm{d}t$ is

$$\mathrm{d}E_\nu = I_\nu \, \mathrm{d}A \, \mathrm{d}\nu \, \mathrm{d}\omega \, \mathrm{d}t \, , \tag{3.79}$$

where I_ν is the specific intensity of the radiation at frequency ν, with dimensions of W m^{-2} Hz^{-1} sr^{-1}. If the intensity profile, i.e. the dependency of the intensity on the frequency, at the point of emission is known, the total intensity I can be found by integrating over all frequencies, i.e.

$$I = \int_0^\infty I_\nu \, \mathrm{d}\nu \, . \tag{3.80}$$

From an observational point of view, it is generally more useful to describe the observed emission in terms of the flux density F or specific flux density F_ν. The specific flux density gives the power of radiation per unit area and frequency, has units of W m^{-2} Hz^{-1} and relates to the specific intensity as

$$F_\nu = \int I_\nu \, \mathrm{d}\omega \, , \tag{3.81}$$

while the flux density is the integrated power of radiation per unit area, has units of W m^{-2} and relates to the total intensity as

$$F = \int I \, \mathrm{d}\omega = \iint I_\nu \, \mathrm{d}\nu \, \mathrm{d}\omega \, . \tag{3.82}$$

For completeness, the flux or luminosity L is defined as the the power of the radiation emitted, and relates to the flux density as

$$L = \int F \, \mathrm{d}A \, . \tag{3.83}$$

In order to now calculate the flux density of an image of the spinning light source at the observer, it is necessary to describe the specific intensity of the radiation. Unless specifically stated otherwise, the radiation coming from the spinning light source is assumed to be monochromatic, i.e. $I_{\mathrm{em},\,\nu} = I_0 \, \delta(\nu - \nu_0)$, such that

$$I_{\mathrm{em}} = \int_0^\infty I_{\mathrm{em},\,\nu} \, \mathrm{d}\nu = I_0 \, . \tag{3.84}$$

Any flux density calculated will be given in units of I_0. For the purpose of calculating the flux density at the observer, it is important to relate the total intensity at the point of emission to the total intensity at the point of observation. In the context of geometrical optics, the quantity I_ν/ν^3 is conserved along the trajectory of the light [50], hence the flux density of the image at the observer is given by the following equation:

$$F_{\mathrm{obs}} = \int \int g^3 \cdot I_{\mathrm{em},\,\nu} \, \mathrm{d}\nu \, \mathrm{d}\omega = \int I_{\mathrm{em}} \cdot g^4 \, \mathrm{d}\omega \, , \tag{3.85}$$

where g is the frequency ratio of the light ray as introduced in the previous subsection.

For a spinning light source orbiting a Schwarzschild object, the variation of the flux density along its orbit and the influence of the spin on the flux density is calculated and discussed in chapter 5.3.4. An equivalent calculation and discussion on the flux density of a light source orbiting a Kerr black hole is given in chapter 6.3.4.

3.3 Numerical procedure

In this section, the numerical procedure used to gather the results and graphs in chapters 5 and 6 is discussed. It is arranged by topic into three subparts; first, the numerical calculation and finding of a single light ray is described; then, it is described how the results are combined to gather the image of the whole surface of the emitter; and lastly, the algorithm to finding the emitter on the observer's screen is highlighted.

Numerical procedure to find the light ray connecting the emitter and observer

First, the algorithm for calculating the properties of a single light ray that connects the emitter and observer is outlined.

In order to visualize the data, it is important to introduce a notion of a screen at the observer. For Schwarzschild and Kerr, this is established in chapters 5 and 6, respectively. Every point on the screen corresponds to a set of constants of motion of a lightlike curve, which are used to determine the initial velocities of the light ray. The initial position of the light ray, i.e. the position of the observer, is assumed to be known.

Afterwards, the full second order coupled differential equation for lightlike geodesics is solved numerically. While it is possible to reduce the geodesic equation to solving only 4 first order coupled differential equations for Schwarzschild and Kerr using the constants of motion, one must be careful in the treatment of turning points in each coordinate; in this sense, it is more practical to solve the full geodesic equation, if speed is not of utmost importance.

Then, a form of hit detection must be implemented. First, it is checked whether the distance of any point of the light ray to the centre of the emitter is smaller than its scale of geometry. This implies the possibility that the light ray hits the emitter. In order to retrieve the exact intersection of the light ray with the emitter, i.e. the point of emission, the light ray is interpolated around where the hit was detected. This assures that the point of emission is known precisely.

The set of spacetime coordinates of the point of emission is then converted into the local set of coordinates that parametrize the surface of the emitter (see chapter 4). Furthermore, this determines the surface velocities for this point of emission for a given spin value, and reaffirms the constants of motion via the emission angles. Then, as the four-velocity of the photon at emission is important for the calculation of e.g. the redshift, the exact light ray is calculated that starts at the emitter and passes the observer. In particular, this fixes the sign of the four-velocity of the lightlike curve, and serves as a double-check to confirm the previous calculations.

Imaging the surface of the emitter

Now, some remarks should be made regarding the imaging of the whole emitting surface, as seen on the observer's screen. For this, a subsection of the screen must be sampled; the dimensions of this sample and how to find it is detailed in the last subsection. This subsection of the screen is gridded using a set resolution, and for each point in this grid, the procedure for calculating the associated light ray is applied. If it does collide with the emitter, i.e. the light ray does indeed connect emitter and observer, the meta data containing e.g. the point of emission, the initial condition of the light ray and the surface velocities, are saved for later use, i.e. calculating the redshift. This results in an image of the entire emitting surface of the light source on the observer's screen. This has to be done for every position of the emitter on its orbit.

Finding the emitter on the observer's screen

In order to calculate the light rays that the observer receives on their screen, it is of utmost importance to first determine the position of the emitter on the observer's screen. Particularly, the subsection of the observer's screen that contains the primary image of the observer is quested. This also limits the geometry of the emitter; if the emitter is very small, it takes increasingly more effort to find it on the screen.

I have implemented an iterative process. First, the scale of geometry of the emitter is heavily increased, such that it becomes easily visible on the observer's screen. Thus, a large portion of the screen can be used, in combination with low resolution, to track the emitter. A matrix containing the information of whether the light ray associated with the point on the screen connects emitter and observer is made. Afterwards, the geometric mean is calculated, as well as the median distance of this mean to the edge of the image on the screen.

This marks the new subsection of the screen that has to be sampled. Iteratively, the scale of geometry of the emitter is reduced, and the new subsection of the screen to be sampled is calculated. This algorithm stops if the reduced size of the emitter is equal to or smaller than the scale of the emitter geometry that is to be used in the experiment itself. Then, the portion of the observer's screen that contains the image of the emitter is known, and this range of parameters is saved.

It is important to remark that this procedure is sensitive to the position of the emitter and observer, and also the source of gravity. For every point on its orbit, the image of the emitter on the observer's screen has to calculated. Furthermore, for every experiment that alters the position of the emitter or observer, this process has to be repeated. Moreover, it is important

to note that, in the case of a Kerr black hole, this procedure has to be repeated for each value of black hole spin.

Chapter 4

Emitter geometry

The information on the emitter geometry is needed to describe the velocity of any point on the surface of the emitter. In this chapter, two types of geometries, which are considered in this thesis, are discussed in more detail.

First, an emitter with spherical symmetry is considered. The sphere is assumed to be solid, i.e. there is neither differential rotation nor deformation to the emitter due to its rotation.

For a more realistic model, a Maclaurin spheroid is discussed. A Maclaurin spheroid is an oblate spheroid arising from a self-gravitating fluid with uniform density and constant angular velocity.

4.1 Spherical emitter

Consider the emitter to be a static sphere with radius ρ. Furthermore, consider a point on the surface of the ball in spherical coordinates on the tangent space (ρ, Θ, Φ), as measured from the COMOM reference frame. Then, the relation between the only non-vanishing component of the spin vector $S^{\langle 2\rangle}$ and the angular velocity $\Omega^{\langle 2\rangle} =: \omega_0$ (see Eq. (3.24)) is

$$\omega_0 = \frac{5}{2\rho^2} \cdot \frac{S^{\langle 2\rangle}}{\mu} \,, \tag{4.1}$$

where we used the fact that for a solid sphere, the only non-vanishing component of the inertia tensor is

$$I^{\langle 2\rangle\langle 2\rangle} = 2/5 \; \mu\rho^2 \,. \tag{4.2}$$

The goal of this section is to find the linear velocities for any point on the surface of the emitter. This can be achieved by linking the angular velocity to the position of the surface point in local spherical coordinates. As $\Omega^{\langle k\rangle}$ has only one non-vanishing component, there are only two non-vanishing components of $u^{\langle i\rangle}$, which can be calculated via Eq. (3.27):

$$u^{\langle 1\rangle} = \frac{5S^{\langle 2\rangle}}{2\mu\rho} \cdot \sin\Phi \sin\Theta, \qquad u^{\langle 3\rangle} = -\frac{5S^{\langle 2\rangle}}{2\mu\rho} \cdot \cos\Phi \sin\Theta \,. \tag{4.3}$$

Points on the surface of the emitter moving with superluminal speed are to be excluded, i.e.

$$1 - (u^{\langle 1\rangle})^2 - (u^{\langle 3\rangle})^2 > 0 \,. \tag{4.4}$$

This condition on the surface velocities imposes a limit on the spin vector in relation to the radius of the spherical emitter ρ. Specifically,

$$\frac{5|S^{\langle 2\rangle}|}{2\mu\rho} < 1 \,. \tag{4.5}$$

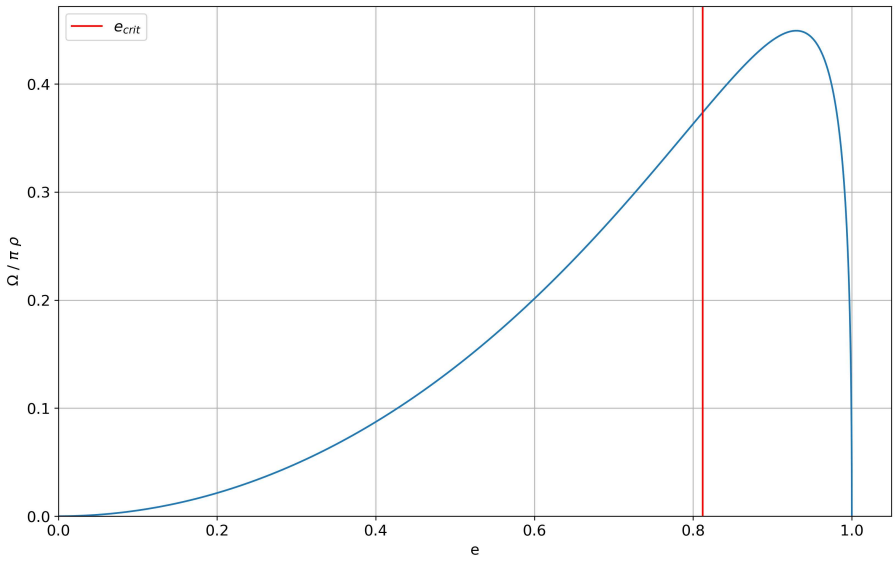

Figure 4.1: Graphical representation of Maclaurin's formula, cf. Eq. (4.6). Here, the square of the angular velocity in terms of the density as a function of the eccentricity is given. The red line indicates the critical eccentricity at $e_{\text{crit}} \approx 0.812$.

4.2 Spheroidal emitter

In this section, the linear velocities for any point on the surfaces of a spheroidal emitter are calculated. In particular, the emitter is modelled as a Maclaurin spheroid. For a thorough discussion on this topic, refer e.g. to [51].

4.2.1 Maclaurin spheroid

The first description of homogeneous bodies in uniform motion was made by Newton, investigating the shape of the Earth. In particular, he showed that the effect of a small rotation on the figure must result in a slightly oblate deformation.

The next advance in the theory was due to Maclaurin, who generalized Newton's result to the case where the ellipticity caused by the rotation cannot be considered small. Maclaurin spheroids are the simplest of ellipsoidal figures in hydrostatic equilibrium, describing homogeneous bodies rotating with constant angular velocity.

For such spheroids, there is an exact analytic formula linking the square of the angular velocity Ω^2 and the eccentricity e, called Maclaurin's formula:

$$\frac{\Omega^2}{\pi\rho} = \frac{2\sqrt{1-e^2}}{e^3}(3-2e^2)\arcsin(e) - \frac{6(1-e^2)}{e^2}\,. \tag{4.6}$$

The course of this graph can be seen in figure 4.1.

The eccentricity is defined via

$$e^2 = 1 - \frac{C^2}{A^2} \tag{4.7}$$

and determines the eccentricity of the meridional sections. Here, C is the polar semi-minor axis and A the equatorial semi-major axis.

As Maclaurin spheroids are figures of uniform density; the density ρ can be rewritten in terms of the mass μ and geometry of the spheroid, i.e.

$$\rho = \frac{\mu}{\frac{4}{3}\pi A^2 C} = \frac{3\,\mu}{4\pi A^3\sqrt{1-e^2}}\,. \tag{4.8}$$

Thus, the angular velocity can be rewritten in terms of the eccentricity e, the semi-major axis a and the mass μ:

$$\Omega^2 = \pi\rho\left(\frac{2\sqrt{1-e^2}}{e^3}(3-2e^2)\arcsin(e) - \frac{6(1-e^2)}{e^2}\right) \tag{4.9}$$

$$=: \frac{3\mu}{4A^3}\cdot\mathcal{F}(e)\,. \tag{4.10}$$

4.2.2 Linear surface velocity

Consider a point on the surface of a Maclaurin spheroid in parameterized coordinates on the tangent space (ϕ, θ). Here, ϕ is the usual azimuth angle, but θ does not describe an physical angle, measured to a Cartesian axis; rather, it is a real parameter with $\theta \in [0,\pi]$ used to parameterize the surface. This parameterization of the spheroid surface is then given by

$$r^{\langle 1\rangle} = A\cos\phi\sin\theta, \tag{4.11}$$

$$r^{\langle 2\rangle} = C\cos\theta, \tag{4.12}$$

$$r^{\langle 3\rangle} = A\sin\phi\sin\theta\,. \tag{4.13}$$

The goal of this section is to find the linear velocities for any point of the surface of the emitter. As before, this is achieved by linking the angular velocity to the position of the surface point in parameterized coordinates. Using the following relation for the non-vanishing components of the inertia tensor,

$$I^{\langle 2\rangle\langle 2\rangle} = 2/5\;\mu A^2\,, \tag{4.14}$$

and the fact that $\Omega^{\langle k\rangle}$ has only one non-vanishing component in $\Omega^{\langle 2\rangle} =: \omega_0$, it is possible to relate the angular momentum to the spin vector as

$$S^{\langle 2\rangle} = \frac{\mu}{5}\,A\sqrt{\frac{\mu}{A}}\cdot\sqrt{3\mathcal{F}(e)} \tag{4.15}$$

$$=: \frac{\mu}{5}\,A\sqrt{\frac{\mu}{A}}\cdot\mathcal{G}(e)\,, \tag{4.16}$$

$$\Rightarrow \omega = \frac{5}{2A^2}\cdot\frac{S^{\langle 2\rangle}}{\mu}\,. \tag{4.17}$$

This result is similar to the case of a spherical emitter in Eq. (4.1), where the semi-major axis A takes the role of the radius of the sphere.

The only two non-vanishing components of the surface velocity $u^{\langle 1\rangle}$ and $u^{\langle 3\rangle}$ can then be calculated to be

$$u^{\langle 1\rangle} = \frac{5S^{\langle 2\rangle}}{2\mu A} \cdot \sin\phi \sin\theta, \qquad u^{\langle 3\rangle} = -\frac{5S^{\langle 2\rangle}}{2\mu A} \cdot \cos\phi \sin\theta \,. \tag{4.18}$$

As discussed in the previous section, we want to exclude points on the surface that are moving with superluminal speed, cf. Eq. (4.5). Incidentally, this condition on the surface velocity imposes a limit on the spin vector in relation to the semi-major axis a. Specifically,

$$\frac{5|S^{\langle 2\rangle}|}{2\mu A} < 1 \,. \tag{4.19}$$

However, contrary to an spherical emitter, there is another restriction imposed on the parameters describing the spheroid due to secular instability.

4.2.3 Secular instability

It is important to note that Eq. (4.16) is not only dependent on the geometry and the spin value, but also on the mass μ. If the eccentricity of a Maclaurin spheroid is greater than $e_{\text{crit}} \approx 0.812$, any perturbation that would break the rotational symmetry leads to elongation into a Jacobian ellipsoid due to secular instability. Assuming the geometry and the spin value are fixed, this limit on the eccentricity also limits the mass allowed.

In the following, the spin vector $S^{\langle 2\rangle}$ is given in units of the small body mass μ, i.e. $S^{\langle 2\rangle}/\mu =: \mathcal{S}$. If the scale of geometry is chosen, i.e. the value of a, then equation (4.19) dictates a limit to the spin value $|\mathcal{S}| < \mathcal{S}_{\text{max}}$. To ensure that, for this value of spin and geometry, the spheroid is stable, i.e. $e < e_{\text{crit}} \approx 0.812$, there must be a limit to the mass of the test body μ, dictated by the following equation, derived from Eq. (4.16):

$$\mu_{\text{crit}} = \frac{25\mathcal{S}^2_{\text{max}}}{\mathcal{G}(e_{\text{crit}})^2} \frac{1}{A} \tag{4.20}$$

$$= \frac{2A}{\mathcal{G}(e_{\text{crit}})^2} \,. \tag{4.21}$$

In fact, this is a *lower* limit to μ, i.e. for a given spin and geometry, the mass of the test body cannot be smaller than μ_{crit}.

Thus, there are two limits to be considered for emitters that take the shape of a Maclaurin spheroid. If the value of A is fixed, then the requirement of subluminal speeds on the surface of the emitter in Eq. (4.19) limits the maximal absolute value of the spin that the emitter may have. Additionally, if secular stability is assumed, then the mass of the emitter is restricted via Eq. (4.21). Consequently, if the spin of the emitter and the semi-major axis are fixed, and the emitter is assumed to be at the critical mass value μ_{crit}, Eq. (4.16) may be used to determine the value of the semi-minor axis, if solved for e.

Chapter 5

Spinning emitter in Schwarzschild spacetime

The theory on modelling the emission from an spinning emitter, established in the previous chapters, was introduced for any stationary and axially symmetric spacetime for which the metric can be written as in Eq. (3.1). In this chapter, the theoretical description is applied to the spherically symmetric, static solution of the Einstein vacuum equations: the Schwarzschild metric. This chapter first discusses briefly the properties of the Schwarzschild spacetime. Furthermore, the properties of light coming from a spinning emitter around a Schwarzschild object are investigated, as well as the influence of the spin on the observables.

5.1 Schwarzschild spacetime

The most general family of axisymmetric, static and asymptotically flat solutions of the vacuum field equations in Eq. (2.1) is represented by the Weyl class of solutions, the simplest of which is the spherically symmetric Schwarzschild metric. It describes the gravitational field outside a spherical mass and its line-element in Boyer-Lindquist coordinates (see e.g. [52]) is given by

$$\mathrm{d}s^2 = g_{\mu\nu}\mathrm{d}x^\mu \mathrm{d}x^\nu = -\left(1-\frac{2M}{r}\right)\mathrm{d}t^2 + \left(1-\frac{2M}{r}\right)^{-1}\mathrm{d}r^2 + r^2(\mathrm{d}\vartheta^2 + \sin^2\vartheta\,\mathrm{d}\varphi^2)\,, \quad (5.1)$$

where M is the mass parameter.

The first subsection recapitulates the physical properties of the Schwarzschild solution as thorough as necessary for the scope of this thesis.

The second subsection covers the theoretical description and solution of lightlike geodesics in Schwarzschild spacetime, describing the path light rays take.

5.1.1 General physical properties

According to the Jebsen-Birkhoff theorem [53, 54], any spherically symmetric solution of the vacuum field equations has to be static and asymptotically flat. Thus, the exterior gravitational field of a spherically symmetric, uncharged, non-rotating source of gravity has to be described by the Schwarzschild metric. It is asymptotically flat, i.e. it transitions into the Minkwoski metric for $r \to \infty$, and is static. Accordingly, the mass M of the object uniquely determines the exterior gravitational field of any spherically symmetric, non-rotating source of gravity.

The Schwarzschild metric in the representation of Eq. (5.1) inhibits two singularities. The singularity at the origin $r = 0$ is a curvature singularity, which can be verified by calculating any curvature scalar (e.g. $R^{\alpha\beta\gamma\delta}R_{\alpha\beta\gamma\delta}$, see [55, 52]). The other singularity at $r = 2M$ is an

artifact of the chosen coordinates and can be removed by proper coordinate transformation; hence, it is called a coordinate singularity. One way to remove it is to map outgoing radial lightlike geodesics onto straight lines; this set of coordinates is called Eddington-Finkelstein coordinates [56, 57]. The distance of the coordinate singularity $r = 2M$ is called the Schwarzschild radius.

Any object whose outer radius decreases below the coordinate singularity $r = 2M$ (e.g. the core of a star collapsing in a supernova, see e.g. [58]) must collapse to $r = 0$, forming a black hole in the process. The hypersurface $r = 2M$ becomes a Killing- or event horizon; outside the event horizon, the Killing vector field $\partial/\partial t$ is timelike, and becomes spacelike when inside. When inside the event horizon, nothing in (sub)luminal motion can escape the black hole, or more generally increase its radius coordinate.

5.1.2 Lightlike geodesics

In this subsection, lightlike geodesics in Schwarzschild spacetimes are discussed. The path of light rays (or, more general, any lightlike object) are described by the solution of the lightlike geodesic equation; formulated in the form of the Euler-Lagrange equations, it can be written as

$$\frac{\mathrm{d}}{\mathrm{d}\sigma}\frac{\partial \mathcal{L}}{\partial \dot{x}^\mu} = \frac{\partial \mathcal{L}}{\partial x^\mu} \,, \tag{5.2}$$

where $\dot{x} := \frac{\mathrm{d}x}{\mathrm{d}\sigma}$ is the tangent of the world line x, differentiated with respect to the affine parameter σ along the geodesic. Furthermore, the Lagrangian $\mathcal{L}$ is connected to the metric via

$$\mathcal{L} = \frac{1}{2} g_{\mu\nu}\dot{x}^\mu \dot{x}^\nu \,. \tag{5.3}$$

For lightlike objects, the Lagrangian is a constant of motion; in particular, $\mathcal{L} = 0$. The geodesic equation is invariant under linear transformation of the affine parameter.

The solution of the geodesic equation is of particular importance, as the geodesics describe the path of light rays in curved spacetime. Consequently, the properties and analytic form of this solution in Schwarzschild spacetime is integral in studying the effects of spin on the light coming from spinning light sources. In particular, when discussing the properties of the radiation for a given set of emitter and observer properties, the lightlike geodesic equation is solved numerically, finding the light ray that connects emitter and observer.

The solution of the geodesic equation for lightlike geodesics in Schwarzschild spacetime is well-established (see e.g. [52, 36]) and can be written as

$$\dot{t} = \frac{E}{\left(1 - \dfrac{2M}{r}\right)} \,, \tag{5.4}$$

$$\dot{r} = \pm\sqrt{E^2 - \frac{Q + L^2}{r^2}\left(1 - \frac{2M}{r}\right)} \,, \tag{5.5}$$

$$\dot{\vartheta} = \pm r^2\sqrt{Q - L^2\cot^2\vartheta} \,, \tag{5.6}$$

$$\dot{\varphi} = \frac{L}{r^2\sin^2\vartheta} \,, \tag{5.7}$$

where the dot indicates a derivative with respect to the affine parameter, and E, Q and L are the constants of motion. In particular, E is the energy of the light ray, L its angular momentum and Q is the adopted Carter constant [59]. By rescaling the affine parameter, it is possible to absorb the factor E and give the solution above in the more common form in

terms of $\lambda := L/E$ and $q := Q/E^2$:

$$\dot{t} = \frac{1}{\left(1 - \frac{2M}{r}\right)} , \tag{5.8}$$

$$\dot{r} = \pm\sqrt{1 - \frac{q + \lambda^2}{r^2}\left(1 - \frac{2M}{r}\right)} , \tag{5.9}$$

$$\dot{\vartheta} = \pm r^2\sqrt{q - \lambda^2 \cot^2\vartheta} , \tag{5.10}$$

$$\dot{\varphi} = \frac{\lambda}{r^2 \sin^2\vartheta} . \tag{5.11}$$

In the following, selected physical properties of this solution are discussed.

When looking at purely radial motion, it is evident that $\dot{r}$ vanishes only at $r_c = 3M$, marking the position of the so-called photon sphere. The motion of light on the photon sphere is unstable, i.e. $\ddot{r}(r = r_c) < 0$. For most stellar objects, the outer radius is much greater than the Schwarzschild radius, thus this distance lies beneath its surface. For black holes, however, it is a valuable tool for observing the effects of gravitation of such dense objects.

Another phenomenon associated with light rays in curved spacetime is the light deflection. In the vicinity of gravitational fields, light is deflected on its path from and towards the surface of gravity. This effect forms the cornerstone of the field of gravitational lensing, where compact objects are used as lenses, bending the light of light sources from behind the line-of-sight between emitter and observer. Particularly, it allows the study of the physical properties of the compact objects in question.

An additional, notable effect is the gravitational time delay or Shapiro time delay. It describes the increase in the travel time of light in the vicinity of gravitational fields. Together with gravitational lensing, it is one of the first effects for which to conduct experiment to test general relativity.

Furthermore, the gravitational field influences the energy of the light. When moving out of the gravitational potential, a photon loses energy, which consequently decreases its frequency. This effect is called gravitational redshift, as the light observed appears "redder" than the emitted light. For purely radial light rays from a static emitter to an static observer in Schwarzschild spacetime, the redshift due only to the gravitational field alone can be calculated to be

$$1 + z = \sqrt{\frac{1 - \frac{2M}{r_{\mathrm{obs}}}}{1 - \frac{2M}{r_{\mathrm{em}}}}} , \tag{5.12}$$

where r_{obs} is the radial position of the observer, and r_{em} is the radial position of the emitter.

The following section covers the theoretical description of an spinning emitter in Schwarzschild background in particular.

5.2 Emission of spinning light source in equatorial plane of a Schwarzschild object

In this section, the general theory of spinning light sources in the equatorial plane of any stationary, axially symmetric spacetime, as described in chapter 3, is applied to the static, asymptotically flat solution to Einsteins vacuum field equations, the Schwarzschild spacetime introduced in the previous section.

The first subsection covers the notion of static observers in Schwarzschild spacetime, which are the basis for describing any physical observer for a point in spacetime (cf. sec. 3.1.1).

In the second subsection, the solution of the MPD-equations (cf. ch. 2) for spinning test bodies in the symmetry plane of a Schwarzschild object is discussed in detail, and the centre of mass reference frame (cf. sec. 3.1.2) for this particular case is established.

The third and last subsection is dedicated to describing the mathematical and physical properties of the relative velocity for a spinning light source on a Schwarzschild background, giving rise to the centre of momentum reference frame (cf. sec. 3.1.3), being the basis for the SRF reference frame.

In particular, the emitter is assumed to orbit in the symmetry plane of the Schwarzschild object $\vartheta = \pi/2$; in the context of this thesis, it will be called the equatorial plane.

5.2.1 Static observers in Schwarzschild spacetime

For any point in spacetime, a static observer, as defined following the flow of the Killing vector field ∂_t, can be described by an orthonormal tetrad. Following the description of Eq. (3.5), it can be written as

$$e^{\lambda}_{(a)} = \begin{pmatrix} \left(\sqrt{1-\frac{2M}{r}}\right)^{-1} & 0 & 0 & 0 \\ 0 & \sqrt{1-\frac{2M}{r}} & 0 & 0 \\ 0 & 0 & \frac{1}{r} & 0 \\ 0 & 0 & 0 & \frac{1}{r\sin\vartheta} \end{pmatrix}, \tag{5.13}$$

$$e^{(a)}_{\lambda} = \begin{pmatrix} \sqrt{1-\frac{2M}{r}} & 0 & 0 & 0 \\ 0 & \left(\sqrt{1-\frac{2M}{r}}\right)^{-1} & 0 & 0 \\ 0 & 0 & r & 0 \\ 0 & 0 & 0 & r\sin\vartheta \end{pmatrix}. \tag{5.14}$$

It is easily verifiable that the spacetime, as measured in this frame, is flat, i.e. $e^{\mu}_{(a)} e^{\nu}_{(b)} g_{\mu\nu} = \eta_{(a)(b)}$ with $\eta = \mathrm{diag}(-1,\ 1,\ 1,\ 1)$.

5.2.2 MPD equations in the symmetry plane of a Schwarzschild object

In this section, the solution of the MPD equations in the equatorial plane of a Schwarzschild object for a spinning test particle in circular motion is discussed. The spin of the test particle is assumed to be (anti-)parallel to the orbital angular momentum.

First, a short summary on the derivation of the solution is given, following the approach of Tanaka et al. [37].

It is convenient to give the equations of motion in terms of the static reference frame, described in the previous subsection. For an arbitrary vector f^κ, the following relation holds:

$$e^{(a)}_\kappa \frac{\mathrm{D}}{\mathrm{D}\tau} f^\kappa = \frac{\mathrm{d}}{\mathrm{d}\tau} f^{(a)} - w_{(b)(c)}{}^{(a)} v^{(b)} f^{(c)} \,, \tag{5.15}$$

where $\frac{\mathrm{D}}{\mathrm{D}\tau}$ is the covariant derivation. The components of w are defined via the components of the orthonormal tetrad and its derivative, i.e.

$$w_{(a)(b)}{}^{(c)} := e^\kappa_{(a)} e^\rho_{(b)} e^{(c)}_{\rho;\kappa} \,, \tag{5.16}$$

where $e^{(c)}_{\rho;\kappa} = \nabla_\kappa e^{(c)}_\rho$ is defined as the derivative of the components of the orthonormal tetrad. Then, the equations of motion reduce to

$$\frac{\mathrm{d}U^{(a)}}{\mathrm{d}\tau} = w_{(b)(c)}{}^{(a)} V^{(b)} U^{(c)} - \hat{S} R^{(a)} \,, \tag{5.17}$$

$$\frac{\mathrm{d}S^{(a)}}{\mathrm{d}\tau} = w_{(b)(c)}{}^{(a)} V^{(b)} S^{(c)} - \hat{S} U^{(a)} S^{(b)} R_{(b)} \,, \tag{5.18}$$

where $U := P/\mu$ is the normalized four-velocity associated with the four-momentum, V is the tangent of the world line of the particle, $\hat{S}$ is the magnitude of the spin and $S^{(a)}$ is the unit spin vector; for a detailed introduction of these quantities, see chapter 2. Specifically, $R^{(a)}$ is defined as

$$R^{(a)} = \frac{1}{2\mu\hat{S}} R^{(a)}{}_{(b)(c)(d)} V^{(b)} S^{(c)(d)} \,, \tag{5.19}$$

where $R_{(a)(b)(c)(d)}$ is the Riemann tensor.

For a spinning particle in the equatorial plane $\vartheta = \pi/2$ of a Schwarzschild object, one can now compute all non-vanishing components of w:

$$w_{(0)(1)}{}^{(0)} = w_{(0)(0)}{}^{(1)} =: w_1 = -\frac{M}{r^2}\sqrt{\frac{r}{r-2M}} \,, \tag{5.20}$$

$$w_{(2)(2)}{}^{(1)} = -w_{(2)(1)}{}^{(2)} = w_{(3)(3)}{}^{(1)} = -w_{(3)(1)}{}^{(3)} =: w_2 = \frac{1}{r}\sqrt{\frac{r-2M}{r}} \,. \tag{5.21}$$

$$\tag{5.22}$$

Similarly, the only non-vanishing components of the Riemann tensor in the equatorial plane can be calculated to be

$$R_{(0)(1)(0)(1)} = -R_{(2)(3)(2)(3)} = -\frac{r-2M}{r^3} \,, \tag{5.23}$$

$$R_{(0)(2)(0)(2)} = R_{(0)(3)(0)(3)} = -R_{(1)(2)(1)(2)} = -R_{(1)(3)(1)(3)} = \frac{r-2M}{2r^3} \,. \tag{5.24}$$

Due to assumption that the orbit is circular ($V^{(1)} = V^{(2)} = 0$) and in the equatorial plane ($\vartheta = \pi/2$), the only non-vanishing component of the spin vector is $S^{(2)} := -\mathcal{S}/\hat{S}$. Using the mass conservation (cf. Eq. (2.10)) and normalization condition (cf. Eq. (2.14)), it is notable that $U^{(1)} = U^{(2)} = 0$, by calculating the time derivative of the centre of mass condition (cf. Eq. (2.5)).

Then, all but one equation of the set in Eq. (5.17) vanish trivially, leaving

$$\frac{\mathrm{d}U^1}{\mathrm{d}t} = w_1 V^{(0)} U^{(0)} + w_2 V^{(3)} U^{(3)} + \mathcal{S}\frac{M}{r^3}\left(2V^{(0)}U^{(3)} + V^{(3)}U^{(0)}\right) = 0\,. \tag{5.25}$$

To solve this equation, it is convenient to introduce a set of new variables, namely

$$\chi_v := \frac{V^{(3)}}{V^{(0)}} \quad \text{and} \quad \chi_u := \frac{U^{(3)}}{U^{(0)}} \quad \text{and} \quad s = \frac{\mathcal{S}}{M}\,. \tag{5.26}$$

Particularly, the quantity s is the dimensionless spin parameter; all equations in the following discussion regarding spinning light sources in Schwarzschild spacetime will be given in terms of s.

For a spinning test particle on a circular orbit in the equatorial plane of a Schwarzschild object, the following solution can be obtained:

$$\chi_v = \frac{-3M^2 s \pm \sqrt{4Mr^3 + 13M^4 s^2 - 8M^7 s^4/r^3}}{2\sqrt{r^2 - 2Mr}(r - M^3 s^2/r^2)}\,, \tag{5.27}$$

$$\chi_u = \frac{r - M^3 s^2/r^2}{r + 2M^3 s^2/r^2} \cdot \chi_v\,. \tag{5.28}$$

Using again the mass conservation and normalization condition, one can obtain the solution on terms of U and V, namely

$$U^{(0)} = \frac{1}{\sqrt{1-\chi_u^2}}, \qquad U^{(3)} = \frac{\chi_u}{\sqrt{1-\chi_u^2}} \tag{5.29}$$

$$V^{(0)} = \frac{\sqrt{1-\chi_u^2}}{1-\chi_v\chi_u}, \qquad V^{(3)} = \frac{\chi_v\sqrt{1-\chi_u^2}}{1-\chi_v\chi_u}\,. \tag{5.30}$$

A few remarks can be made regarding this solution. For large values of the fraction s/r, the root of χ_v is not positive definite; in this limit, there are no circular orbits. For every physically reasonable values of s/r; however, they always exist. In particular, the quantities χ_v and χ_u differ only slightly for physically expected values of spin, which for most physical applications is much less than unity. Consequently, the difference between V and U is small for very small spin values. Evidently, for vanishing spin, χ_v and χ_u coincide, and so do V and U.

Now, the centre of mass reference frame can be constructed. The orbital velocity is defined as $v := V^{(3)}/V^{(0)} = \chi_v$, which only depends on the spin parameter s, the distance to the origin r and the mass of the central object M. The tensors of transformation, i.e. the Lorentz transformation, from the static observer into the centre of mass reference frame and back is given in Eq. (3.10) ff.

The following section covers the description of the centre of momentum reference frame and the velocity between the V and U, which is directly related to the solution introduced above.

5.2.3 Relative velocity between four-velocity and normalized four-momentum in Schwarzschild background

In this section, the relative velocity for a spinning test particle in the equatorial plane of a Schwarzschild object is calculated in detail. The relative velocity arises as a consequence of the fact that the four-velocity and the normalized four-momentum are not parallel anymore in

using the Tulcziew-Dixon supplementary condition; for further details, see section 3.1.3.

The determining equation for the relative velocity is given by Eq. (3.17), and for convenience here again:

$$\mathcal{V}^2 = 1 + V_\nu V^\nu \,, \tag{5.31}$$

where V^ν is the four-velocity of the spinning test-particle. In the previous subsection, the four-velocity of a spinning test-particle in the equatorial plane of a Schwarzschild object is given, in particular Eqs. (5.29) ff. Evaluating the product above, one can easily find that

$$\mathcal{V}^2 = 1 - \frac{(1-\chi_v^2)(1-\chi_u^2)}{(1-\chi_u\chi_v)^2} \,. \tag{5.32}$$

Some important remarks shall be made here. For vanishing spin (see the discussion in the previous subsection), the quantities χ_u and χ_v coincide. Evidently, one can see that, in this case, the relative velocity vanishes too, in line with previous discussions. For small spin values much smaller than unity, which is the case in most physically appropriate settings, the relative velocity is only slightly larger than zero; in leading terms of s, the relative velocity is approximately given by

$$\mathcal{V}^2\Big|_{s=0} \approx \frac{288M^5(r-2M) \mp M^4 r(r^2-2Mr)^2(21r^3+12)}{2r(r^2-3Mr)^2(r-2M)} \cdot s^2 + \mathcal{O}(s^3) \,. \tag{5.33}$$

The full derivation is given in the appendix A.

5.3 Observables in Schwarzschild spacetime

In this section, the observables, introduced in section 3.2, are discussed in detail for a spinning emitter orbiting a Schwarzschild object. In particular, the dependence of the spin on these observables is studied.

Accordingly, a configuration of emitter and observer properties is required. This includes the observer position in spacetime, as well as the distance of the orbit of the emitter from the centre of the Schwarzschild object, as well as its geometrical properties. There are, in principal, no constraints on these parameters, as long as they abide the established theory; however, to study the effects of spin and gravity on the observables, it is possible to reason some preferences.
As a natural scale of distances, all lengths are given in units of the mass of the central object, namely M. Additionally, the spin of the emitter is specified by the dimensionless spin parameter, defined as

$$s = \frac{\mathcal{S}}{M} \,. \tag{5.34}$$

The emitter is orbiting the Schwarzschild object in the equatorial plane $\vartheta_{\mathrm{em}} = \pi/2$ at a distance of $r_{\mathrm{em}} = 8M$. The distance is chosen such that it is far enough away to not interfere with the innermost stable circular orbit at $r_{\mathrm{isco}} = 6M$ for a spinless test particle, and is close enough to observe the effects of the strong gravitational field on the light, in particular the bending of the light curve.
The location of the observer is chosen to be at $r_{\mathrm{obs}} = 35M$, elevated above the symmetry plane at $\vartheta_{\mathrm{obs}} = \pi/3$. As the theory does not limit the observer's position to be at infinity, the distance is chosen to be finitely but moderately far away from the source of light. Additionally, the observer is chosen to not be in the equatorial plane in order to study the effect of an inclination of the observer on the observables, and to limit the discussion regarding multiple images of

the emitter to only using the primary image.
The geometrical extension of the emitter is chosen to be $\rho = 0.005M$, if the emitter is spherical, and $A = 0.005M$, if the emitter is described by a Maclaurin spheroid. This scale of geometry is chosen to be small enough to abide the test particle approximation for the MPD equations and its size limit, see Eq. (2.13), but large enough to uphold numerical constraints discussed in section 3.3. The size of the emitter then, following Eq. (4.5) and (4.19), determines the maximally allowed value of the spin parameter. Thus, due to the Möller limit, the maximum spin of a spinning object with a scale of geometry of $\{A,\ \rho\} = 0.005M$ is $|s_{\text{max}}| = 0.002$.

Screen coordinates for a static observer in Schwarzschild spacetime

In order to simulate the recording of the observables at the observer, the notion of a celestial sphere and observer screen has to be established for a static observer in Schwarzschild spacetime specifically, following the description in section 3.2.1.

Recall that the celestial sphere is described by the azimuth coordinate $\Phi \in [0,\ 2\pi)$ and the polar coordinate $\Theta \in [-\pi/2,\ \pi/2]$, see Eqs. (3.58) ff. These coordinates are determined by the four-velocity of the lightlike geodesic, see Eqs. (5.17), and can be written as

$$\cos\Theta = -\frac{\dot{r}}{\zeta}\sqrt{\frac{r}{r-2M}}\,, \qquad \sin\Theta = \sqrt{1-\frac{\dot{r}^2}{\zeta^2}}\,, \tag{5.35}$$

$$\cos\Phi = \frac{r\dot{\vartheta}}{\sqrt{\zeta^2-\dot{r}^2}}\,, \qquad \sin\Phi = -\frac{r\sin\vartheta\dot{\varphi}}{\sqrt{\zeta^2-\dot{r}^2}}\,, \tag{5.36}$$

where

$$\zeta = g(\dot{\lambda}, \mathbf{e}_{(0)}) = -E\sqrt{\frac{r}{r-2M}}\,. \tag{5.37}$$

The screen coordinates α and β are then defined by stereographic projection; recall from Eq. (3.60):

$$\alpha := -2\frac{(1-\cos\Theta)}{\sin\Theta}\sin\Phi\,, \tag{5.38}$$

$$\beta := 2\frac{(1-\cos\Theta)}{\sin\Theta}\cos\Phi\,. \tag{5.39}$$

Structure of the following section

This section is structured as follows:

First, the influence of the spin on the velocities, namely the orbital and relative velocity, is studied.

Next, the dependency of the spin on the redshift is studied. In this context, the influence of spin and the different velocities on the redshift distribution is discussed, and the redshift distribution of spherical and spheroidal emitters is compared.

Afterwards, the influence of the spin on the polarization vector is studied, where the notion of the polarization vector and the parallel transport of it, in Schwarzschild spacetime in particular, is discussed in more detail.

Lastly, the effect of the spin on the observed flux is studied for monochromatic light sources. Here, the fluxes of spherical and spheroidal emitter are compared as well.

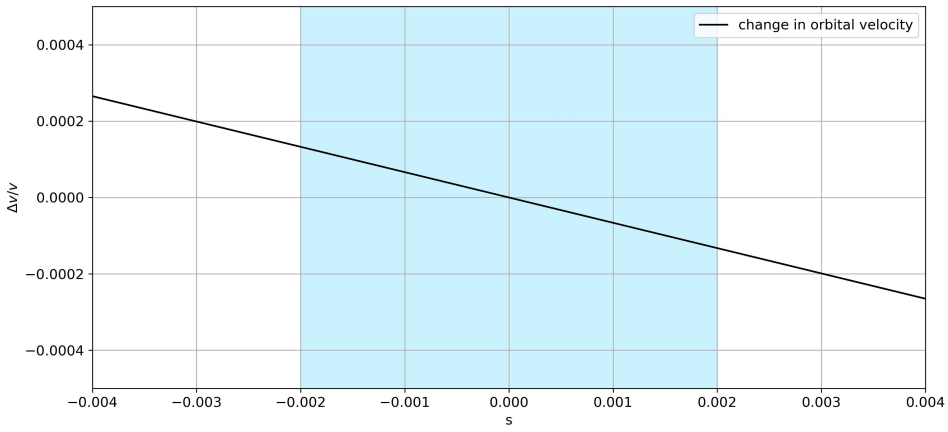

Figure 5.1: Change in orbital velocity $\triangle v/v$ relative to the spinless case, dependent on the spin of the emitter. The blue shaded area indicates the range of spin allowed for an emitter with a scale of geometry of $0.005M$.

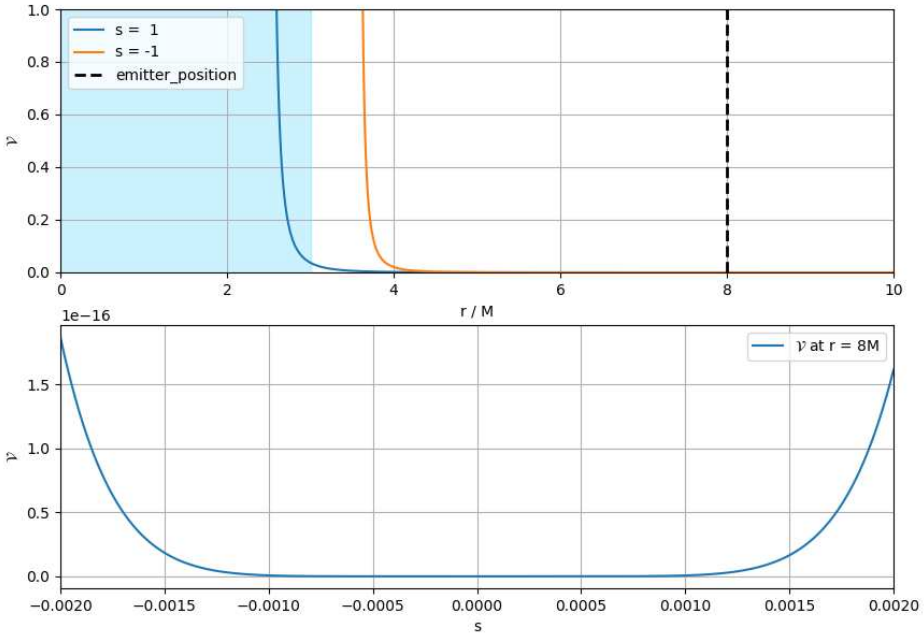

Figure 5.2: Graphical depiction of the relative velocity $\mathcal{V}$.
Top: dependence of the relative velocity on the distance to the origin of the Schwarzschild object. Blue: relative velocity for an (physically improbable) emitter with spin $s = 1$; red: relative velocity for an (physically improbable) emitter with spin $s = -1$. The black dashed line indicates the position of the emitter $r = 8M$ chosen throughout this thesis.
Bottom: relative velocity at the orbital position of the emitter $r = 8M$, depending on the spin parameter s.

5.3.1 Influence of the spin on the velocities

In this section, the influence of the spin on the orbital velocity and relative velocity is studied.

Figure 5.1 depicts the change of orbital velocity, relative to the orbital velocity of a non-spinning emitter, depending on its spin. The blue shaded area indicates the region of spin that is in line with the Möller limit, see Eqs. (4.5) and (4.19) for the considered scale of the two emitter geometries, respectively. While it is possible to observe a change of v, as it is decreasing with increasing spin, the effect is rather small. For a small emitter, such is chosen to be in this thesis, the orbital velocity can be assumed to be constant. For numerical computations, however, the orbital velocity is inserted exactly.

In figure 5.2, the relative velocity, depending on the spin and distance, is depicted. The top panel of the figure shows the relative velocity depending on the distance to the source of gravity, for two different spin values. Both lines indicate physically unrealistic values of spin of ± 1, which diverges between $r = 2M$ and $r = 4M$, as the orbit becomes lightlike. The high values of spin parameter are chosen to demonstrate the fact that the relative velocity drops off strongly at the marginally stable circular orbit ($r_{\mathrm{ms}}(s = 0) = 6M$) and beyond. The black line indicates the position of the emitter throughout this thesis at $r_{\mathrm{em}} = 8M$.

This can be seen more clearly in the lower panel of figure 5.2, where the dependence of the spin on the relative velocity at $r_{\mathrm{em}} = 8M$ is depicted. Even at the edges of the graph, corresponding to the maximum allowed spin values $|s_{\mathrm{max}}| = 0.002$, the relative velocity does not exceed $2 \cdot 10^{-16}$. Thus, it is magnitudes lower than the orbital velocity, and its effect on the observables will be small, and can effectively be neglected. Still, the relative velocity is inserted exactly for all numerical computations.

The following section investigates the influence of the spin on the shape and redshift distribution of the emitter on the observer's screen.

5.3.2 Influence of the spin on the redshift

Redshift distribution for a spherical emitter

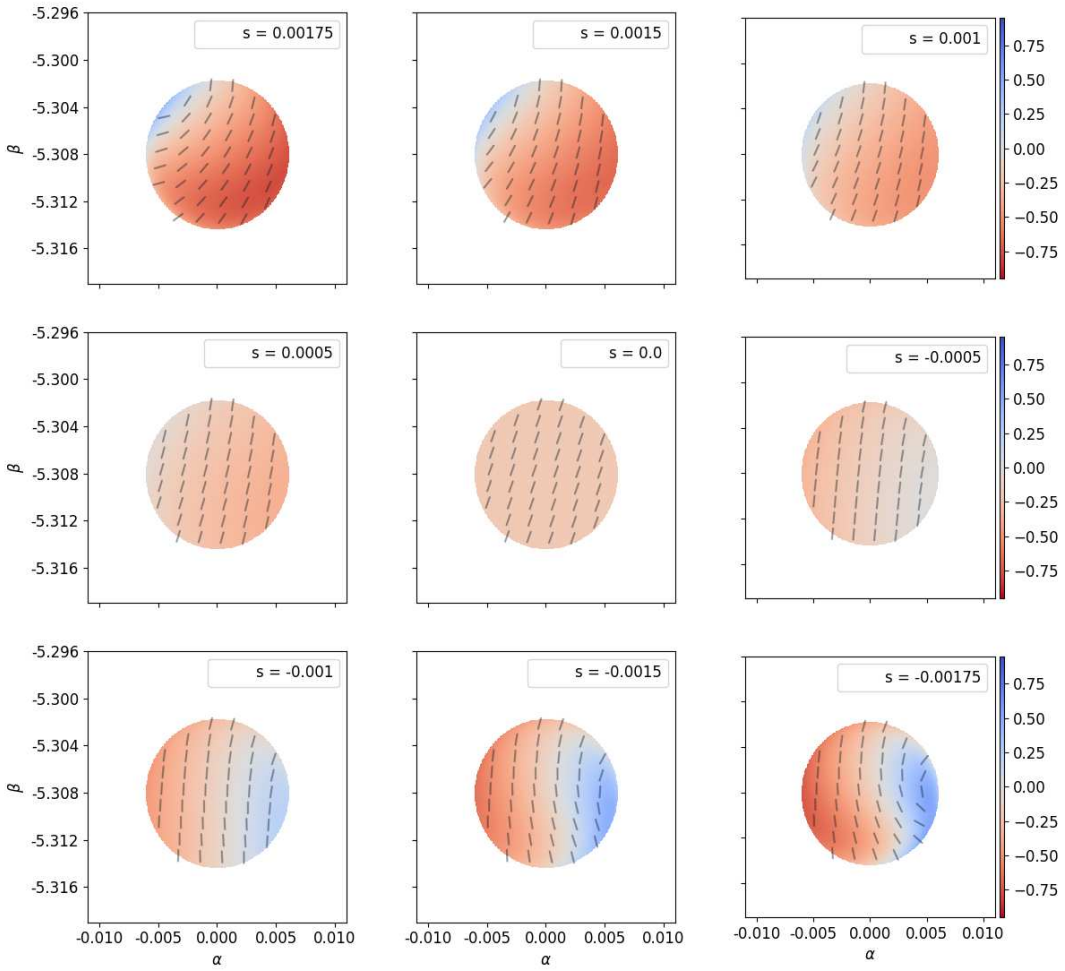

Figure 5.3: Redshift distribution of a spherical emitter for different spin values for an emitter in front of the compact object, i.e. $\varphi_{\mathrm{em}} = \varphi_{\mathrm{obs}} = 0$, on the observer's screen. Negative spin values correspond to counter-rotating emitters, while positive spin values correspond to co-rotating emitters. Colors indicate the magnitude of redshift z, while the grey bars indicate the shift of the polarization plane, see section 5.3.3.

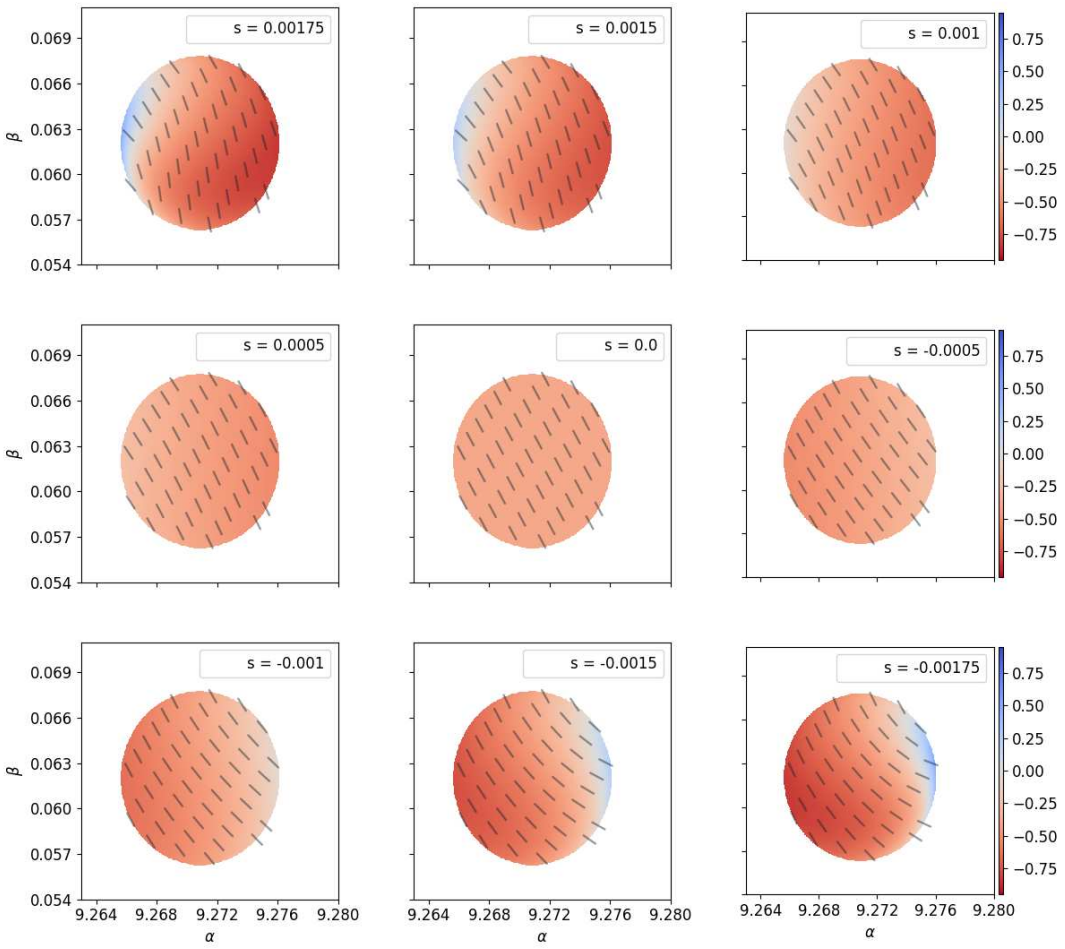

Figure 5.4: Redshift distribution of a spherical emitter for different spin values for an emitter at orbital position $\varphi_{\mathrm{em}} = \pi/2$, on the observer's screen. Negative spin values correspond to counter-rotating emitters, while positive spin values correspond to co-rotating emitters. Colors indicate the magnitude of redshift z, while the grey bars indicate the shift of the polarization plane, see section 5.3.3.

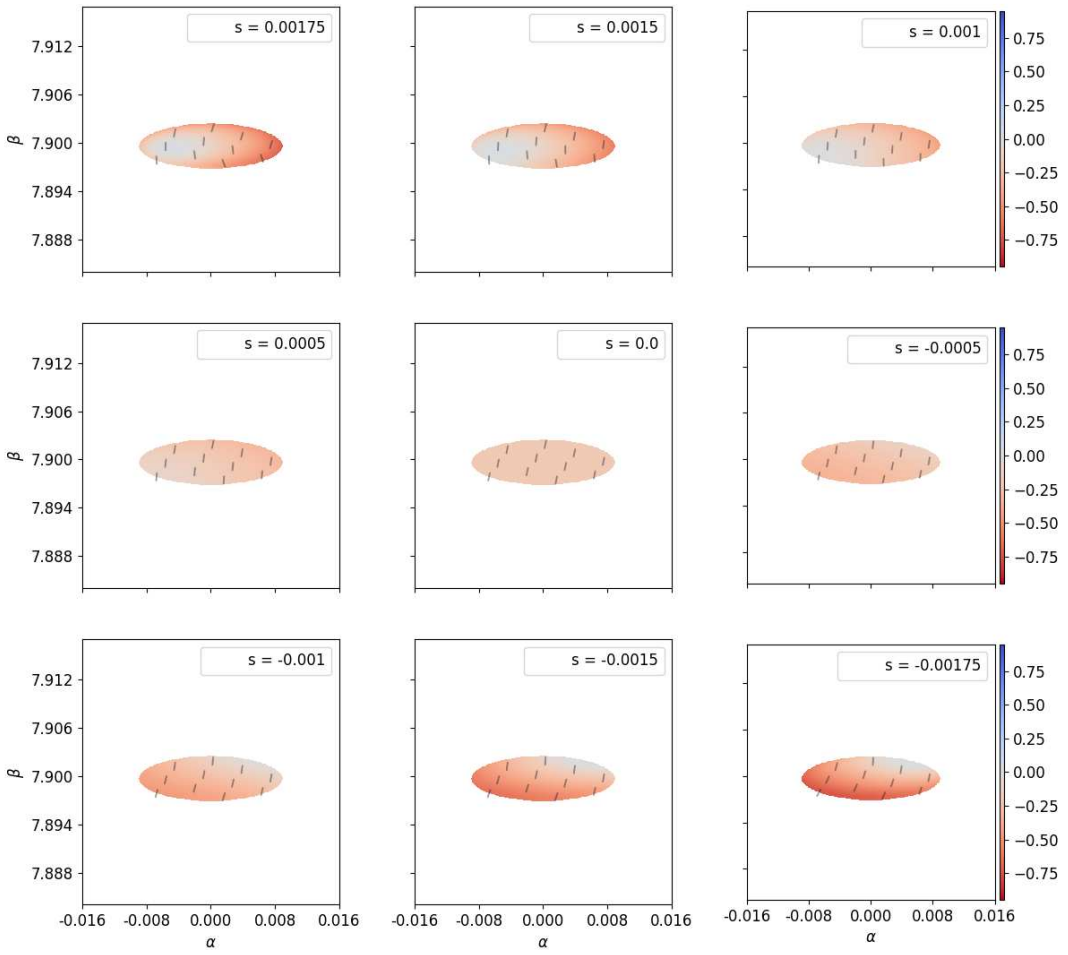

Figure 5.5: Redshift distribution of a spherical emitter for different spin values for an emitter behind of the compact object, i.e. $\varphi_{\mathrm{em}} = \pi$, on the observer's screen. Negative spin values correspond to counter-rotating emitters, while positive spin values correspond to co-rotating emitters. Colors indicate the magnitude of redshift z, while the grey bars indicate the shift of the polarization plane, see section 5.3.3.

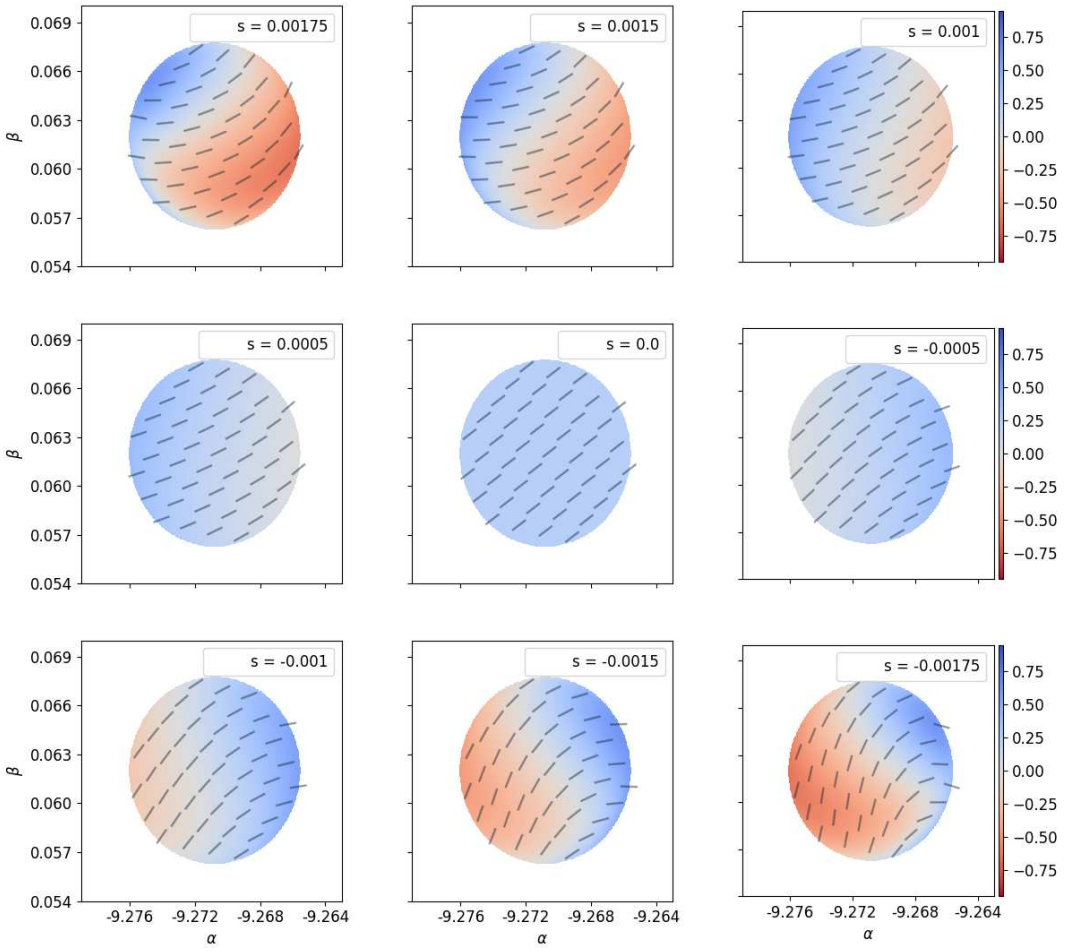

Figure 5.6: Redshift distribution of a spherical emitter for different spin values for an emitter at orbital position $\varphi_{\mathrm{em}} = 3\pi/2$, on the observer's screen. Negative spin values correspond to counter-rotating emitters, while positive spin values correspond to co-rotating emitters. Colors indicate the magnitude of redshift z, while the grey bars indicate the shift of the polarization plane, see section 5.3.3.

The information about the shape and redshift of the emitted light that reaches the observer and the influence of the spin on it can be seen in figures 5.3 to 5.10. Figures 5.3 to 5.6 depict the redshift distribution for a spherical emitter, while figures 5.7 to 5.10 show the distribution for a spheroidal emitter.
Thus, there are 4 figures for each emitter geometry; every set of four images is composed of an image of the emitter for $\varphi_{\mathrm{em}} \in \{0,\ \pi/2,\ \pi,\ 3\pi/2\}$ in ascending order. In particular, if $\varphi_{\mathrm{em}} = \varphi_{\mathrm{obs}} = 0$, the emitter is in front of the Schwarzschild object, while at $\varphi_{\mathrm{em}} = \pi$, it is exactly behind the source of gravity, relative to the observer.
Every figure is composed of 9 panels, where each panel represents the image of the emitter at different spins, ranging from $s = 0.00175$ to $s = -0.00175$, still below the maximal spin value at $|s_{\mathrm{max}}| = 0.002$. Note that positive values of s correspond to co-rotating emitters, while negative values of s correspond to counter-rotating emitters, relative to the direction of orbit rotation.
Each panel consists of a colored shape, which is the observed shape of the emitter on the observer's screen. The image is plotted in terms of the stereographic projection of the screen coordinates, namely (α, β); see the beginning of section 5.3. For a sense of direction of orbit, the emitter moves on the observer's screen on its orbit in positive α-direction if the emitter is in front of the compact object, and in negative α-direction if the emitter is behind the source of gravity. The color corresponds to the redshift z of the received light, where blue colors indicate positive redshift, i.e. the frequency of the light is increased, relative to the emitted frequency, and red colors indicate negative redshift, i.e. the frequency of the observed light is decreased. Additionally, every panel shows the distribution of the plane of polarization by gray bars on top of the redshift distribution, which is discussed in detail in the following section 5.3.3.

First, consider the spinless case, in particular for a spherical emitter. This corresponds to the middle panels of figures 5.3 to 5.6.
If the emitter is in front of the Schwarzschild object (cf. figure 5.3), the path of the light from the emitter to the observer is bent only slightly, thus the shape of the emitter on the observer's screen appears spherical, similar to the purely special relativistic case, where the shape of any spherical object is conserved, cf. Penrose [60]. The emitter is observed around $\alpha \approx 0$, as it is in front of the source of gravity, and observed at negative values of β, because the observer is located not in the equatorial plane $\vartheta = \pi/2$, but at an inclination above it, namely $\vartheta_{\mathrm{obs}} = \pi/3$. However, due to its small size, i.e. $\rho = 0.005M$, the extension of the emitter on the observer's screen is small. The redshift distribution is nearly uniform and the redshift negative, as the light has to move out of the gravitational potential of the central object, losing energy and therefore frequency in the process. This effect is known as gravitational redshift.
If the emitter is at $\varphi_{\mathrm{em}} = \pi/2$ or $\varphi_{\mathrm{em}} = 3\pi/2$ (cf. figure 5.4 and 5.6), the shape of the emitter is elongated vertically. This is due to the fact that, in order to reach the observer, the path of the light is bent by the gravitational field of the Schwarzschild object, resulting in an non-spherical image. The redshift distribution for both orbit positions is nearly uniform; however, for $\varphi_{\mathrm{em}} = \pi/2$, the redshift is negative, while it is positive for $\varphi_{\mathrm{obs}} = 3\pi/2$. This effect can be explained by the Doppler shift due to the orbital velocity: at $\varphi_{\mathrm{em}} = \pi/2$, the emitter is moving away from the observer, resulting in a decrease in frequency of the observed light, relative to the emitted frequency. If the emitter is at $\varphi_{\mathrm{em}} = 3\pi/2$, it is moving towards the observer, resulting in a positive frequency shift.
The most extreme case of an non-spherical image can be obtained if the emitter is behind the source of gravity, namely $\varphi_{\mathrm{em}} = \pi$, cf. figure 5.5. Here, the emitter is observed again around $\alpha \approx 0$, but at positive values of β, due to the fact that the observer is at inclination $\vartheta_{\mathrm{obs}} = \pi/3$ and $\beta = 0$ corresponding to the direction towards the centre of gravity. The image of the spherical emitter is elongated horizontally on the observer's screen, forming a

nearly elliptical shape. The path of the light here is bent strongly by the central object; it appears higher on the observer's screen than is expected, and its shape is visibly non-spherical.

Next, the influence of the spin on the redshift is discussed, again in particular for a spherical emitter.
Most of the following discussion applies for every orbit position, thus the influence of the spin is studied exemplary if the emitter is in front of the Schwarzschild object, i.e. figure 5.3. It is clearly visible that for non-vanishing spin, the redshift distribution is no longer uniform, and this effect is stronger for increasingly co- and counter-rotating emitters. Thus, the strongest impact on the redshift distribution is introduced by the surface velocity; if the emitting surface element is moving towards the observer, the frequency of the observed light relative to the emitted light is increased, while the opposite is true if the emitting surface element is moving away from the observer. In the case that the emitter is in front of the source of gravity, the emitter moves to positive values of α, thus the surface elements on the right of a co-rotating emitter is away from the observer, while surface elements on the left move towards the observer. By similar argument, the opposite is true for a counter-rotating emitter. This line of reasoning is reflected in the redshift distributions for co- and counter-rotating emitters and is best seen for $|s| = 0.00175$. Additionally, it is important to note that the redshift distribution is not symmetrical to a thought symmetry line on the image of the emitter on the observer's screen due to inclination of the observer; lines with constant latitude on the emitter surface project to (non-closed) ellipses on the observer's screen. Furthermore, this inclination allows us to observe the emitters surface from above; observing the pole corresponds to redshift values that are equal to the spinless case.
As stated before, this line of reasoning holds for all orbit positions, where the effect of the orbital velocity is either amplified or de-amplified by the spin of the emitter. An important remark can be made for the case that the emitter is behind the Schwarzschild object; there, due to the deflection of the light path, parts of the back side of the emitter can be seen on the observer's screen.

Following this, the effect of the shape of the emitter on the observables is discussed.

Redshift distribution for a spheroidal emitter

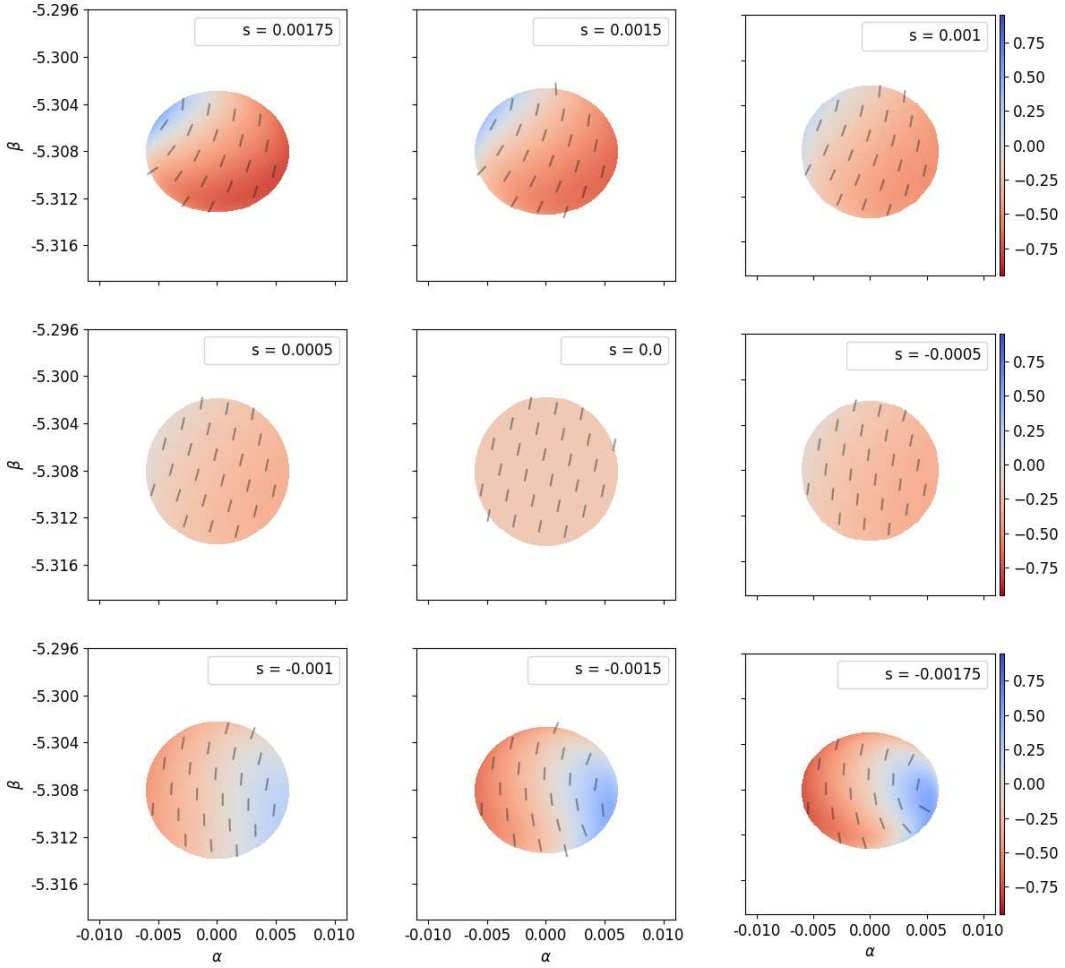

Figure 5.7: Redshift distribution of a spheroidal emitter for different spin values for an emitter in front of the compact object, i.e. $\varphi_{\mathrm{em}} = \varphi_{\mathrm{obs}} = 0$, on the observer's screen. Negative spin values correspond to counter-rotating emitters, while positive spin values correspond to co-rotating emitters. Colors indicate the magnitude of redshift z, while the grey bars indicate the shift of the polarization plane, see section 5.3.3.

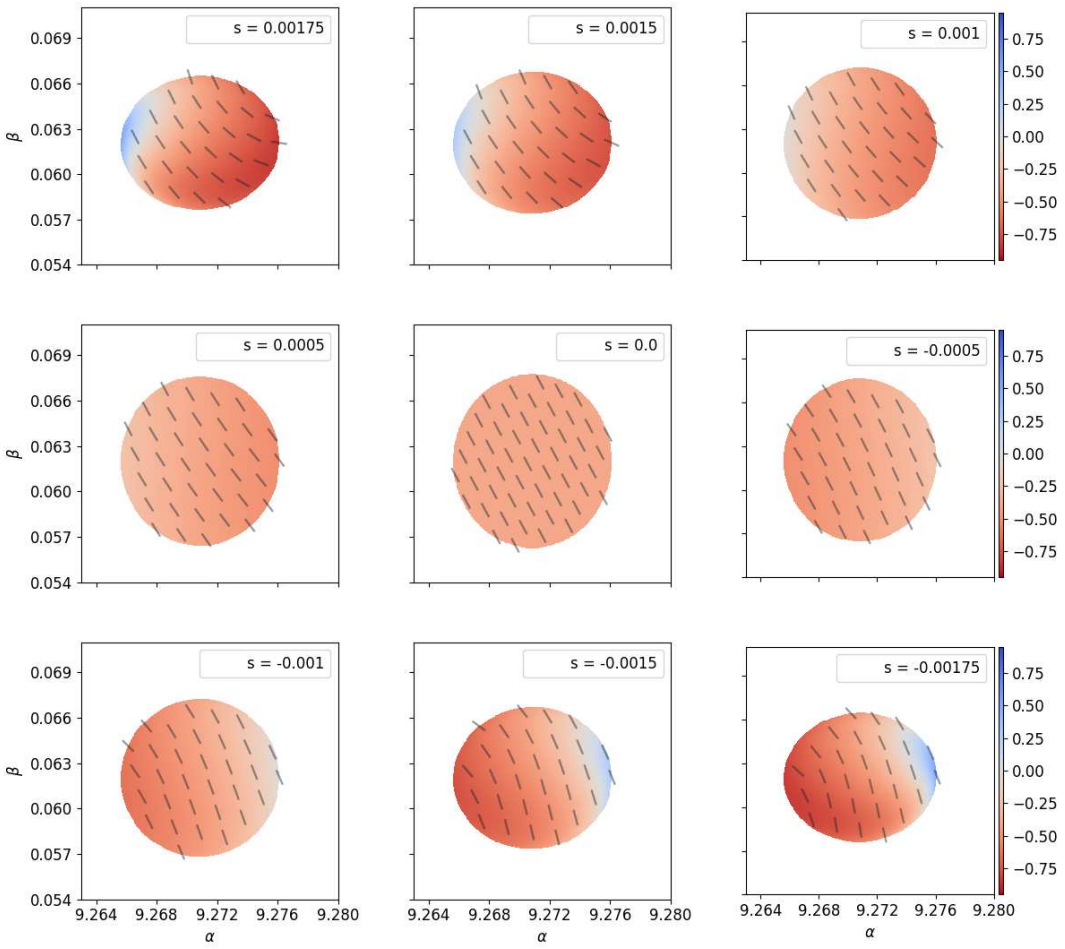

Figure 5.8: Redshift distribution of a spheroidal emitter for different spin values for an emitter at orbital position $\varphi_{\mathrm{em}} = \pi/2$, on the observer's screen. Negative spin values correspond to counter-rotating emitters, while positive spin values correspond to co-rotating emitters. Colors indicate the magnitude of redshift z, while the grey bars indicate the shift of the polarization plane, see section 5.3.3.

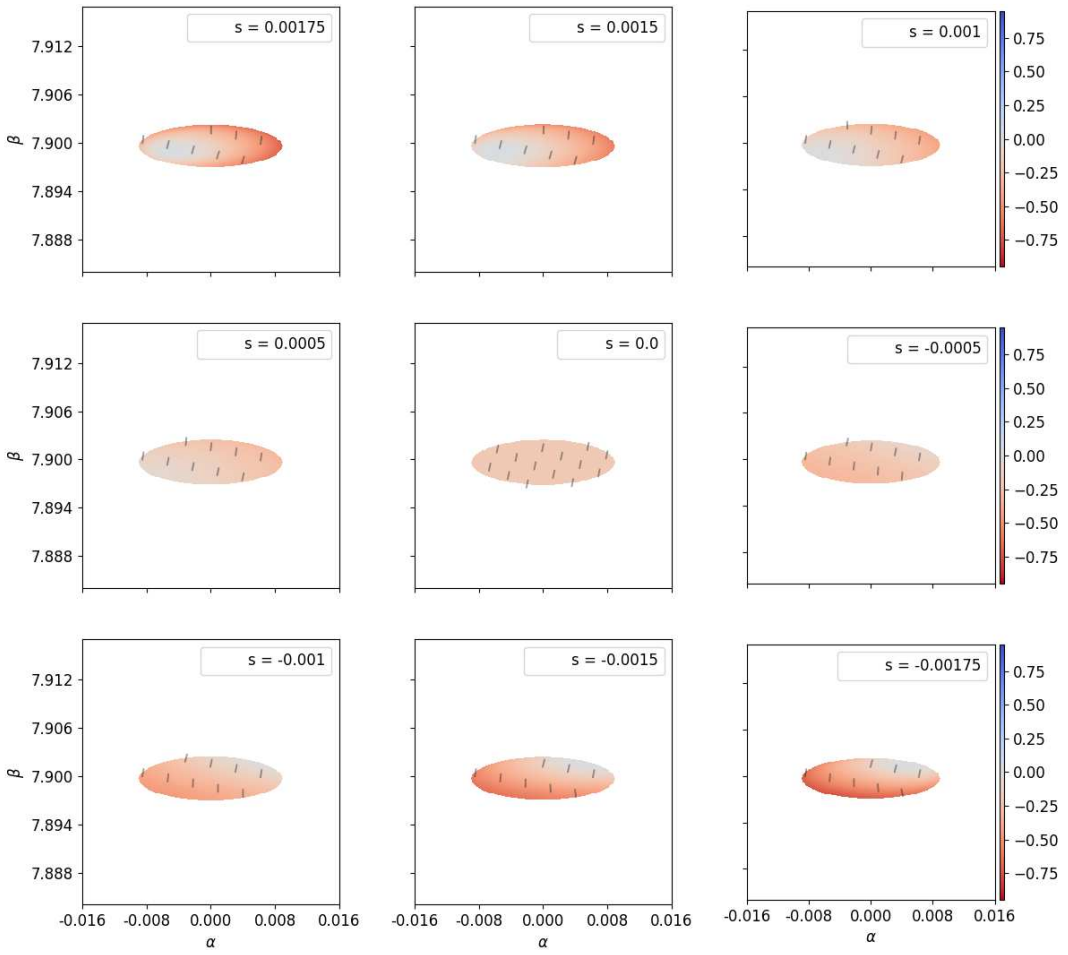

Figure 5.9: Redshift distribution of a spheroidal emitter for different spin values for an emitter behind of the compact object, i.e. $\varphi_{\mathrm{em}} = \pi$, on the observer's screen. Negative spin values correspond to counter-rotating emitters, while positive spin values correspond to co-rotating emitters. Colors indicate the magnitude of redshift z, while the grey bars indicate the shift of the polarization plane, see section 5.3.3.

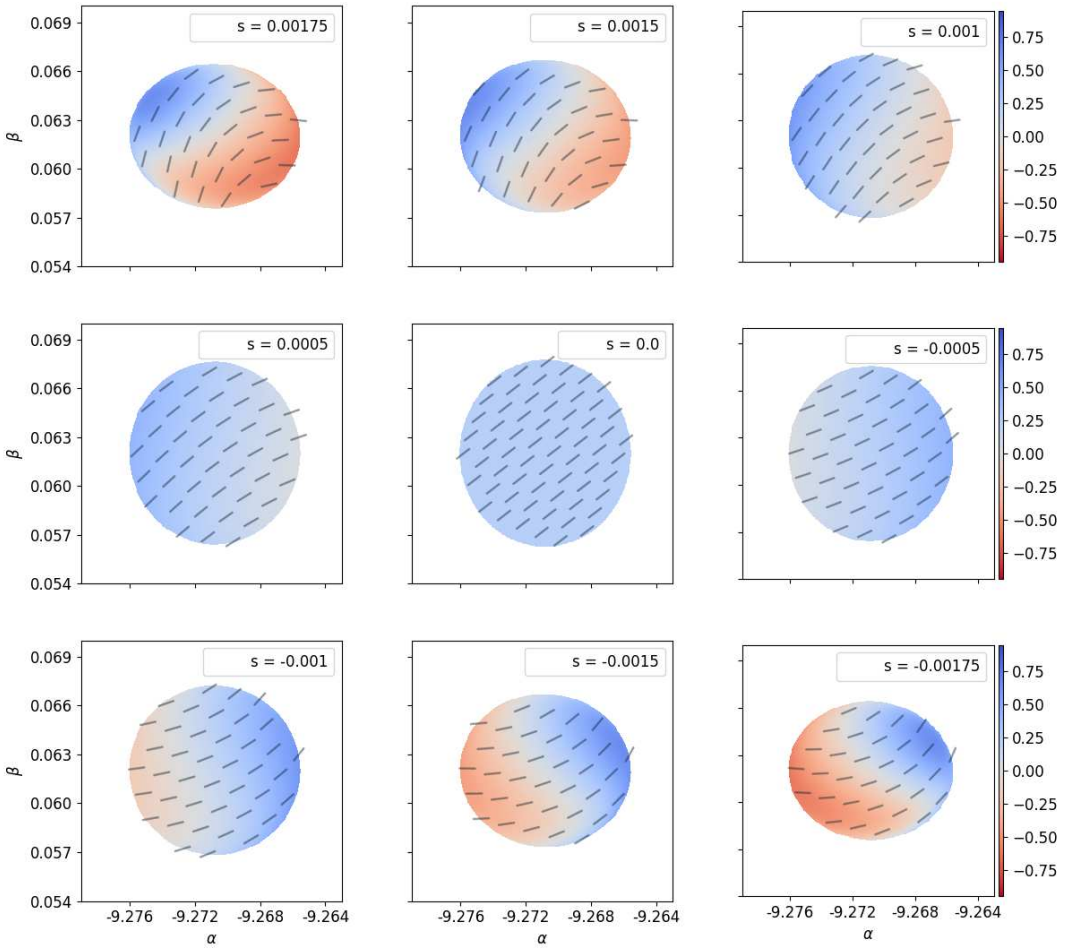

Figure 5.10: Redshift distribution of a spheroidal emitter for different spin values for an emitter at orbital position $\varphi_{\mathrm{em}} = 3\pi/2$, on the observer's screen. Negative spin values correspond to counter-rotating emitters, while positive spin values correspond to co-rotating emitters. Colors indicate the magnitude of redshift z, while the grey bars indicate the shift of the polarization plane, see section 5.3.3.

The influence of the geometry of the emitter can be seen in figures 5.7 to 5.10. In particular, it is clear to see that, for highly co- and counter-rotating emitters, the image of the emitter on the screen is non-spherical, as the geometry of the emitter itself changes from spherical in the spinless case to spheroidal for high absolute spin values. This matches the theoretical considerations introduced in section 4.2. Specifically, the semi-minor axis C for the highest spin case of $|s| = 0.00175$ for the mass smaller than the critical mass ratio (cf. Eq. (4.21)) is $c \approx 0.00327M$; recall that the semi-major axis is fixed at $a = 0.005M$. The extent of this eccentricity is not fully reflected in the figures, as the emitter is observed from above, thus the shape is less elliptical than would be the case if the light source was observed edge-on. The influence of the spin on the redshift distribution for a spheroidal emitter still follows the line of reasoning introduced above.
Peculiarly, the shape of the image of the emitter on the observer's screen at $\varphi_{\mathrm{em}} = \pi/2$ and $\varphi_{\mathrm{em}} = 3\pi/2$ changes from elongated vertically to elongated horizontally, being nearly spherical for certain values of spin in between. Additionally, the change of shape for highly

co- and counter-rotating emitters is minimal if the emitter is behind the Schwarzschild object; the effect of the light bending is stronger.

5.3.3 Influence of the spin on the polarization

In this subsection, the polarization angle of radiation coming from spinning light sources in Schwarzschild spacetime is discussed in detail. The theoretical description follows the one outlined in section 3.2.2.

Recall that the light is assumed to be linearly polarized, parallel to $e^{\{2\}}$, as measured in the SRF, and is given by Eq. (3.64); the polarization vector is given here for reading convenience only:

$$f^{\{d\}} = N \cdot \left(-1\,, \quad 0\,, \quad \frac{p_{\{0\}}}{p_{\{2\}}}\,, \quad 0 \right). \tag{5.40}$$

Again, $p_{\{d\}}$ describes the four-momentum (see Eq. (5.8) - (5.11)) of the lightlike geodesic, transformed into the SRF system, and N is the normalization constant fixed in Eq. (3.66). Assuming that the light ray between the emitter and observer is found by the scheme introduced in chapter 3, the constants of motion are known, and if the spin is chosen, the components of the polarization vector, measured in the SRF system, are uniquely determined.

In order to calculate the polarization angle at the observer, the polarization vector has to be evaluated at the position of the observer. The 4 non-trivial determining equations for the spacetime components of the polarization vector in Schwarzschild spacetime specifically are given as

$$\kappa_1 = r\left(k^t f^r - k^r f^t\right)\,, \tag{5.41}$$

$$\kappa_2 = -r^3\left(k^\varphi f^\vartheta - k^\vartheta f^\varphi\right)\,, \tag{5.42}$$

$$1 = -g_{tt}\left(f^t\right)^2 + g_{rr}\left(f^r\right)^2 + g_{\vartheta\vartheta}\left(f^\vartheta\right)^2 + g_{\varphi\varphi}\left(f^\varphi\right)^2\,, \tag{5.43}$$

$$0 = -g_{tt} f^t k^t + g_{rr} f^r k^r + g_{\vartheta\vartheta} f^\vartheta k^\vartheta + g_{\varphi\varphi} f^\varphi k^\varphi\,, \tag{5.44}$$

where $\kappa_{1,\,2}$ are the real and imaginary parts of the Penrose-Walker constant (cf. section 3.2.2 and [44, 61]), and $g_{\mu\nu}$ are the components of the metric tensor of the Schwarzschild solution. As described above, the components of the polarization vector, as measured in the SRF system, are assumed to be known, and by transforming $f^{\{d\}}$ back into spacetime coordinates, f^ν at the point of emission is assumed to be known as well. Consequently, the value of the Penrose-Walker constant can be calculated at the point of emission, and has to calculated only once, as it is conserved along the light ray. Thus, the value of κ_1 and κ_2 are known as well.

This set of equations can be solved analytically, giving rise to the components of the polarization vector anywhere along the geodesic, as long as the point of evaluation is specified.

For an arbitrary point in spacetime, these can be expressed as

$$f^t = \frac{T_{\text{nom}} \pm \alpha k^t (\beta (k^\varphi)^2 \sqrt{\Xi_{T1}} - (k^\vartheta)^2 \sqrt{\Xi_{t2}})}{r \cdot T_{\text{denom}}} , \tag{5.45}$$

$$f^r = \frac{R_{\text{nom}} \pm \alpha k^r (\beta (k^\varphi)^2 \sqrt{\Xi_{R1}} - (k^\vartheta)^2 \sqrt{\Xi_{R2}})}{r \cdot R_{\text{denom}}} , \tag{5.46}$$

$$f^\vartheta = \frac{\theta_{\text{nom}} \pm k^\vartheta \sqrt{\Xi_\theta}}{r^3 \cdot \theta_{\text{denom}}} , \tag{5.47}$$

$$f^\varphi = \frac{\phi_{\text{nom}} \pm k^\varphi \sqrt{\Xi_\phi}}{r^3 \cdot \phi_{demon}} , \tag{5.48}$$

and

$$\alpha = 1 - \frac{2M}{r} , \qquad \beta = \sin^2 \vartheta . \tag{5.49}$$

The full derivation, along with the definition of the terms described above, is given in appendix A.3.1, and the polarization angle at the observer can be calculated by the scheme introduced in section 3.2.

The information on the polarization plane and the influence of the spin on it can be seen in figures 5.3 to 5.10. There, the distribution of the plane of polarization on the image of the emitter is indicated by the grey bars, which are plotted on top of the redshift distribution; see section 5.3.2. Figures 5.3 to 5.6 depict the distribution of the plane of polarization for a spherical emitter, while figures 5.7 to 5.10 show the distribution for a spheroidal emitter. It is important to note that the relative strength of the polarization is not depicted.

For a spinless emitter, the plane of polarization is uniformly distributed along the image of the emitter on the observer's screen. If the emitter is in front of the Schwarzschild object (cf. figures 5.3 and 5.7), the plane of polarization is tilted slightly to the right, relative to the positive β-axis to which the polarization angle is evaluated. This effect is due to the orbital velocity; the φ-component of the polarization vector at the point of emission in spacetime coordinates becomes non-zero, following the inverse Lorentz transformation to transform $f^{\{d\}}$ to f^μ. Therefore, the polarization vector has, in general, a non-vanishing φ-component along the lightlike geodesic, including the observer's position in spacetime.
Further velocities of a spinning surface element introduce a shift in all the components of the polarization vector at emission in spacetime coordinates, except f^ϑ. In general, the plane of polarization follows the surface velocity distribution, mimicking the redshift distribution. The plane of polarization generally also shifts along the orbit, making a full revolution along one orbit.

This is a very simple model of initial polarization to investigate the influence of the spin on the plane of polarization at an arbitrarily positioned, static observer in Schwarzschild spacetime. For more physically probable models, the emitter would have to be modelled more in-depth, too; in particular, if a model for the magnetic field is chosen, the polarization vector then follows from it, cf. eg. [46] and [43]. In the context of this thesis, however, the goal of modelling the polarization plane is to demonstrate the capabilities of the theory established in chapter 3; further introducing properties of the emitter would introduce more and different aspects of study, thus it is outside the scope of this thesis.

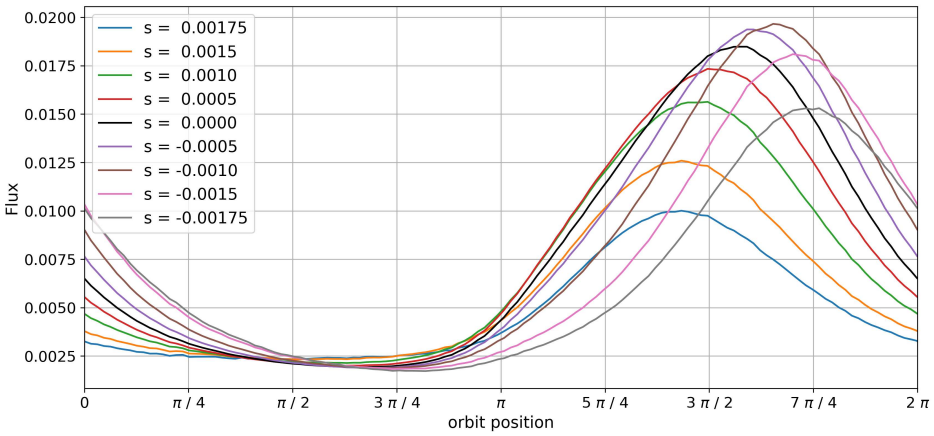

Figure 5.11: Flux at the observer's screen in arbitrary units along a spherical emitters' orbit. The different colors indicate different spin values.

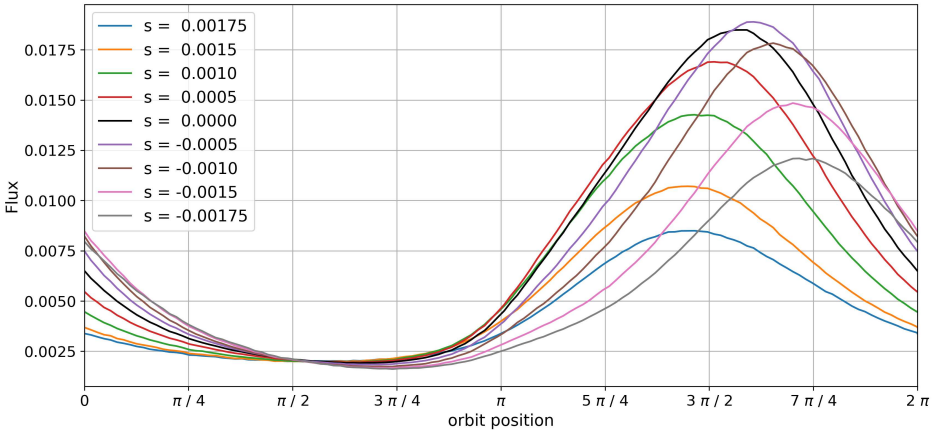

Figure 5.12: Flux at the observer's screen in arbitrary units along a spheroidal emitters' orbit. The different colors indicate different spin values.

5.3.4 Influence of the spin on the flux

In this section, the flux of a spinning emitter in orbit in the equatorial plane around a Schwarzschild object is investigated. As the redshift distribution of astrophysical objects is hardly resolvable, it is of great interest to investigate the influence of the spin on the commonly observed flux along the emitters orbit. This section follows the theoretical foundation introduced in section 3.2.4.

The observed flux of a light source is derived from integrated redshift over the observed surface area; for convenience, equation (3.85) is repeated here:

$$F_{\mathrm{obs}} = \int\int g^3 \cdot I_{\mathrm{em},\,\nu}\,\mathrm{d}\nu\,\mathrm{d}\omega = \int I_{\mathrm{em}} \cdot g^4\,\mathrm{d}\omega\,, \tag{5.50}$$

where g is the energy fraction associated with the redshift of the light ray and I_{em} is the emitted intensity profile. For simplicity, the light emitted is assumed to be monochromatic, thus the observed flux is an integral over g only. The observed flux in arbitrary units for an

observer at inclination $\vartheta_{\mathrm{obs}} = \pi/3$ is depicted in figure 5.11 for a spherical emitter and figure 5.12 for a spheroidal emitter.

Both figures show the observed flux as a function of the orbit position φ_{em}. The different colors represent different spin configurations of the emitter, evenly spaced between $s = 0.00175$ and $s = -0.00175$; the black line indicates the spinless case.
Starting from $\varphi_{\mathrm{em}} = 0$, the observed flux decreases until $\varphi \in [\pi/2,\ \pi]$, where it the increases until $\varphi \in [5\pi/4,\ 7\pi/4]$, where it then drops again. This follows the redshift distribution images shown before. The general redshift for a spinless emitter for the given orbit positions in section 5.3.2 is lowest for $\varphi_{\mathrm{em}} = \pi/2$, and highest for $\varphi_{\mathrm{em}} = 3\pi/2$, which can be seen in the figures for the observed flux as well. Additionally, the shape of the image of the emitter on the observer's screen plays a role; while the redshift of a spinless emitter at $\varphi_{\mathrm{em}} = 0$ and $\varphi_{\mathrm{em}} = \pi$ are similar, the image of the emitter is smaller if the emitter is behind the Schwarzschild object, thus the observed flux is smaller as well.
If the emitter is spinning, the position of the maximum of the flux, as well as the magnitude of the flux at its maximum, changes depending on the direction of spin. If the emitter is co-rotating, the position of maximal flux moves monotonically in spin to earlier orbit positions, while the opposite is true for a counter-rotating emitters. The change of the magnitude of maximal flux, however, is non-monotic in general. While the magnitude of flux does decrease monotonically with increasing values of s, the same cannot be said for the counter-rotating case. Here, there is a maximal magnitude lies between $s = -0.0005$ and $s = -0.0010$ for a spherical emitter and earlier between $s = 0$ and $s = -0.0005$ for a spheroidal emitter; this also marks the main difference for different emitter geometries. This effect is caused by the inclination of the observer; as the emitter is seen from above, one can see parts of the emitters surface that do not move edge-on towards the observer, thus there is no horizontal symmetry. Moreover, it is visible in general in the redshift distribution images; there, one can see (eg. in 5.6 and 5.10) that the image for a highly co-rotating emitter is more strongly dominated by red colors, indicating a higher decrease in observed frequency and thus observed flux.
Furthermore, one can see that the observed fluxes for highly co- and counter-rotating spheroidal emitters are generally lower than the observed flux for similar spherical emitters. This effect is caused by the reduced image size of the emitter, due to the increased ellipticity for high spin values for a Maclaurin spheroid with fixed semi-major axis.

In practice, the shift of the flux of known emission lines is used in astronomy to estimate the so-called radial velocity of the emitter, which is the fraction of the velocity of the emitter towards the observer. The effect of the spin on this flux is not taken into account, so the radial velocity of light sources may be over- or underestimated. However, for almost all astrophysical objects, the spin values relative to the maximal spin value is very small, so the effect is also very small too. Further study regarding this subject would be needed to estimate the error in the calculation of the radial velocity.
Other models of the type of radiation may be studied as well, with a black body profile for radiation being the most simple and astrophysically reasonable model. Nevertheless, if this theory would be used to model the emission of neutron stars, astrophysical objects with some of the highest spin-to-extension models, other radiation profiles and especially non-isotropic radiation may be important to study in detail. In either case, the amount of work regarding this would go well beyond the scope of this thesis.

Chapter 6

Spinning emitter in Kerr spacetime

6.1 Kerr spacetime

The theoretical description of light emitted by a spinning light source, introduced in the chapter 3 of this thesis, enables the discussion for an emitter in any stationary and axially symmetric spacetime for which the metric can be written as in Eq. (3.1). The previous chapter limited the discussion to a static and spherically symmetric exterior solution of the vacuum Einstein equations, the Schwarzschild solution. This chapter, however, introduces a stationary and axially symmetric background metric, the Kerr spacetime, used to describe in particular rotating black holes. The following pages are dedicated to discussing the properties of this solution, as well as the properties of light coming from a spinning emitter around a Kerr black hole.[1]

6.1.1 General physical properties

The Kerr spacetime is a exact solution to the vacuum field equations, which describes the exterior gravitational field of a uncharged, spinning black hole. The solution is stationary, axially symmetric and asymptotically flat. It was first found by Kerr [62] in 1963. It reduces to the Schwarzschild spacetime in the non-rotating case. The only physical parameters uniquely determining gravitational field of the black hole are its mass M and the dimensionless angular momentum parameter $a = J/M$, with its line element given in Boyer-Lindquist coordinates (cf. e.g. [52]) by

$$\begin{aligned} \mathrm{d}s^2 = &- \left(1 - \frac{2Mr}{\Sigma}\right)\mathrm{d}t^2 - \frac{4Mra\sin^2\vartheta}{\Sigma}\mathrm{d}t\mathrm{d}\varphi + \frac{\Sigma}{\Delta}\mathrm{d}r^2 \\ &+ \Sigma\,\mathrm{d}\vartheta^2 + \left(r^2 + a^2 + \frac{2Mra^2\sin^2\vartheta}{\Sigma}\right)\sin^2\vartheta\,\mathrm{d}\varphi^2\,, \end{aligned} \tag{6.1}$$

where

$$\Sigma = r^2 + a^2\cos^2\vartheta\,, \qquad \Delta = r^2 - 2Mr + a^2\,. \tag{6.2}$$

For a thorough discussion on the solution, see e.g. [52, 36]. The sign of a determines the direction of rotation of the black hole. As mentioned before, the metric reduces to the Schwarzschild solution in Eq. (5.1) for $a = 0$, and the Minkowski metric for $M \to 0$. In contrast to the Schwarzschild case, the Kerr metric is non-diagonal, as its line element includes a non-zero $\mathrm{d}t\mathrm{d}\varphi$-component, in line with the notion of stationarity. The solution admits two Killing fields ∂_t and ∂_φ, thus it is possible to construct a Killing tensor. Additionally, it is invariant under simultaneous transformation of $t \to -t$ and $\varphi \to -\varphi$.

[1] To minimize confusing terminology, I will refer to self-rotating light sources as *spinning*, and self-rotating sources of gravity as *rotating*.

The horizon- and singularity structure of the Kerr solution is more advanced than in the Schwarzschild case. In Boyer-Lindquist coordinates, the metric is degenerate on multiple surfaces: the event horizon and the ergosphere.
The position of the event horizon can be determined by investigating the divergent behavior of the $\mathrm{d}r\mathrm{d}r$-component of the metric; there are two event horizons at

$$r_{\mathrm{EH}}^{\pm} = M \pm \sqrt{M^2 - a^2}\,. \tag{6.3}$$

For a maximally rotating black hole at $|a| = M$, both event horizons coincide at $r = M$; for a minimally rotating black hole at $a = 0$, the outer horizon coincides with the Schwarzschild radius at $r = 2M$, while the inner horizon drops to $r = 0$. For $|a| \leq M$, the inner horizon is not directly observable, and for $|a| > M$, there is no event horizon covering the black hole anymore, leaving a naked singularity. Thus, the discussion throughout this thesis is limited to the case $|a| \leq M$.
The ergosurfaces can be located by investigating the sign of the $\mathrm{d}t\mathrm{d}t$-component of the metric, where solving the quadratic equation in $g_{tt} = 0$ leads to

$$r_{\mathrm{ES}}^{\pm} = M \pm \sqrt{M^2 - a^2 \cos^2\vartheta}\,. \tag{6.4}$$

It is notable that the metric is regular at $r_{\mathrm{ES}}^{\pm}$; the ergosurfaces do not represent a coordinate singularity in this set of coordinates. For the Schwarzschild case, the outer ergosurface coincides with the Schwarzschild radius again, and the inner ergosurface falls to $r = 0$. The outer ergosurface and outer event horizon coincide at the poles, i.e. $\vartheta = 0$ and $\vartheta = \pi$. The region between the outer ergosurface and the outer event horizon is called the ergosphere; here, massive particles must co-rotate in the direction of the sense of rotation of the black hole.

There also exists a curvature singularity, which can be checked by calculating any curvature scalar (e.g. $R^{\alpha\beta\gamma\delta}R_{\alpha\beta\gamma\delta}$); it lies at

$$r^2 + a^2 \cos^2\vartheta = 0\,. \tag{6.5}$$

The curvature singularity now takes the shape of a ring in the symmetry plane $\vartheta = \pi/2$ at $|r| = |a|$, which coincides with a point at $r = 0$ for vanishing rotation.

Lense-Thirring effect

An important gravitomagnetic effect of a non-static, stationary spacetime is the so-called Lense-Thirring effect, found by J. Lense and H. Thirring [63]. In the context of a Kerr black hole, it describes dragging of space induced by the rotation of the black hole. In particular, the movement of any observer is superimposed with a non-vanishing angular velocity in the direction of rotation of the black hole, relative to a non-rotating observer at infinity; this also called rotational frame-dragging. This also influences the notion of a stationary observer; specifically, there are no static observers in Kerr spacetimes, but rather only observers with zero angular momentum can be constructed, which will be discussed in more detail in section 6.2.1.

6.1.2 Lightlike geodesics

This subsection is dedicated to giving a quick overview over the solution of the geodesic equation for lightlike particles; recall from section 5.1.2 that they can be formulated via the Euler-Lagrange equations (cf. Eq. (5.2)) with the Lagrangian

$$\mathcal{L} = \frac{1}{2} g_{\mu\nu} \dot{x}^\mu \dot{x}^\nu = 0 \,, \tag{6.6}$$

where $g_{\mu\nu}$ are the components of the metric, and $\dot{x}^\mu$ is the tangent to the light ray; the Lagrangian itself is conserved along the orbit. Carter showed in 1968 [59, 64] that the equations of motion in Kerr spacetime are fully integrable with three constants of motion, namely E, the energy associated with the lightlike particle, L, its angular momentum, and Q, the so-called Carter constant. In the context of this thesis, the solution of the geodesic equation for lightlike particles is of particular importance, as it allows us to study the properties and path of light rays, and is consequently relevant in describing the light coming from spinning light sources around a Kerr black hole. The equation is solved numerically, finding the light ray that connects emitter and observer, following the scheme introduced in section 3.3.

The solution of the geodesic equation for lightlike geodesics in Kerr spacetime is well-established, see e.g. [52, 65]. By rescaling the affine parameter, it is possible to absorb the constant E and give the solution in the more common form in terms of $\lambda := L/E$ and $q := Q/E^2$, similar to the Schwarzschild case. The solutions take the following from:

$$\Sigma \dot{t} = -a\left(a \sin^2 \vartheta - \lambda\right) + \left(r^2 + a^2\right) \frac{T}{\Delta} \,, \tag{6.7}$$

$$\Sigma \dot{r} = \pm \sqrt{R} \,, \tag{6.8}$$

$$\Sigma \dot{\vartheta} = \pm \sqrt{\Theta_\theta} \,, \tag{6.9}$$

$$\Sigma \dot{\varphi} = -\left(a - \frac{\lambda}{\sin^2 \vartheta}\right) + a \frac{T}{\Delta} \,, \tag{6.10}$$

with

$$R = r^4 - r(q + \lambda^2 - a^2) r^2 + 2\left(q + (\lambda - a)^2\right) - a^2 q \,, \tag{6.11}$$

$$\Theta_\theta = q + a^2 \cos^2 \vartheta - \lambda^2 \cot^2 \vartheta \,, \tag{6.12}$$

$$T = r^2 + a^2 - a\lambda \,. \tag{6.13}$$

The structure of closed photon orbits in Kerr spacetime is much more difficult than the associated structure of photon regions in Schwarzschild spacetime; for a thorough discussion, see e.g. [66]. For Kerr, there is no photon sphere anymore, due to the lack of spherical symmetry in the spacetime itself. However, there exist two circular photon orbits in the equatorial plane, depending on the sense of rotation of the orbit angular momentum; in Boyer-Lindquist coordinates, they take the following form (cf. e.g. [67]):

$$r_c^\pm = 2M \left[1 + \cos\left(\frac{2}{3} \arccos \frac{\pm |a|}{M}\right)\right] . \tag{6.14}$$

Other photon orbits with constant radial distance from the source exist, but are generally more complicated in shape, and do not lie in one plane with $\vartheta = \text{const}$. On the other hand, in general, light rays that starting in the equatorial plane and end into the equatorial plane stay at $\vartheta = \pi/2$ [68].

The same phenomena for light, discussed in section 5.1.2, apply in Kerr spacetime as well. In particular, the light bending effects in the vicinity of gravitational fields, altering the path the light takes though spacetime, and the gravitational redshift, associated light moving out of or into a gravitational potential.

The following section discusses spinning light source in a Kerr background in detail.

6.2 Emission of spinning light source in equatorial plane of a Kerr black hole

In this section, the general theory on spinning light sources in the symmetry plane of stationary, axially symmetric spacetime, as established in chapter 3, is applied to the Kerr metric, introduced in the previous section. It is important to note the following sign convention for the black hole parameter a: the black hole angular momentum and the orbit angular momentum are parallel if the black hole parameter a is positive; otherwise, it is anti-parallel.

The first subsection establishes stationary observers in Kerr spacetime, which form the basis for describing physical observers at any point in spacetime, see section 3.1.1.

The second subsection covers the solution of the MPD-equations (cf. chapter 2) for spinning test particles in the symmetry plane of a Kerr black hole. In particular, this is used to establish the centre of mass reference frame, see section 3.1.2.

In the third and last subsection, the mathematical and physical properties of the relative velocity between the normalized four-momentum and the tangent of the worldline of the emitter are discussed (cf. section 3.1.3). This velocity gives rise to the centre of momentum reference frame, being the basis for the SRF reference frame.

For all following discussions and calculations, the emitter is assumed to be in the symmetry plane of the Kerr black hole, namely $\vartheta = \pi/2$; in the context of this thesis, this will be called the equatorial plane.

6.2.1 Stationary observers in Kerr spacetime

Following the description of Eqs. (3.5), a stationary observer, which has vanishing angular momentum as seen by an observer at infinity, can be written as

$$e^{\lambda}_{(a)} = \begin{pmatrix} \sqrt{\frac{A}{\Sigma\Delta}} & 0 & 0 & \frac{2ar}{\sqrt{A\Sigma\Delta}} \\ 0 & \sqrt{\frac{\Delta}{\Sigma}} & 0 & 0 \\ 0 & 0 & \sqrt{\frac{1}{\Sigma}} & 0 \\ 0 & 0 & 0 & \sqrt{\frac{\Sigma}{A\sin^2\vartheta}} \end{pmatrix}, \tag{6.15}$$

$$e^{(a)}_{\lambda} = \begin{pmatrix} \sqrt{\frac{\Sigma\Delta}{A}} & 0 & 0 & 0 \\ 0 & \sqrt{\frac{\Sigma}{\Delta}} & 0 & 0 \\ 0 & 0 & \sqrt{\Sigma} & 0 \\ -2ar\sqrt{\frac{\Sigma\Delta}{A^3}} & 0 & 0 & \sqrt{\frac{\sin^2\vartheta A}{\Sigma}} \end{pmatrix}. \tag{6.16}$$

This tetrad also forms the basis for describing a physical observer, which will be used to evaluate the observables established in section 6.3.

6.2.2 MPD equations in the symmetry plane of a Kerr object

In this section, the solution to the MPD equations in the equatorial plane of a Kerr black hole for a spinning test particle in circular motion is discussed; this spin angular momentum of the test particle is assumed to be either anti-parallel or parallel to the orbit angular momentum.

This section starts with a quick summary on the derivation of the solution, similar to section 5.2.2, which follows the approach of Tanaka et al. [37].

Recall from section 5.2.2 that the equations of motion of a spinning test particle in the orthonormal tetrad frame can be written as

$$\frac{\mathrm{d}U^{(a)}}{\mathrm{d}\tau} = w_{(b)(c)}^{\ \ \ (a)} V^{(b)} U^{(c)} - \hat{S} R^{(a)} \,, \tag{6.17}$$

$$\frac{\mathrm{d}S^{(a)}}{\mathrm{d}\tau} = w_{(b)(c)}^{\ \ \ (a)} V^{(b)} S^{(c)} - \hat{S} U^{(a)} S^{(b)} R_{(b)} \,, \tag{6.18}$$

where $U := P/\mu$ is the four-velocity associated with the four-momentum, V is the tangent of the world line of the particle, $\hat{S}$ is the magnitude of the spin and $S^{(a)}$ is the unit spin vector. For a more detailed explanation, see section 5.2.2.

For a spinning particle in the equatorial plane of a Kerr black hole, the only non-vanishing components of the tensor $w_{(a)(b)}^{\ \ \ (c)}$ are

$$w_{(0)(1)}^{\ \ \ (0)} = w_{(0)(0)}^{\ \ \ (1)} =: w_1 = -\frac{a^2 - Mr}{r^2\sqrt{\Delta}} \,, \tag{6.19}$$

$$w_{(3)(1)}^{\ \ \ (0)} = w_{(3)(0)}^{\ \ \ (1)} = w_{(1)(3)}^{\ \ \ (0)} = w_{(1)(0)}^{\ \ \ (3)} = w_{(0)(3)}^{\ \ \ (1)} = -w_{(0)(1)}^{\ \ \ (3)} =: w_2 = \frac{a}{r^2} \,, \tag{6.20}$$

$$w_{(2)(2)}^{\ \ \ (1)} = -w_{(2)(1)}^{\ \ \ (2)} = w_{(3)(3)}^{\ \ \ (1)} = -w_{(3)(1)}^{\ \ \ (3)} =: w_3 = \frac{\sqrt{\Delta}}{r^2} \,. \tag{6.21}$$

As a result of assuming the spinning test particle to be in the equatorial plane, and the orbit to be circular, all but one equation vanishes trivially, leaving only the differential equation for $U^{(1)}$, namely

$$\begin{aligned}\frac{\mathrm{d}U^1}{\mathrm{d}t} =& w_1 V^{(0)} U^{(0)} + w_2 \Big(V^{(0)} U^{(3)} + V^{(3)} U^{(0)} \Big) \\ &+ w_3 V^{(3)} U^{(3)} + \mathcal{S} \frac{M}{r^3} \Big(2V^{(0)} U^{(3)} + V^{(3)} U^{(0)} \Big) = 0 \end{aligned} \tag{6.22}$$

With the same line of reasoning described in section 5.2.2 and [37], one can obtain the non-zero components of $V^{(a)}$ and $U^{(b)}$ in terms of $\chi_v := V^{(3)}/V^{(0)}$, $\chi_u := U^{(3)}/U^{(0)}$ and $s = \mathcal{S}/M$:

$$U^{(0)} = \frac{1}{\sqrt{1-\chi_u^2}}, \qquad U^{(3)} = \frac{\chi_u}{\sqrt{1-\chi_u^2}} \,, \tag{6.23}$$

$$V^{(0)} = \frac{\sqrt{1-\chi_u^2}}{1-\chi_v\chi_u}, \qquad V^{(3)} = \frac{\chi_v\sqrt{1-\chi_u^2}}{1-\chi_v\chi_u} \,. \tag{6.24}$$

with

$$\chi_v = \frac{-(2ra + 3M^2 s + aM^3 s^2/r^2) \pm \sqrt{\chi_0}}{2\sqrt{\Delta}(r - M^3 s^2/r^2)} \,, \tag{6.25}$$

$$\chi_u = \frac{r - M^3 s^2/r^2}{r + 2M^3 s^2/r^2} \cdot \chi_v \,, \tag{6.26}$$

$$\chi_0 := 4Mr^3 + 12aM^2 rs + 13M^4 s^2 + 6aM^5 s^3/r^2 - 8M^7 s^4/r^3 + 9a^2 M^6 s^4/r^4 \,. \tag{6.27}$$

Again, we can identify the quantity χ_v as the orbital velocity v of the spinning test particle, depending only on the distance r to the centre of the black hole, the spin of the particle s and the black hole rotation parameter a, as well as the mass M of the central object. Thus, the Lorentz transformation from the stationary observer into the centre of mass reference frame and back is fully determined, see Eq. (3.10) ff.

6.2.3 Relative velocity between four-velocity and normalized four-momentum in Kerr background

In this section, the relative velocity for a spinning light source in the symmetry plane of a Kerr black hole is calculated in detail. As discussed in section 3.1.3 in general, and in section 5.2.3 for Schwarzschild specifically, the relative velocity is a consequence of the fact that the tangent of the world line and the normalized four-momentum are not parallel for spinning test particles. Again, the relative velocity $\mathcal{V}$ can be expressed in terms of the four-velocity V^ν (see Eq. (3.17)), i.e.

$$\mathcal{V}^2 = 1 + V_\nu \, V^\nu \,. \tag{6.28}$$

In particular, the four-velocity of a spinning light source in the equatorial plane of a Kerr black hole is given by Eq. (6.24), thus the relative velocity can be rewritten in terms of χ_u and χ_v as

$$\mathcal{V}^2 = 1 - \frac{(1 - \chi_u^2)(1 - \chi_v^2)}{(1 - \chi_u \chi_v)^2} \,. \tag{6.29}$$

Recall that for vanishing spin values, the quantities χ_u and χ_v coincide, and the relative velocity vanishes as a consequence, which is in line with the physical considerations, see e.g. sections 2.2 and 3.1.3. For small spin values, the relative velocity can be approximated up to leading order in s by

$$\begin{aligned} \mathcal{V}^2\Big|_{s=0} \approx \Bigg[& \frac{108M^3(a \pm \sqrt{Mr})^4}{r^3 \left(4\Delta - (a \pm \sqrt{Mr})^2\right)^2} - \frac{4aM + 8aM^3 r}{r^4} \\ & \pm \frac{31M^4\sqrt{r^2 - 2Mr} - 9a^2 M\sqrt{r^2 - 2Mr} + 24M^4 r}{4r^4\sqrt{M(r - 2M)}} \Bigg] \cdot s^2 + \mathcal{O}(s^3) \,. \end{aligned} \tag{6.30}$$

The full derivation is given in appendix A.

The subsequent section handles the description of the different observables, specifically for a spinning source of radiation in the equatorial plane around a Kerr black hole.

Table 6.1: Depiction of the radial distance values r_{em} and associated orbital velocities v for non-spinning test particles, depending on the Kerr parameter a considered throughout this thesis. The values of r_{em} are chosen such that the emitter takes the same time for one orbit for every value of a.

Black hole spin a	Radial distance of orbit r_{em}	Orbital velocity v
$-0.9M$	$9.321M$	0.475693
$0M$	$8M$	0.408248
$0.9M$	$6.067M$	0.309639

6.3 Observables in Kerr spacetime

This section is dedicated to discussing the observables of spinning light sources around Kerr black holes, formerly introduced in section 3.2. In particular, the influence of the spin on these observables is studied in detail.

For this reason, a configuration of emitter and observer properties is required, including their positions in spacetime, as well as the geometrical properties of the emitter. Again, as long as the values chosen abide the established theory, there are no constraints on the choice of parameters; nonetheless, it is possible to reason some preferences for studying the effects of spin and gravity on the observables.
As a natural scale of distances, all lengths are given in units of the mass of the central object, M. In addition to length scales, the spin of the emitter is given in units of the central mass M, namely

$$s = \frac{\mathcal{S}}{M} \,. \tag{6.31}$$

The emitter is orbiting the Kerr black hole in the symmetry plane $\vartheta_{\mathrm{em}} = \pi/2$. The distance to the central object is chosen such that the duration of orbit on the observer's screen coincides with the Schwarzschild case; the values of distance are depicted in table 6.1. Although at varying distances, the emitter is close enough to the black hole to study the effect of gravity on the path of the light, and at the same time far enough away from the centre of gravity to not interfere with any marginally stable circular orbit.
The location of the observer in spacetime remains at $r_{\mathrm{obs}} = 35M$ and $\vartheta_{\mathrm{obs}} = \pi/3$, as in the Schwarzschild case. In particular, the distance is chosen to be finite, but moderately far away from the black hole, and the elevation of the observer enables the studying of the effect of inclination on the observations. Furthermore, it allows us to limit the discussion of multiple images to only using the direct images.
The geometrical extension is again set to be $\rho = 0.005M$ for a spherical emitter and $A = 0.005M$ if the emitter is described by a Maclaurin spheroid. Thus, the emitter is small enough to abide the test particle approximation for the MPD equations and its size limit, cf. Eq. (2.13), but large enough to uphold the numerical constraints discussed in section 3.3. Again, the Möller limit for a spinning object of this geometrical extension limits the spin to $|s_{\mathrm{max}}| = 0.002$.

Screen coordinates for a static observer in Kerr spacetime

In order to simulate the recording of the observables at the observer, the notion of a celestial sphere and observer's screen has to be established in Kerr spacetime specifically, following the description in section 3.2.1.

Recall that the celestial sphere is described by the azimuth coordinate $\Phi \in [0,\ 2\pi)$ and the polar coordinate $\Theta \in [-\pi/2,\ \pi/2]$, see Eqs. (3.58) ff. These coordinates are determined

by the four-velocity of the lightlike geodesic, see Eqs. (6.7) to (6.10), and can be written as

$$\cos\Theta = -\frac{\dot{r}}{\zeta}\sqrt{\frac{A}{\Sigma\Delta}}\,, \qquad \sin\Theta = \sqrt{1-\frac{\dot{r}^2}{\zeta^2}}\,, \tag{6.32}$$

$$\cos\Phi = \frac{\dot{\vartheta}}{\sqrt{\zeta^2-\dot{r}^2}}\sqrt{\frac{\Sigma}{\Delta}}\,, \qquad \sin\Phi = -\frac{\sin\vartheta\dot{\varphi}}{\sqrt{\zeta^2-\dot{r}^2}}\sqrt{\frac{A}{\Sigma}}\,, \tag{6.33}$$

where

$$\zeta = g(\dot{\lambda}, \mathbf{e}_{(0)}) = \frac{a\lambda - a^2\sin^2\vartheta - \Sigma}{\sqrt{\Sigma\Delta}}\,. \tag{6.34}$$

The screen coordinates α and β are then defined by stereographic projection; recall from Eq. (3.60):

$$\alpha := -2\frac{(1-\cos\Theta)}{\sin\Theta}\sin\Phi\,, \tag{6.35}$$

$$\beta := 2\frac{(1-\cos\Theta)}{\sin\Theta}\cos\Phi\,. \tag{6.36}$$

Structure of the following section

This section is structured similarly to the section for a Schwarzschild central object, in particular:

First, the influence of the emitter spin on the orbital and relative velocity for different rotating black hole rotations is studied.
Afterwards, the influence of the emitter spin on the redshift distribution, similar to the Schwarzschild case, is studied. Here, the influence of different emitter and black hole spins are objects of study, and the different types of emitter geometries are distinguished.
Then, the change of polarization angle, depending on the spin of the emitter, is discussed in detail. In this context, the notion of a polarization vector and its parallel transport along the lightlike geodesic to the observer is detailed.
Lastly, the observed flux and the dependence of the spin on it is studied; here, the difference of emitter geometry on the flux is examined, too.

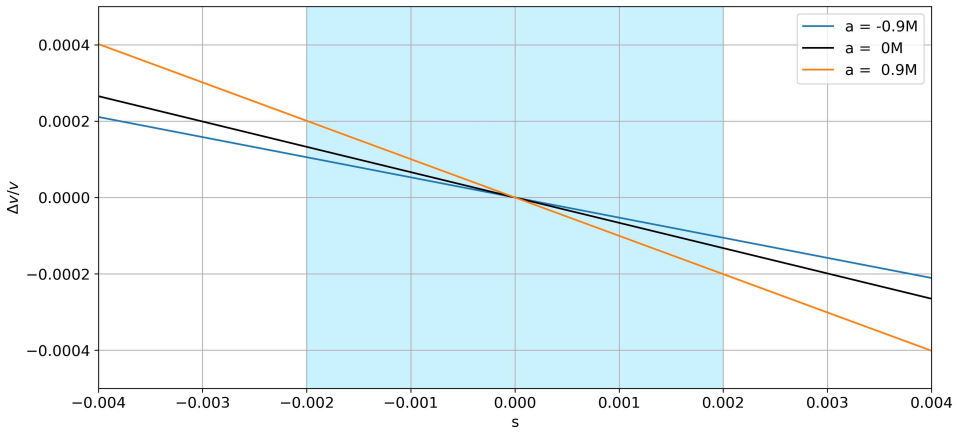

Figure 6.1: Change in orbital velocity $\triangle v/v$ relative to the spinless case, dependent on the spin of the emitter. Each color represents the magnitude and direction of the black hole rotation. The blue shaded area indicates the range of spin allowed for an emitter with a scale of geometry of $0.005M$.

6.3.1 Influence of the spin on the velocities

In this section, the influence of the spin on the orbital velocity and relative velocity for different black hole rotations is studied.

In figure 6.1, the relative change in orbital velocity of the emitter depending on the spin is depicted; the values of the orbital velocity for spinless test particles is given in table 6.1. The different colors represent different values of the black hole angular momentum parameter a; the black line indicates the Schwarzschild limit at $a = 0$, see section 5.3.1. For black holes co-rotating with the direction of orbit rotation, the change in orbital velocity reduces, relative to the Schwarzschild case, while the opposite is true for a black hole counter-rotating with the orbit. However, the effect of the spin on the change of orbital velocity is still rather small, so the orbital velocity can be considered nearly constant for different values of spin, regarding the discussions on the influence of spin on the light emitted. In all numerical procedures, the exact values for the orbital velocity is inserted.

Figure 6.2 shows the relative velocity $\mathcal{V}$ depending on the spin and distance for different black hole rotations. The top panel shows shows the relative velocity depending on the distance of the source of gravity for two spin values for each black hole rotation each. It is clear to see that the relative velocity diverges at different radial distances, depending on the black hole rotation. This occurs when the orbital velocity becomes lightlike for these high values of spin. The spin values are chosen to be unrealistically high at $s = \pm 1$ in order to show that the relative velocity drops off strongly at the position of the emitter, indicated by the dashed lines for every value of a.

In the bottom panel, this can be seen even more clearly. Here, the dependence of the relative velocity on the spin of the light source is shown on a logarithmic scale. Again, the different colors depict the relative velocity evaluated at different values of a at their respective orbit positions. The relative velocity does differ strongly between different angular momentum parameters; however, even at the maximal spin values of $|s| = s_{\max}$, the relative velocity does not exceed magnitudes $> \mathcal{O}(10^{-13})$, and is negligible compared to the orbital velocity. Thus, the effect of the relative velocity on the observables are small, but the exact values for $\mathcal{V}$ are inserted in all numerical computations exactly.

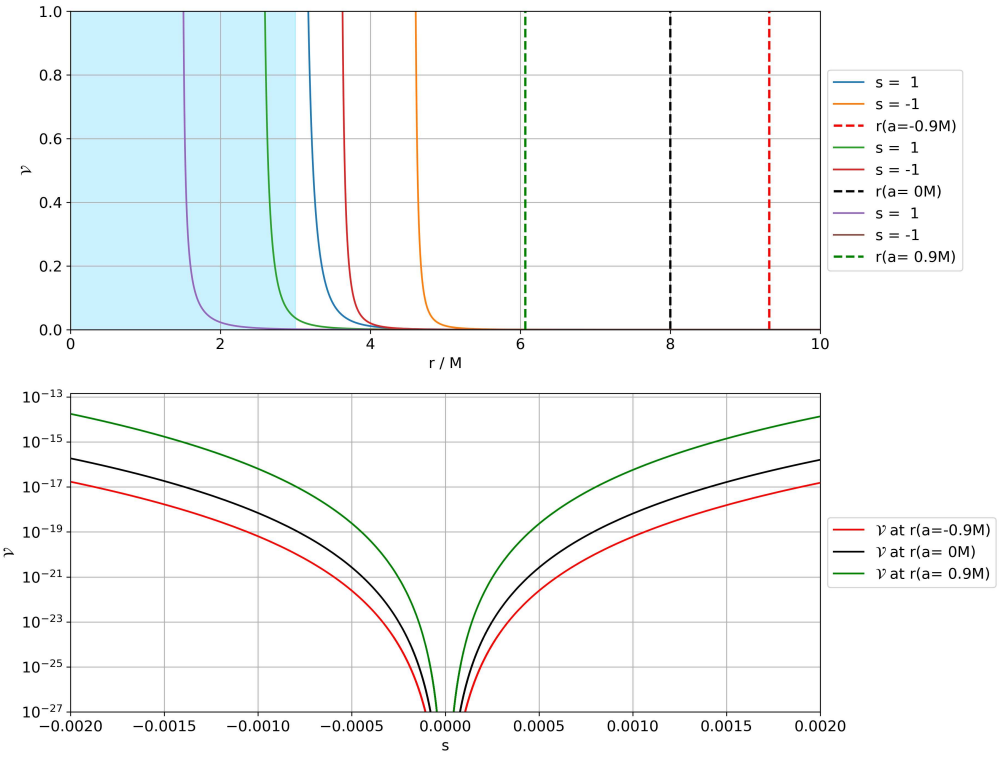

Figure 6.2: Graphical depiction of the relative velocity $\mathcal{V}$.
Top: dependence of the relative velocity on the distance to the source of gravity. The different colors indicate the relative velocity for very high values of spin $|s| = 1$. The black dashed line indicates the position of the emitter, see table 6.1.
Bottom: relative velocity at the orbital position of the emitter, depending on the spin parameter s. The different colors indicate different magnitude and direction of black hole rotation.

6.3.2 Influence of the spin on the redshift

Redshift distribution for a spherical emitter at $a = -0.9M$

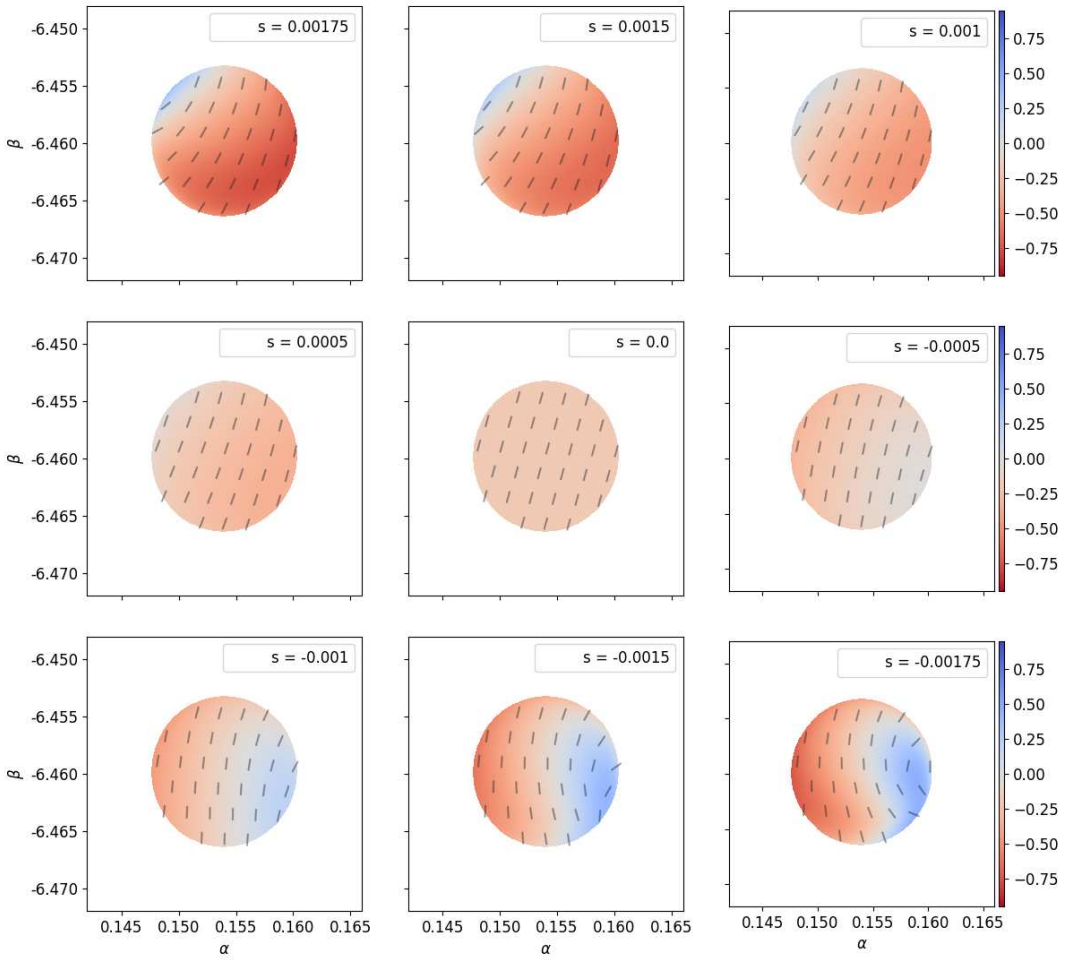

Figure 6.3: Redshift distribution of a spherical emitter for different spin values for an emitter in front of the Kerr black hole, i.e. $\varphi_{\mathrm{em}} = \varphi_{\mathrm{obs}} = 0$, on the observer's screen, with Kerr spin $a = -0.9M$. Negative emitter spin values correspond to counter-rotating emitters, while emitter positive spin values correspond to co-rotating emitters. Colors indicate the magnitude of redshift, while the grey bars indicate the shift of the polarization plane, see section 6.3.3.

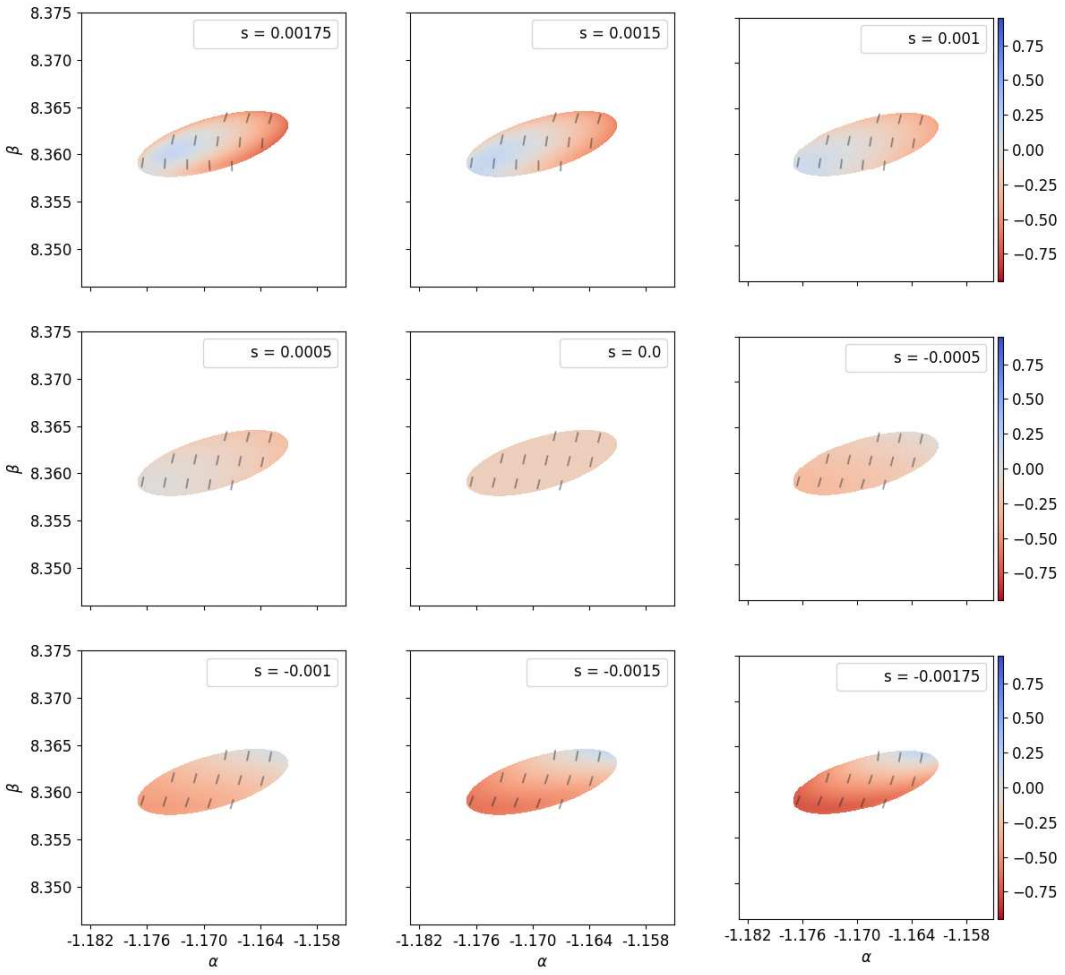

Figure 6.4: Redshift distribution of a spherical emitter for different spin values for an emitter behind the Kerr black hole, i.e. $\varphi_{\rm em} = \pi$, on the observer's screen, with Kerr spin $a = -0.9M$. Negative emitter spin values correspond to counter-rotating emitters, while emitter positive spin values correspond to co-rotating emitters. Colors indicate the magnitude of redshift, while the grey bars indicate the shift of the polarization plane, see section 6.3.3.

Redshift distribution for a spheroidal emitter at $a = -0.9M$

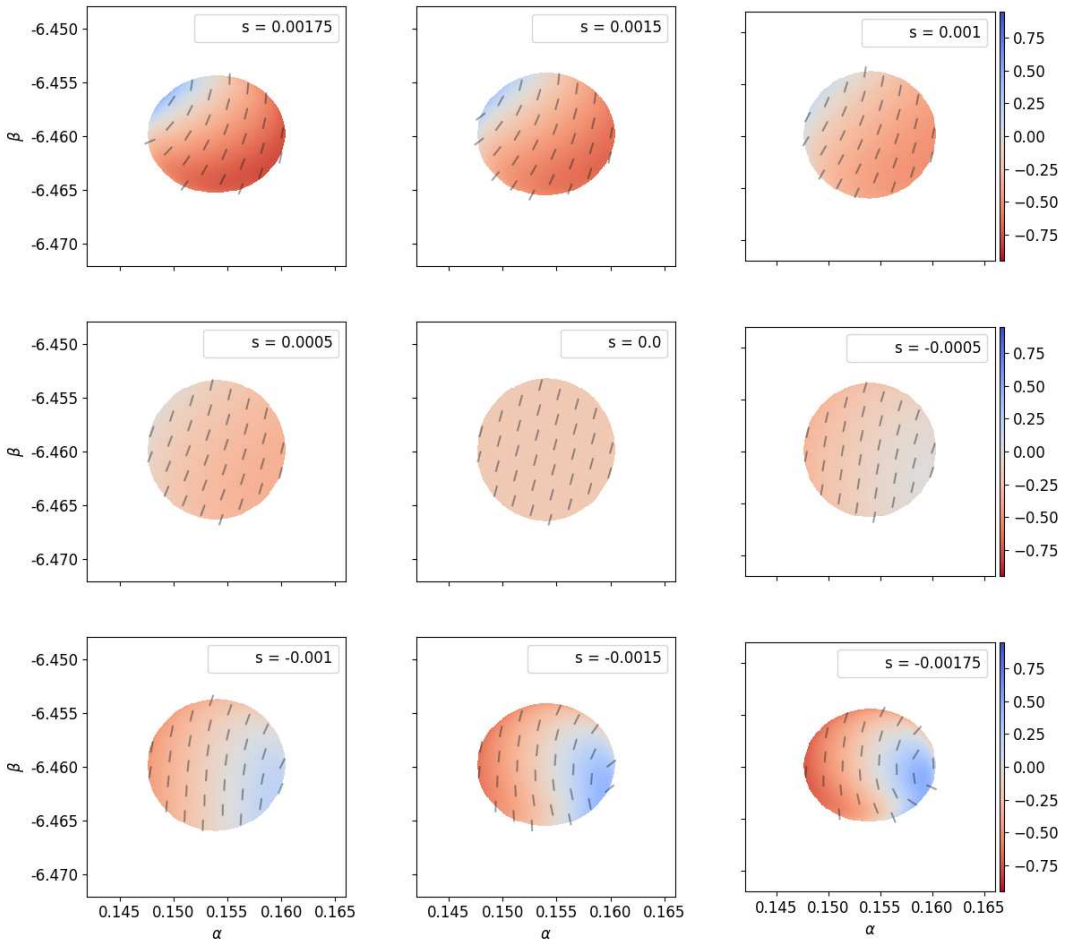

Figure 6.5: Redshift distribution of a spheroidal emitter for different spin values for an emitter in front of the Kerr black hole, i.e. $\varphi_{\rm em} = \varphi_{\rm obs} = 0$, on the observer's screen, with Kerr spin $a = -0.9M$. Negative emitter spin values correspond to counter-rotating emitters, while emitter positive spin values correspond to co-rotating emitters. Colors indicate the magnitude of redshift, while the grey bars indicate the shift of the polarization plane, see section 6.3.3.

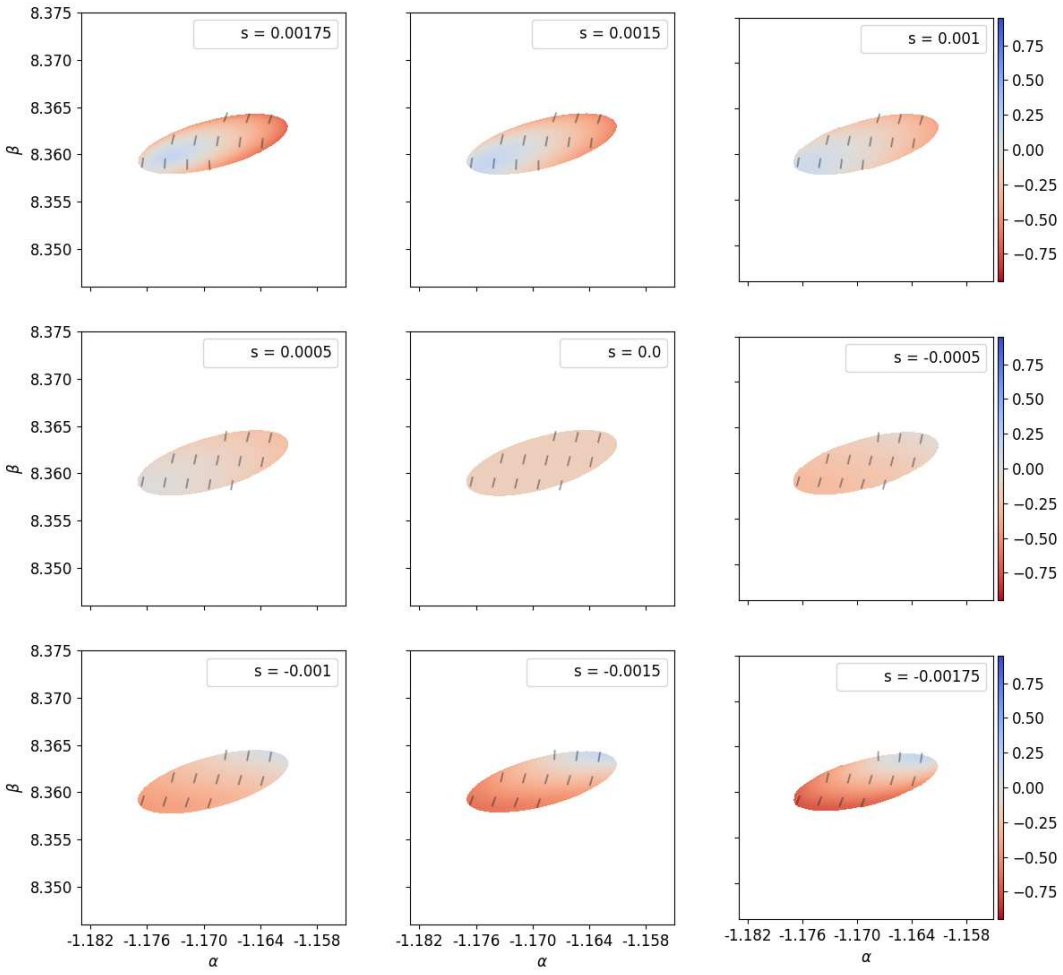

Figure 6.6: Redshift distribution of a spheroidal emitter for different spin values for an emitter behind the Kerr black hole, i.e. $\varphi_{\rm em} = \pi$, on the observer's screen, with Kerr spin $a = -0.9M$. Negative emitter spin values correspond to counter-rotating emitters, while emitter positive spin values correspond to co-rotating emitters. Colors indicate the magnitude of redshift, while the grey bars indicate the shift of the polarization plane, see section 6.3.3.

Redshift distribution for a spherical emitter at $a = 0.9M$

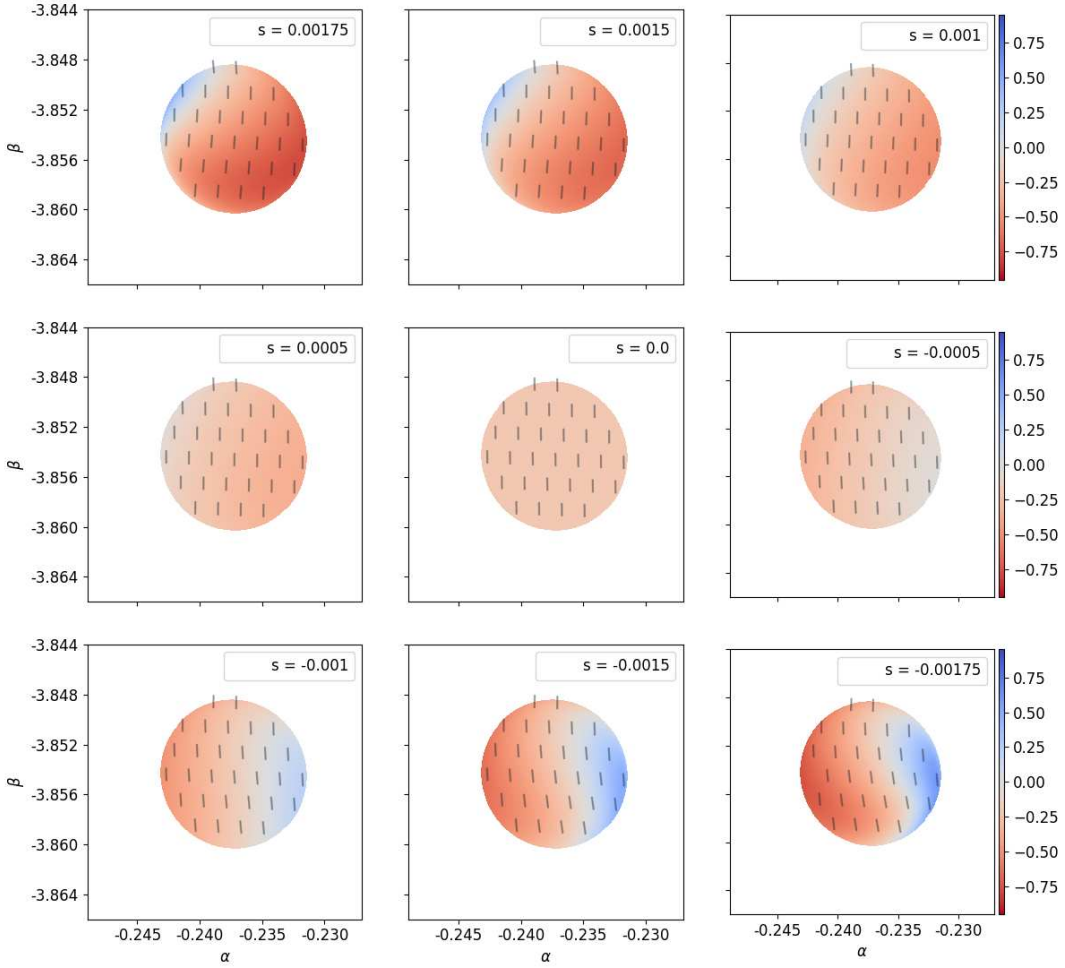

Figure 6.7: Redshift distribution of a spherical emitter for different spin values for an emitter in front of the Kerr black hole, i.e. $\varphi_{\rm em} = \varphi_{\rm obs} = 0$, on the observer's screen, with Kerr spin $a = 0.9M$. Negative emitter spin values correspond to counter-rotating emitters, while emitter positive spin values correspond to co-rotating emitters. Colors indicate the magnitude of redshift, while the grey bars indicate the shift of the polarization plane, see section 6.3.3.

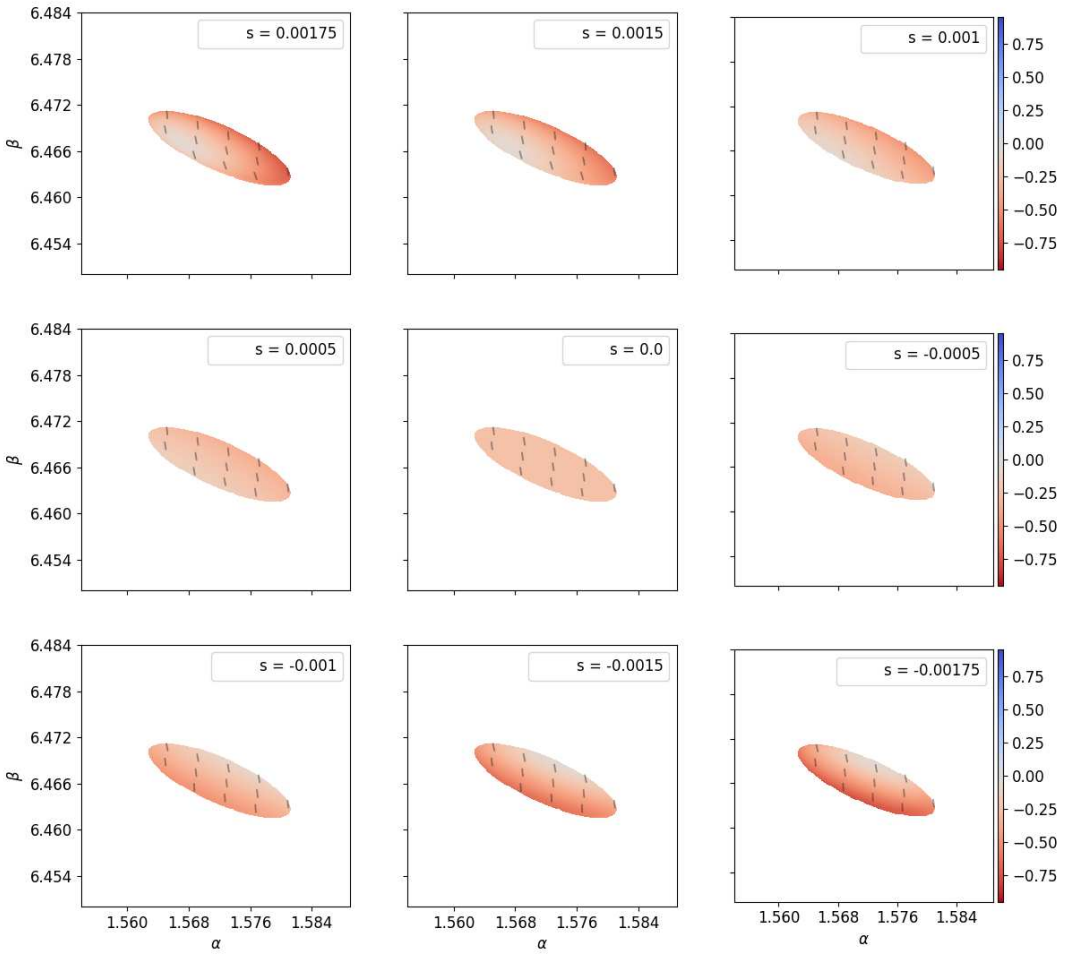

Figure 6.8: Redshift distribution of a spherical emitter for different spin values for an emitter behind the Kerr black hole, i.e. $\varphi_{\rm em} = \pi$, on the observer's screen, with Kerr spin $a = 0.9M$. Negative emitter spin values correspond to counter-rotating emitters, while emitter positive spin values correspond to co-rotating emitters. Colors indicate the magnitude of redshift, while the grey bars indicate the shift of the polarization plane, see section 6.3.3.

Redshift distribution for a spheroidal emitter at $a = 0.9M$

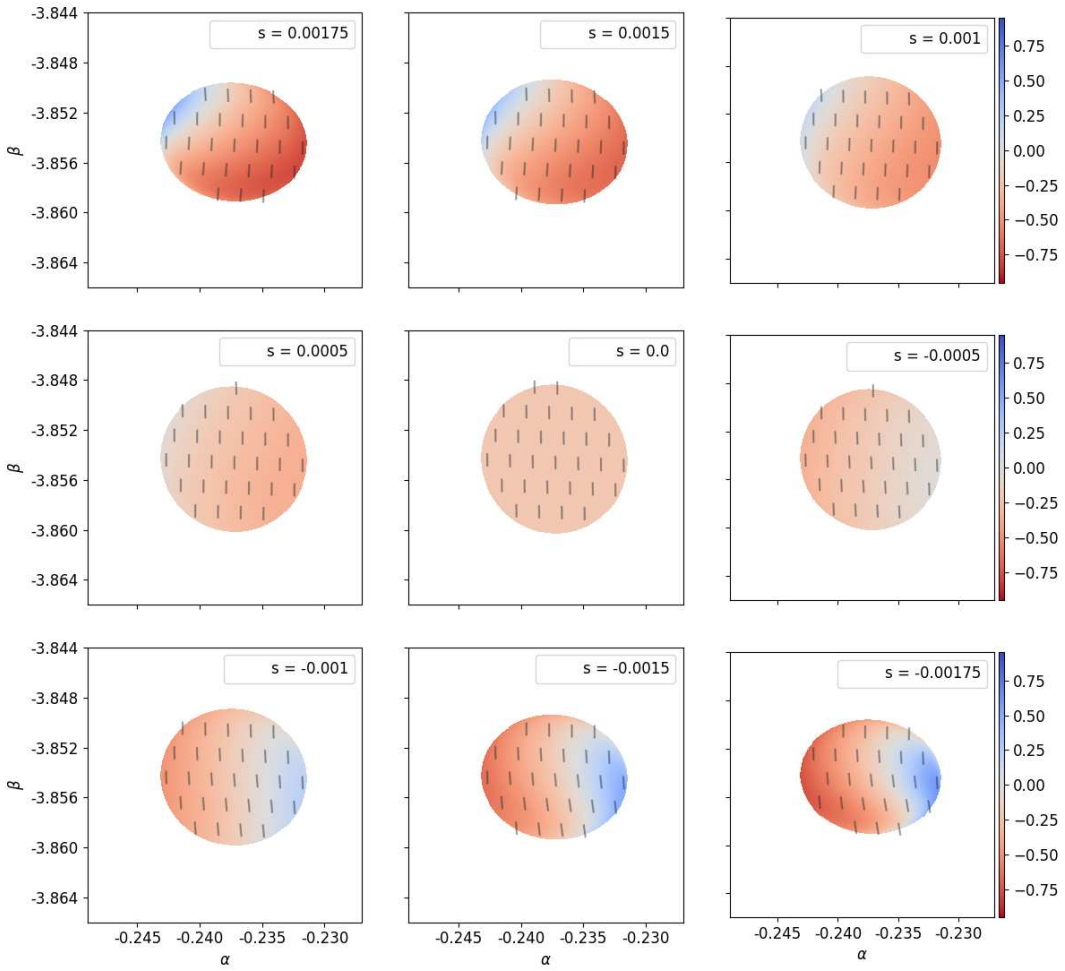

Figure 6.9: Redshift distribution of a spheroidal emitter for different spin values for an emitter in front of the Kerr black hole, i.e. $\varphi_{\rm em} = \varphi_{\rm obs} = 0$, on the observer's screen, with Kerr spin $a = 0.9M$. Negative emitter spin values correspond to counter-rotating emitters, while emitter positive spin values correspond to co-rotating emitters. Colors indicate the magnitude of redshift, while the grey bars indicate the shift of the polarization plane, see section 6.3.3.

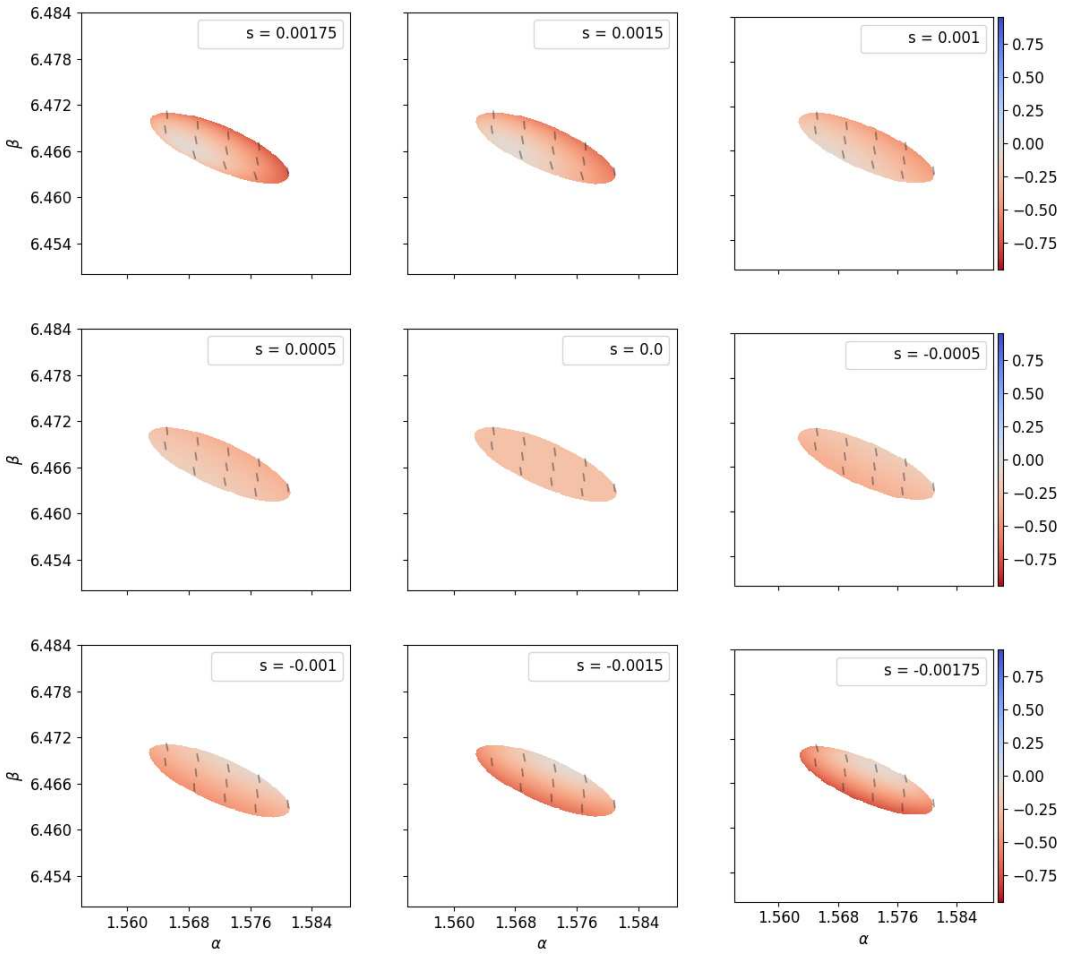

Figure 6.10: Redshift distribution of a spheroidal emitter for different spin values for an emitter behind the Kerr black hole, i.e. $\varphi_{\rm em} = \pi$, on the observer's screen, with Kerr spin $a = 0.9M$. Negative emitter spin values correspond to counter-rotating emitters, while emitter positive spin values correspond to co-rotating emitters. Colors indicate the magnitude of redshift, while the grey bars indicate the shift of the polarization plane, see section 6.3.3.

The information on the redshift of the emitted light, as well as the shape of the object and its placement on the observer's screen can be seen in figures 6.3 to 6.10. In particular, figures 6.3 to 6.6 depict the redshift distribution of an emitter in the equatorial plane of a Kerr black hole that is strongly counter-rotating relative to the sense of orbit direction, with $a = -0.9M$. Similarly, figures 6.7 to 6.10 present the redshift distribution for a Kerr black hole that is strongly co-rotating, relative to the sense of orbit direction, with $a = 0.9M$.
For every Kerr rotation parameter, there are 2 figures for each of the considered emitter geometries; the first two images represent the redshift distribution of a spherical light source, the latter two represent the redshift distribution of a spheroidal light source. Each emitter geometry is depicted for two orbit positions, $\varphi_{\rm em} = 0$ and $\varphi_{\rm em} = \pi$. In this thesis, the observer is at $\varphi_{\rm obs} = 0$, thus the case $\varphi_{\rm em} = 0$ is referred to as the emitter being in front of the black hole, while the the case $\varphi_{\rm em} = \pi$ is referred to as the emitter being behind the black hole.

Similar to the figures in section 5.3.2, every figure is composed of 9 panels, each panel representing the emitter spinning at different rates. The values of spin range from $s = -0.00175$ to $s = 0.00175$, below the maximal spin value of $|s_{\max}| = 0.002$, dictated by the Möller limit in Eq. (4.5) and (4.19). Positive values of s correspond to emitters co-rotating with the direction of orbit rotation, while negative values of s correspond to emitters counter-rotating with the direction of orbit rotation instead.
Each panel consists of a colored shape, which is the shape of the emitter on the observer's screen. The emitter is depicted on the observer's screen in terms of the stereographic projection of the celestial sphere of the observer, namely $(\alpha,\ \beta)$; see the start of section 6.3. To give a sense of direction, the emitter moves in positive α-direction, i.e. to the right, if the emitter is in front of the black hole, and in negative α-direction, i.e. to the left, if the emitter is behind the black hole. The color of the image represents the redshift of the observed light; red colors indicate a decrease in frequency, relative to the emitted frequency, and blue colors indicate an increase in frequency. Additionally, each panel depicts the plane of polarization, distributed over the image of the emitter; these are represented as the grey bars on top of the redshift distribution. The polarization plane and the influence of the spin on it is discussed in detail in the following section 6.3.3.

First, the spinless case is discussed, in particular for a spherical emitter. This corresponds to the middle panels of figures 6.3 and 6.4 for a black hole that is counter-rotating with the direction of orbit, and 6.7 and 6.8, if the black hole is co-rotating. Specifically, the redshift distribution for different black hole rotations is discussed, and compared to the case of vanishing black hole rotation, i.e. Schwarzschild, which can be seen in the centre panels of figures 5.3 and 5.5.
Similarly to the Schwarzschild case, if the emitter is in front of the black hole, its shape is conserved, appearing spherical on the observer's screen. The influence of the black hole rotation becomes most apparent when comparing the position of the observer on the screen itself. For the Schwarzschild case, i.e. $a = 0$, the emitter is seen at negative values of β, due to the inclination of the observer at $\vartheta_{\text{obs}} = \pi/3$, but centered around $\alpha = 0$ in the vertical middle of the screen. This symmetry is broken if the black hole is rotating; for a black hole that is co-rotating with the direction of orbit rotation, i.e. $a = 0.9M$, the image of the emitter is shifted to the left on the observer's screen, and to the right if the black hole is counter-rotating relative to the orbit rotation, i.e. $a = -0.9M$. This is due to the frame-dragging effect of the rotating black hole: if the black hole is strongly co-rotating with the orbit rotation, the light is emitted from the light source against the direction of orbit rotation, to compensate the effect of the black hole on spacetime. The light thus forms an arc, such that it hits the observer from the left. Similarly, if the black hole is strongly counter-rotating with the orbit direction, the light is emitted further into the direction of orbit rotation, to counteract the effect that the black hole drags the path of the light against the sense of orbit direction. Thus, the light forms an arc such that it hits the observer from the right, resulting in an image of the emitter that is shifted in positive α-direction.

The redshift distribution is nearly uniform and negative, explainable by the notion of gravitational redshift, similar to the Schwarzschild case. For $a = -0.9M$, the redshift is generally slightly increased compared to a non-rotating black hole, and slightly decreased for $a = 0.9M$. This effect is caused by the different distances of orbit of the emitter to the source of gravity, thus increasing or decreasing the distance of the emitter to the observer; the rotation of the black hole does not significantly impact the redshift by itself in this context.
The most extreme case of a non-spherical image of the emitter is depicted for the case that the emitter is behind the black hole, cf. figures 6.4 and 6.8. For the case of a non-rotating black hole, the image of the emitter is strongly flattened vertically, appearing on the screen at positive values of β, and again centred around $\alpha = 0$. The fact that the emitter is visible

at $\beta > 0$ is due to the observer's inclination, as the direction $\beta = \alpha = 0$ corresponds to the direction towards $r = 0$. For a rotating black hole, the position of the emitter on the observer's screen, as well as its appearance, changes drastically. For a strongly co-rotating black hole, relative to the direction of orbit rotation, the image of the emitter is shifted far to the right, i.e. positive values of α. Furthermore, the previously nearly elliptical shape of the emitter appears rotated to the right. On the contrary, the emitter is shifted far to the left, i.e. to negative values of α, with its elliptical shape appearing rotated to the left, for a strongly counter-rotating black hole, relative to the direction of orbit rotation. This effect is caused by a combination of the light bending due to the gravitational pull of the black hole and the frame-dragging caused by the black hole rotation. The light bending effects are strongest if the emitter is behind the black hole; in particular, the light is bent so strongly that parts of the back side of the emitter are visible. Tha line of reasoning explains the non-spherical shape of the object. The shift of the image is caused by the frame-dragging, as the path is bent into or against the direction of orbit rotation, counteracting the effect of the black hole rotation. The apparent rotation of the image is caused by a combination of both; for $a = 0.9M$, the emitted light coming from the right side of the light source, compared to its left side, is increasingly shifted to the right by the frame-dragging effect, but the light has to be emitted closer the equatorial plane as a result, in order to reach the observer. Similar reasoning explains the equivalent effect for $a = -0.9M$.

Next, the influence of the spin on the redshift is discussed, again in particular for a spherical emitter.
In the following, most of the discussion applies for both orbit positions, thus the case that the emitter is in front of the black hole is studied exemplary, again seen for $a = -0.9M$ in figure 6.3 and for $a = 0.9M$ in figure 6.7. It is apparent that the redshift distribution of a spinning emitter is not uniform anymore, and the effect is stronger for increasing magnitude of spin. This is in line with the discussion for a spinning emitter in Schwarzschild spacetime. The most important observations are repeated here briefly: the frequency of the light emitted by surface elements moving towards the observer is increased due to the Doppler effect, and the frequency of light emitted by surface elements moving away from the observer is decreased. This is best seen for highly spinning emitters with $|s| = 0.00175$. The non-symmetrical appearance of the redshift distribution is caused again by the inclination of the observer above the equatorial plane.

The influence of the black hole rotation on this behaviour is small. The general behaviour of the redshift distribution for different emitter spins is similar for both black hole rotations considered. There are slight differences in the redshift, which are caused by the frame-dragging of the light, as the areas of positive redshift for a highly counter-rotating emitter for $a = -0.9M$ are bigger than the areas of positive redshift are for a highly counter-rotating emitter for $a = 0.9M$. Similar arguments can be made for highly co-rotating emitters, where the areas of positive redshift are bigger for $a = 0.9M$, compared to the same areas for $a = -0.9M$; however, this effect is even smaller.

The influence of the geometrical shape of the emitter is shown in figures 6.5 and 6.6 for a black hole that is counter-rotating with the direction of orbit rotation, and 6.9 and 6.10, if the black hole is co-rotating. For strongly spinning emitters, independent on the direction of spin, the shape of the emitter changes even for an emitter in front of the black hole. This matches the increasingly non-spherical, spheroidal form of the emitter in spacetime and the theoretical considerations made in section 4.2. Specifically, the semi-minor axis c for the highest spin case of $|s| = 0.00175$, for a mass smaller than the critical mass ratio (cf Eq. (4.21)), is $c \approx 0.00327M$; recall that the semi-major axis is fixed at $a = 0.005M$. The extent of this eccentricity is not fully reflected in the figures above, as the emitter is observed from above, thus the shape is less elliptical than would be the case if the emitter was observed edge-on;

this behaviour is observed in the Schwarzschild case as well. The influence of the spin on the redshift distribution follows the same line of reasoning as described above, and the spin of the black hole does not influence the distribution in other ways than those described in the previous paragraph.

6.3.3 Influence of the spin on the polarization

In this subsection, the polarization of the light emitted from spinning light source orbiting a Kerr black hole is discussed in detail, following the theoretical description outlined in section 3.2.2.

First, recall that the light is assumed to linearly polarized parallel to $e^{\{2\}}$, relative to the rest frame of the surface. In this frame, the polarization vector is given by Eq. (3.64), repeated here for convenience:

$$f^{\{d\}} = N \cdot \left(-1\,, \quad 0\,, \quad \frac{p_{\{0\}}}{p_{\{2\}}}\,, \quad 0 \right). \tag{6.37}$$

Note that $p_{\{d\}}$ is the four-momentum of the light ray, established from Eq. (6.7) to (6.10), transformed into the SRF reference frame by transformation rules established in section 3.1.4, and N is the normalization constant fixed by the velocities, seen in Eq. (3.66). The constants of motion, used to fix the four-momentum, are computed by the scheme introduced in chapter 3, thus the polarization vector is uniquely determined for every chosen spin.

The goal of this section is to describe the polarization angle at the position of the observer for a spinning source of radiation orbiting a Kerr black hole. In order to achieve that, the polarization vector has to be transformed into spacetime coordinates and parallel transported to the observer position. There are four non-trivial equations for all spacetime components of the polarization vector, parallel transported along the lightlike geodesic, and are given by

$$\begin{aligned}
\kappa_1 &= r\left(k^t f^r - k^r f^t\right) + ra\sin^2\vartheta\left(k^r f^\varphi - k^\varphi f^r\right) \\
&\quad - a\cos\vartheta\sin\vartheta\left[(r^2+a^2)\left(k^\varphi f^\vartheta - k^\vartheta f^\varphi\right) - a\left(k^t f^\vartheta - k^\vartheta f^t\right)\right], && (6.38)\\
\kappa_2 &= -a\cos\vartheta\left(k^t f^r - k^r f^t\right) - a^2\sin^2\vartheta\cos\vartheta\left(k^r f^\varphi - k^\varphi f^r\right) \\
&\quad - r\sin\vartheta\left[(r^2+a^2)\left(k^\varphi f^\vartheta - k^\vartheta f^\varphi\right) - a\left(k^t f^\vartheta - k^\vartheta f^t\right)\right], && (6.39)\\
1 &= -g_{tt}\left(f^t\right)^2 + g_{t\varphi} f^t f^\varphi + g_{rr}\left(f^r\right)^2 + g_{\vartheta\vartheta}\left(f^\vartheta\right)^2 + g_{\varphi\varphi}\left(f^\varphi\right)^2, && (6.40)\\
0 &= -g_{tt} f^t k^t + g_{t\varphi}\left(f^t k^\varphi + f^\varphi k^t\right) + g_{rr} f^r k^r + g_{\vartheta\vartheta} f^\vartheta k^\vartheta + g_{\varphi\varphi} f^\varphi k^\varphi, && (6.41)
\end{aligned}$$

where $\kappa_{1,\,2}$ are the real and imaginary parts of the Penrose-Walker constant (cf. [44, 45, 46]), and $g_{\mu\nu}$ are the components of the metric tensor for the Kerr solution, see Eq. (6.1). The value of the Penrose-Walker constant can be fixed at the point of emission, only necessary to compute once, and the tangent of the world line of the photon and the polarization vector at emission in spacetime coordinates are known for a given light ray, in the context of this thesis.

This set of equations can be solved analytically, thus it is possible to write down the exact formula for the polarization vector at any point in spacetime. It can be expressed as

$$f^t = C_{38} \pm \sqrt{C_{39}}\,, \tag{6.42}$$

$$f^r = C_{40} \pm \sqrt{C_{41}}\,, \tag{6.43}$$

$$f^\vartheta = C_{36} \pm \sqrt{C_{37}}\,, \tag{6.44}$$

$$f^\varphi = C_{42} \pm \sqrt{C_{43}}\,. \tag{6.45}$$

The full derivation, along with the definition of all terms mentioned here, can be seen in appendix A.3.2. Afterwards, as the polarization vector is then computed at the position of the observer, the polarization angle on the observer's screen can be calculated, relative to the positive β-axis, introduced in section 3.2.

The information on the plane of polarization and influence of the spin on it can be seen in figures 6.3 to 6.10, where the polarization plane is depicted as grey bars on top of the redshift distribution, which is discussed in the previous subsection. The polarization plane for a spherical emitter in the equatorial plane of a Kerr black hole is depicted in figures 6.3 to 6.8, and for a spheroidal emitter in figures 6.5 to 6.10. It is important to note that the relative strength of the polarization is not depicted in these figures.

In general, the qualitative behaviour of the plane of polarization for a spinning emitter in the equatorial plane of a Kerr black hole is similar to the Schwarzschild case, i.e. for vanishing black hole rotation. The plane of polarization of an emitter in front of the black hole is uniformly distributed on the observer's screen for a spinnless emitter, see e.g. figure 6.3. If it is in front of the black hole, the polarization plane is generally tilted to the right, relative to the positive β-axis, which is an effect of the orbit velocity on the polarization vector; see section 5.3.3 for more details. Furthermore, if the emitter is spinning, the plane of polarization generally follows the surface velocities, in addition to the general shift by the orbit velocity. Similarly to the Schwarzschild case, the polarization plane makes a full revolution along one orbit, and the behaviour of it does not change qualitatively for different emitter geometries.

There are some effects visible when comparing the polarization planes of an emitter for Kerr black holes that are strongly co- and counter-rotating, relative to the sense of orbit revolution; in particular, see figures 6.3 and 6.7. The plane of polarization of an emitter in the equatorial plane of a co-rotating black hole with $a = 0.9M$ is appearing nearly vertical in the observer's screen for a spinnless emitter, where the polarization plane of a emitter in Schwarzschild spacetime is tilted to the right. This tilt is increased even further if the black hole is strongly counter-rotating, i.e. $a = -0.9M$, relative to the sense of direction of the orbit. This effect is a result of the frame-dragging of the black hole on the path of the light. For a strongly co-rotating black hole, the light has to be emitted further against the sense of direction of the orbit rotation, compared to the Schwarzschild case; this counteracts the effect of the orbit velocity on the plane of polarization, thus the plane of polarization is less tilted to the right. The opposite is true for a strongly counter-rotating black hole: the light has to be emitted further into the direction of the direction of orbit rotation to counteract the effect of the black hole dragging on the spacetime, thus the plane of polarization is further tilted to the right.

As discussed in section 5.3.3 for an emitter in the equatorial plane of a Schwarzschild object, this is a very simple model of initial polarization to investigate the influence of the spin on the plane of polarization at an arbitrary positioned, stationary observer in Kerr spacetime. For a more realistic model, one would have to impose further properties on the emitter, such as a

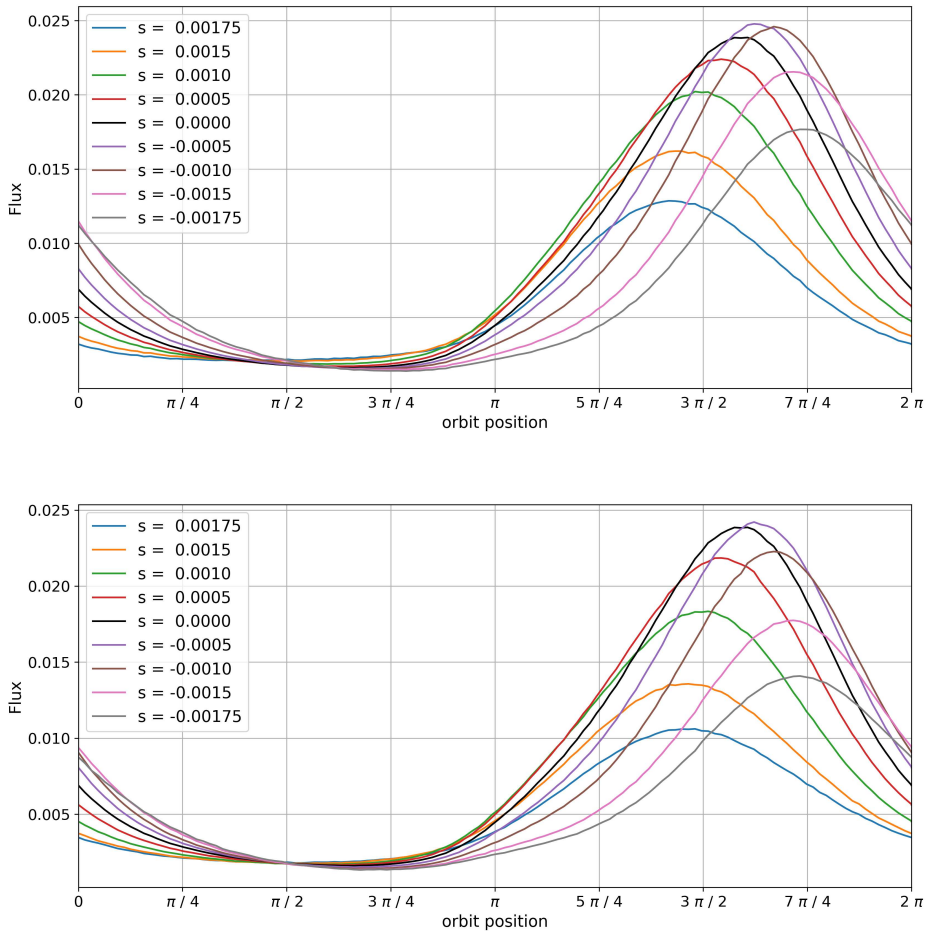

Figure 6.11: Flux at the observer's screen in arbitrary units along the emitter's orbit, where $a = -0.9M$. Top panel: Observed flux emitted by spherical light source. Bottom panel: Observed flux emitted by spheroidal light source. The different colors indicate different spin values.

magnetic field generating the polarization, see e.g. [46] and [43]. In the context of this thesis, however, the goal of modelling the polarization plane is to demonstrate the possibilities of the theory established in chapter 3; further introducing properties of the emitter would introduce more and different aspects of study, thus it is outside the scope of this thesis.

6.3.4 Influence of the spin on the flux

In this section, the flux of a spinning light source orbiting a Kerr black hole in the equatorial plane is studied in detail. While the distribution of redshift over the observed parts of the surface of the emitter is hardly resolvable even with modern instruments, the observed flux of light sources around heavy objects is a common used observable to study astrophysical objects. This section follows the theoretical considerations introduced in section 3.2.4.

For convenience, the equation for calculating the observed flux, given as the integrated redshift over the observed surface area, is repeated here from Eq. (3.85):

$$F_{\text{obs}} = \int\int g^3 \cdot I_{\text{em},\,\nu}\, \mathrm{d}\nu\, \mathrm{d}\omega = \int I_{\text{em}} \cdot g^4\, \mathrm{d}\omega\,, \tag{6.46}$$

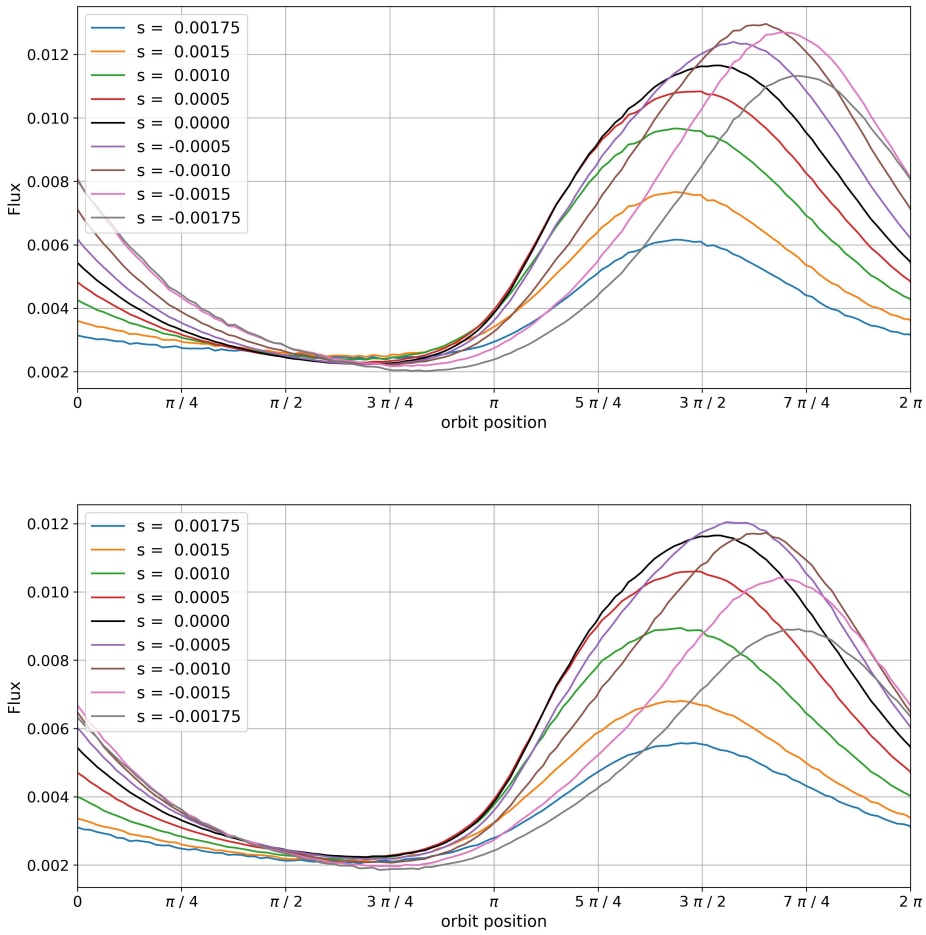

Figure 6.12: Flux at the observer's screen in arbitrary units along the emitter's orbit, where $a = 0.9M$. Top panel: Observed flux emitted by spherical light source. Bottom panel: Observed flux emitted by spheroidal light source. The different colors indicate different spin values.

where g is the energy fraction associated with the redshift of the light ray and $I_{\mathrm{em},\,\nu}$ is the emitted intensity profile. As mentioned before, the light is assumed to be monochromatic for simplicity, so the observed flux is an integral over g only. The observed flux for a strongly rotating black hole anti-parallel to the orbit sense of direction with $a = -0.9M$ can be seen in figure 6.11, both for a spherical and spheroidal emitter. Similarly, figure 6.12 depicts the observed flux for a strongly rotating black hole parallel to the orbit sense of direction with $a = +0.9M$, again both for a spherical and spheroidal emitter.

Both figures show the observed flux depending on the position φ_{em} of the emitter on its orbit in the equatorial plane of the black hole. Observed fluxes of light sources with differing spin are differentiated by their color; the spinless case $s = 0$ is indicated by the black line.
The general behavior of the observed flux is similar to the Schwarzschild case. For both values of black hole angular momentum, the observed flux decreases until $\varphi_{\mathrm{em}} \in [\pi/2,\ \pi]$, depending on the spin of the emitter. It then increases until $\varphi_{\mathrm{em}} \in [5\pi/4,\ 7\pi/4]$, and drops again afterwards. This general shape can be found independent on the shape of the emitter, and does not differ qualitatively on the black hole parameter a.
If the black hole angular momentum and the orbit angular momentum are anti-parallel, i.e.

$a = -0.9M$ and figure 6.11, the behavior of the flux for different spin values s of the emitter resembles the same behavior for an emitter orbiting a Schwarzschild object, see section 5.3.4 and figures 5.11 and 5.12. The position of the maximal flux increases monotonically with decreasing spin. Additionally, the height of the maximal flux depends on the spin, too, and does not vary monotonically. For increasingly positive values of spin, counter-rotating with the black hole and co-rotating with the orbit, the height of the maximal flux decreases, but the same cannot be said generally for increasingly negative values of spin. The observed flux here reaches its maximum between $s = -0.0005$ and $s = -0.0010$ for a spherical emitter and between $s = 0$ and $s = -0.0005$ for a spheroidal emitter; this effect is caused by the inclination of the observer at $\vartheta_{\mathrm{obs}} = \pi/3$. This is inline with the discussion for a spinning emitter in Schwarzschild spacetime. While the observed flux for $a = -0.9M$ is generally bigger, and the ratio of maximal to minimal flux, i.e. the sharpness of the flux curve, is greater for a rotating black hole, this effect cannot be uniquely attributed to the rotation, as the distance of the light source to the observer and the centre of gravity are not the same as in the Schwarzschild case.
However, if the black hole angular momentum and the orbit angular momentum are parallel, i.e. $a = 0.9M$ and figure 6.12, there are qualitative changes to the observed flux. The position of the maximal spin does still increase monotonically with decreasing spin values for negative spins, however, this is not the case for positive values of spin. For increasing values of spin, the position of the maximal flux decreases to earlier orbit positions at first, but then appears to stagnate and then even retract and move to later orbit positions for high values of positive spin, albeit only slight. Moreover, the effect of the spin on the height of maximal spin changes, relative to the Schwarzschild case. The height of maximal flux still decreases with increasingly positive values of spin, co-rotating with both the black hole and orbit; however, the observed flux reaches its maximum for more negative values of spin. It is maximal between $s = -0.001$ and $s = -0.0015$ for a spherical emitter, and around $s = -0.0005$ for a spheroidal emitter. In addition to this, it is possible to see that the observed flux is asymmetric around the maximal flux for non- and slowly spinning co-rotating emitters, i.e. more flux is observed before the position of maximal flux than after, best seen for $s = 0$ in figure 6.12. Furthermore, height of the minimal flux is lower for highly negative values of spin; for the Schwarzschild case and anti-parallel black hole angular momenta, the height of the minimal spin is approximately constant. It is also notable that the general amount of flux received for $a = 0.9M$ is smaller than in the Schwarzschild case and for a Kerr black hole with $a = -0.9M$. Again, however, this effect cannot be uniquely attributed to the rotation of the black hole, as the emitter is generally closer to the source of gravity, which increases the distance of the light source to the observer.

Chapter 7

Summary and Outlook

The goal of this thesis was to establish the theoretical description of a spinning light source orbiting a compact object that is stationary and axially symmetric, and study the influence of the spin on the observables associated to the light coming from the emitter. This may serve as the theoretical groundwork for describing e.g. hot spots in accretion discs and spinning neutron stars.

In this context, the first chapter dealt with the notion of the velocity of a spinning test particle along a circular orbit in the symmetry plane of such an object, the Mathisson–Papapetrou–Dixon equations. In particular, a brief overview was given and the influence of the choice of supplementary condition discussed.

The subsequent chapter was dedicated to establishing the general theory of spinning light sources in the symmetry plane of compact objects that are stationary, axially symmetric and asymptotically flat. This included defining an stationary observer at any point in spacetime, which also serves as the local reference frame of an observer at which to evaluate the observables. Then, by Lorentz transformation, the centre of mass reference frame was established, which co-moves with the orbital velocity. Then, the centre of momentum reference frame was defined as an observer that follows the normalized four-momentum of the emitter, rather than the tangent to the world line, as those two are not parallel anymore for spinning test-particles. Afterwards, the rest frame of the surface was introduced via Lorentz boost with the surface velocity, which depends on the emitter geometry. With the description of these reference frames, and solution of the lightlike geodesic equation for the given spacetime, the emitter-observer problem can be solved numerically; the procedure is also given in much detail. In the same chapter, the notion of a celestial sphere and screen at the observer is developed, in order to study the observables. The observables discussed include the plane of polarization, which is linearly polarized in the direction of the spin angular momentum, as measured in the surface rest frame, the redshift distribution across the image of the emitter on the observer's screen, as well as the observed flux, a result of integrating the redshift distribution along the image.

The third chapter dealt with the geometry of the emitter, and the influence of the geometry on the velocity of surface elements of the rigidly spinning light source. Specifically, two geometries were discussed: a spherical emitter, and a spheroidal emitter, described by a Maclaurin spheroid. Additionally, the limit of the spin values on the geometrical extension of the emitter was discussed in detail.

Afterwards, this theory was applied to a spinning emitter in the equatorial plane of a Schwarzschild object. This includes a brief overview of the Schwarzschild solution, as well as concreting the mentioned velocities for the given spacetime. Following this, the influence of the spin on the observables was studied in much detail for a fixed configuration of emitter

and observer.

First, the influence of gravity, spin and emitter geometry on the shape of the light source and redshift distribution on the observer's screen was discussed. Here, the effect of light bending on the appearance can be seen, especially for an emitter that is behind the Schwarzschild black hole, where the emitter takes on a nearly elliptical shape. The image appears spherical if the spherical emitter is in front of the Schwarzschild object instead. Additionally, the observed frequency of the light coming from the emitter is generally lower, compared to the emitted frequency, result of the gravitational pull on the light, commonly referred to as gravitational redshift. The influence of the spin on the redshift distribution was also discussed in detail; the frequency of the light emitted by surface elements moving towards the observer is increased, while the frequency of the light emitted by surface elements moving away from the observer is decreased. This effect is coupled to the effect of the orbital velocity on the redshift distribution, resulting in highly different distributions for co- and counter-rotating emitters.

Then, the influence of the spin on the polarization plane was discussed. It can be seen that, if the emitter is in front of the object, it is generally tilted to the right, relative to the up-direction (parallel to the axis $\beta = 0$) on the observer's screen, due to the influence of the orbital velocity. The tilt is influenced by the spin of the emitter, increasing or decreasing depending on the velocity of the emitting surface elements relative to the observer. This effect is stronger for higher magnitudes of spin.

Lastly, the influence of the spin on the observed flux was studied. This is of significant importance regarding astrophysical observations, as the redshift distribution is hardly resolvable, even by means of modern technology. It is clear to see that the spin influences not only the position of the maximal flux, but also its height. Peculiarly, the height of maximal flux does not vary monotonically with spin, but is rather non-monotonic for strongly counter-rotating emitters as a result of the observer inclination.

The last chapter dealt with the application of the theory of spinning light sources in a specific stationary and axially symmetric solution of Einstein's vacuum field equations, the Kerr spacetime. Following a brief overview of this solution, the velocities for an emitter orbiting a Kerr black hole specifically are discussed in detail. This is then proceeded by a study for a specific configuration of emitter and observer, that is chosen to have the same orbit duration on the observer's screen, relative to the configuration considered for the Schwarzschild case.

First, the influence of gravity, spin, emitter geometry, and importantly the black hole rotation, on the shape of the emitter and redshift distribution on the observer's screen is discussed. The effect of light bending on the appearance can be seen as well; however, another important effect arises from the rotation of the black hole, as frame-dragging shifts the position of the images of the emitter on the observer's screen. In particular, if the emitter is behind the black hole, the emitter appears not only elliptical, but also rotated, due to a combination of the light bending and frame-dragging. The influence of the spin of the emitter on the redshift distribution follows the same line of reasoning as described before, with only slight differences induced by the black hole rotation.

Afterwards, the influence of the spin and black hole rotation on the polarization plane is discussed. In general, the behaviour described for the plane of polarization in the Schwarzschild case is repeated here. Although the strength of the tilting of the polarization plane changes with the black hole rotation due to frame-dragging, this effect is rather small.

Lastly, the influence of the spin and black hole rotation on the observed flux was studied once more. The effect that the height of the maximal flux is highly non-monotonic for emitters strongly counter-rotating relative to the direction of orbit rotation is still visible here; however, the position of the maximal flux does not change monotonically anymore for strongly co-rotating black holes, relative to the sense of orbit rotation. This effect is not a result of the

observer's inclination, but rather of the black hole rotation and dragging of the path of light. Additionally, the spin value for which the peak of the flux curve is highest depends on the black hole rotation.

This closes the study of the influence of the spin on the light received from spinning emitters in the symmetry plane of compact objects that are axisymmetric, stationary and asymptotically flat. However, it may be interesting to extend the theory and this study in some of the following ways:

The model of the emitter established in this thesis is entirely sufficient for studying the general effects of the spin on the light received, but one may want to extend this to more astrophysically realistic emitter properties. For example, this may include a model of a magnetic field, which would also result in a more realistic initial polarization, motivated and generated by the magnetic field. Studying other emitter geometries might be of interest, too, especially for non-rigidly spinning emitters.

The light emitted by the light source is assumed to be isotropic and, with respect to the observed flux, monochromatic. This is the simplest form of radiation, that serves the purposes of this thesis, such that the effects of anisotropy and dispersion do not enter in the study of the observables, thus the focus can be placed on the influence of the spin and gravity. For a more realistic model, one might be interested in light that is not emitted isotropically, or only partly light emitting surface elements. In regards to the flux, other intensity profiles may affect the observed flux in notable ways, where modelling the light to emit black body radiation comes to mind.

Throughout this thesis, the spin of the emitter is assumed to be either parallel or anti-parallel to the orbit angular momentum, as it allows us to study the effect of spin and the coupling to the orbit angular momentum. For further generalization, one may be able to extend this study for arbitrary spin directions, in order to study the effect of precession on the observables.

If this theory is to be implemented to describe, for example, a hot spot in the accretion disk in the vicinity of a black hole, it might be useful to investigate the effect of a plasma in the path between the emitter and observer. As this theory does not limit the matter or its distribution in space, this may be a simple extension to studying the influence of the spin on the light observed.

Another possible extension of the model, outside the scope of this thesis, is the influence of the gravity of the emitter on the emitted light. This would lead to information of parts of the surface of the emitter that are not visible in the context of the theory established here, and may be interesting when modelling the emission of neutron stars; in particular, the papers of Bodanov et al. [16, 17] introduce such a model for a neutron star as the central object and source of gravity, and may thus be used as preparatory material in this context.

Lastly, one may also be interested in other choices of sources of gravity. If e.g. the emitter is assumed to possess a magnetic field, it may be worthwhile to investigate the emission of light sources in the symmetry plane of charged solutions of the field equations, e.g. the Kerr-Newman solution. Studying the influence of other axisymmetric solutions, such as the q-metric [69], which described a quadrupolar mass distribution, may also be a intriguing prospect.

Appendix A

Additional calculations

A.1 Relative velocity for small spin approximation for Schwarzschild

Recall from Eqs. (5.28) that for a spinning test-particle in the equatorial plane of a Schwarzschild object, the relative velocity is given by

$$\mathcal{V}^2 = 1 - \frac{(1-\chi_v^2)(1-\chi_u^2)}{(1-\chi_u\chi_v)^2} \,, \tag{A.1}$$

where

$$\chi_v = \frac{-3M^2 s \pm \sqrt{4Mr^3 + 13M^4 s^2 - 8M^7 s^4/r^3}}{2\sqrt{r^2-2Mr}(r - M^3 s^2/r^2)} =: \frac{-3M^2 s \pm \alpha(s)}{2\sqrt{r^2-2Mr}\beta(s)} \,, \tag{A.2}$$

$$\chi_u = \frac{r - M^3 s^2/r^2}{r + 2M^3 s^2/r^2} \cdot \chi_v =: \frac{\delta(s)}{\gamma(s)} \cdot \chi_v \,. \tag{A.3}$$

We want to approximate the relative velocity up to the first non-vanishing order in s for small spin values, i.e. $s \to 0$.

A.1.1 Approximation for zeroth order in spin

In leading terms of s^0, it is trivial to see that $\mathcal{V}$ vanishes, as $\chi_v = \chi_u$. This effect is only emerging from the fact that the test-particle is spinning, see section 2 or 5.2.2 for more details.

A.1.2 Approximation for first order in spin

For the approximation of the relative velocity in first order in s, the derivative of the relative velocity in s is needed:

$$\partial_s \mathcal{V}^2 = \frac{2\chi_v \partial_s \chi_v (1-\chi_u^2) + 2\chi_u \partial_s \chi_u (1-\chi_v^2)}{(1-\chi_u\chi_v)^2} \tag{A.4}$$

$$- \frac{(2\chi_u \cdot \partial_s \chi_v + 2\chi_v \cdot \partial_s \chi_u)(1-\chi_u^2)(1-\chi_v^2)}{(1-\chi_u\chi_v)^3} \,, \tag{A.5}$$

including the derivatives of the quantities χ_v and χ_u:

$$\partial_s \chi_v = \frac{1}{2\sqrt{r^2-2Mr}} \Bigg[-\frac{3M^2}{\beta(s)} \tag{A.6}$$

$$\pm \frac{13M^4 s - 16M^7 s^3/r^3}{\alpha(s)\beta(s)} \tag{A.7}$$

$$+ \frac{2M^3 s(-3Ms^2 \pm \alpha(s))}{r^2 \beta(s)^2} \Bigg] \tag{A.8}$$

and

$$\partial_s \chi_u = -\left(\frac{2M^3}{r^2\gamma(s)} + \frac{4M^3\delta(s)}{r^2\gamma(s)^2}\right)\chi_v \cdot s \tag{A.9}$$

$$+ \frac{\delta(s)}{\gamma(s)}\partial_s\chi_v \,. \tag{A.10}$$

Investigating the behavior of the derivatives, as well as the quantities χ_v and χ_u themselves, for vanishing spin reveals:

$$\chi_v\big|_{s=0} = \pm\sqrt{\frac{Mr}{r^2-2Mr}}\,, \tag{A.11}$$

$$\chi_u\big|_{s=0} = \chi_v\Big|_{s=0}\,, \tag{A.12}$$

$$\partial_s\chi_v\big|_{s=0} = -\frac{3M^2}{r\sqrt{r^2-2Mr}}\,, \tag{A.13}$$

$$\partial_s\chi_u\big|_{s=0} = \partial_s\chi_v\big|_{s=0}\,. \tag{A.14}$$

We can thus rewrite the quantities $\chi_v(s=0) = \chi_u(s=0) =: \chi$ and the derivatives $\partial_s\chi_v(s=0) = \partial_s\chi_u(s=0) =: \chi'$, and see that the relative velocity vanishes in first order in s:

$$\mathcal{V}^2 \approx \partial_s\mathcal{V}^2\big|_{s=0}\cdot s \tag{A.15}$$

$$= \left[\frac{4\chi\chi'(1-\chi^2)}{(1-\chi^2)^2} - \frac{4\chi\chi'(1-\chi^2)^2}{(1-\chi^2)^3}\right]\cdot s \tag{A.16}$$

$$= 0\,. \tag{A.17}$$

A.1.3 Approximation for second order in spin

For the approximation of the relative velocity in second order in s, the second order derivative of $\mathcal{V}^2$ in terms of the spin is needed:

$$\partial_s^2\mathcal{V}^2 = \frac{\left(2\left(\partial_s\chi_v\right)^2 + \chi_v\left(\partial_s^2\chi_v\right)\right)(1-\chi_u^2) + \left(2\left(\partial_s\chi_u\right)^2 + \chi_u\left(\partial_s^2\chi_u\right)\right)(1-\chi_v^2)}{(1-\chi_u\chi_v)^2}$$

$$- \frac{(2\chi_u\cdot\partial_s\chi_v + 2\chi_v\cdot\partial_s\chi_u)(2\chi_v\partial_s\chi_v(1-\chi_u^2) + 2\chi_u\partial_s\chi_u(1-\chi_v^2))}{(1-\chi_u\chi_v)^3} \tag{A.18}$$

$$- \frac{\left(2\chi_u(\partial_s^2\chi_v) + 4(\partial_s\chi_u)(\partial_s\chi_v) + 2\chi_v(\partial_s^2\chi_u)\right)(1-\chi_u^2)(1-\chi_v^2)}{(1-\chi_u\chi_v)^3} \tag{A.19}$$

$$+ \frac{(2\chi_u\cdot\partial_s\chi_v + 2\chi_v\cdot\partial_s\chi_u)(2\chi_v\partial_s\chi_v(1-\chi_u^2) + 2\chi_u\partial_s\chi_u(1-\chi_v^2))}{(1-\chi_u\chi_v)^3} \tag{A.20}$$

$$+ \frac{(3\chi_u\partial_s\chi_v + 3\chi_v\partial_s\chi_u)(2\chi_u\cdot\partial_s\chi_v + 2\chi_v\cdot\partial_s\chi_u)(1-\chi_u^2)(1-\chi_v^2)}{(1-\chi_u\chi_v)^4}\,, \tag{A.21}$$

where it is important to note that the second and fourth terms cancel. Before simplifying this further for evaluating this at $s=0$, we extend the list of partial derivatives by the second-order

derivatives of χ_v and χ_u:

$$\partial_s^2\chi_v = \frac{1}{2\sqrt{r^2-2Mr}}\Bigg[-\frac{6M^5 s}{r^2\beta(s)^2} \pm \frac{13M^4 - 48M^7 s^2/r^3}{\alpha(s)\beta(s)} \tag{A.22}$$

$$\pm\left(13M^4 s - 16M^7\frac{s^3}{r^3}\right)\left(-\frac{13M^4 s - 16M^7 s^3/r^3}{2\alpha^3\beta(s)} + \frac{2M^3 s}{r^2\alpha(s)\beta(s)^2}\right) \tag{A.23}$$

$$-\frac{18M^3 s^2 \pm 2M^3\alpha(s)}{r^2\beta(s)^2} \pm \frac{26M^7 s^2 - 32M^{10}s^4/r^3}{r^2\alpha(s)\beta(s)} + \frac{4M^6 s^2(-3Ms^2 \pm \alpha(s))}{r^2\beta(s)^3}\Bigg]$$

and

$$\partial_s^2\chi_u = -\left(\frac{2M^3}{r^2\gamma(s)} + \frac{4M^3\delta(s)}{r^2\gamma(s)^2}\right)\chi_v + \left(\frac{4M^6 + 2M^3}{r^4\gamma(s)^2} + \frac{32M^6\delta(s)}{r^4\gamma(s)^3}\right)\chi_v \cdot s^2 \tag{A.24}$$

$$-\left(\frac{2M^3}{r^2\gamma(s)} + \frac{4M^3\delta(s)}{r^2\gamma(s)^2}\right)\partial_s\chi_v \cdot s + \frac{\delta(s)}{\gamma(s)}\partial_s^2\chi_v\,. \tag{A.25}$$

Extending the list of quantities at $s = 0$ in Eqs. (A.11) to (A.14) with the second-order derivatives of the quantities χ_v and χ_u reveals:

$$\partial_s^2\chi_v\big|_{s=0} = \pm\frac{1}{2\sqrt{r^2-2Mr}}\left[\frac{13M^4}{\alpha(0)\beta(0)} + \frac{2M^3\alpha(0)}{r^2\beta(0)^2}\right] = \pm\frac{21M^4}{4\sqrt{M(r-2M)}}\,, \tag{A.26}$$

$$\partial_s^2\chi_u\big|_{s=0} = -\frac{2M^3\gamma(0) + 4M^3\delta(0)}{r^2\gamma(0)}\chi_v(s=0) + \frac{\delta(0)}{\gamma(0)}\partial_s^2\chi_v\big|_{s=0} \tag{A.27}$$

$$= \pm\frac{6M^3}{r^3}\sqrt{\frac{Mr}{r^2-2Mr}} + \partial_s^2\chi_v\big|_{s=0}\,. \tag{A.28}$$

Again, we rewrite the quantities $\chi_v(s=0) = \chi_u(s=0) =: \chi$ and the derivatives $\partial_s\chi_v(s = 0) = \partial_s\chi_u(s=0) =: \chi'$, as well as the second-order derivatives $\partial_s^2\chi_v(s=0) = \chi'' =: \partial_s^2\chi_u \mp u(r)$, in order to simplify the second-order approximation of the relative velocity first:

$$\partial_s^2\mathcal{V}\Big|_{s=0} = \frac{4(\chi')^2 + \chi(2\chi'' \pm u(r))}{1-\chi^2} \tag{A.29}$$

$$-\frac{2\chi(2\chi'' \pm u(r)) + 4(\chi')^2}{1-\chi^2} \tag{A.30}$$

$$+\frac{24\chi^2(\chi')^2}{(1-\chi^2)^2} \tag{A.31}$$

$$= \frac{24\chi^2(\chi')^2 - \chi(2\chi'' \pm u(r))}{(1-\chi^2)^2}\,. \tag{A.32}$$

Thus, we can write the second order approximation of the relative velocity:

$$\mathcal{V}^2\Big|_{s=0} \approx \frac{288M^5(r-2M) \mp M^4 r(r^2-2Mr)^2(21r^3+12)}{2r(r^2-3Mr)^2(r-2M)} \cdot s^2 + \mathcal{O}(s^3)\,. \tag{A.33}$$

A.2 Relative velocity for small spin approximation for Kerr

Recall from Eqs. (5.28) that for a spinning test-particle in the equatorial plane of a Kerr black hole, the relative velocity is given by

$$\mathcal{V}^2 = 1 - \frac{(1-\chi_v^2)(1-\chi_u^2)}{(1-\chi_u\chi_v)^2} \,, \tag{A.34}$$

where

$$\chi_v = \frac{-(2ra + 3M^2 s + aM^3 s^2/r^2) \pm \sqrt{\chi_0}}{2\sqrt{\Delta}(r - M^3 s^2/r^2)} =: \frac{-(2ra + 3M^2 s + aM^3 s^2/r^2) \pm \alpha(s)}{2\sqrt{\Delta}\beta(s)} \,, \tag{A.35}$$

$$\chi_u = \frac{r - M^3 s^2/r^2}{r + 2M^3 s^2/r^2} \cdot \chi_v =: \frac{\delta(s)}{\gamma(s)} \cdot \chi_v \,, \tag{A.36}$$

$$\chi_0 := 4Mr^3 + 12aM^2 rs + 13M^4 s^2 + 6aM^5 s^3/r^2 - 8M^7 s^4/r^3 + 9a^2 M^6 s^4/r^4 \,. \tag{A.37}$$

We want to approximate the relative velocity up to the first non-vanishing order in s for small spin values, i.e. $s \to 0$.

A.2.1 Approximation for zeroth order in spin

In leading terms of s^0, it is trivial to see that $\mathcal{V}$ vanishes, as $\chi_v = \chi_u$. This effect is only emerging from the fact that the test-particle is spinning, see section 2 or 6.3.2 for more details.

A.2.2 Approximation for first order in spin

For the approximation of the relative velocity in first order in s, the derivative of the relative velocity in s is needed:

$$\partial_s \mathcal{V}^2 = \frac{2\chi_v \partial_s \chi_v (1-\chi_u^2) + 2\chi_u \partial_s \chi_u (1-\chi_v^2)}{(1-\chi_u\chi_v)^2} \tag{A.38}$$

$$- \frac{(2\chi_u \cdot \partial_s \chi_v + 2\chi_v \cdot \partial_s \chi_u)(1-\chi_u^2)(1-\chi_v^2)}{(1-\chi_u\chi_v)^3} \,, \tag{A.39}$$

where the derivatives of the quantities χ_v and χ_u now read

$$\partial_s \chi_v = \frac{1}{2\sqrt{\Delta}} \Bigg[- \frac{3M^2 + 2aM^3 s/r^2}{\beta(s)} \tag{A.40}$$

$$\pm \frac{6aM^2 r + 13M^4 s + 9aM^5 s^2/r^2 - 16M^7 s^3/r^3 + 18a^2 M^6 s^3/r^4}{\alpha(s)\beta(s)} \tag{A.41}$$

$$+ \frac{2M^3 s(-(2ra + 3M^2 s + aM^3 s^2/r^2) \pm \alpha(s))}{r^2 \beta(s)^2} \Bigg] \tag{A.42}$$

and

$$\partial_s \chi_u = - \left(\frac{2M^3}{r^2 \gamma(s)} + \frac{4M^3 \delta(s)}{r^2 \gamma(s)^2} \right) \chi_v \cdot s + \frac{\delta(s)}{\gamma(s)} \partial_s \chi_v \,. \tag{A.43}$$

Investigating the behaviour of all those quantities for $s = 0$ yields:

$$\chi_v\big|_{s=0} = -\frac{a \pm \sqrt{Mr}}{2\sqrt{\Delta}} \,, \tag{A.44}$$

$$\chi_u\big|_{s=0} = \chi_v\Big|_{s=0} \,, \tag{A.45}$$

$$\partial_s\chi_v\big|_{s=0} = -\frac{3M^2(\sqrt{Mr} \pm a)}{2\sqrt{\Delta M r^3}} \,, \tag{A.46}$$

$$\partial_s\chi_u\big|_{s=0} = \partial_s\chi_v\big|_{s=0} \,. \tag{A.47}$$

We can again rewrite the quantities $\chi_v(s=0) = \chi_u(s=0) =: \chi$ and the derivatives $\partial_s\chi_v(s=0) = \partial_s\chi_u(s=0) =: \chi'$, and see that the relative velocity vanishes in first order in s, following the same argument as used for the Schwarzschild case:

$$\mathcal{V}^2 \approx \partial_s\mathcal{V}^2\big|_{s=0} \cdot s \tag{A.48}$$

$$= \left[\frac{4\chi\chi'(1-\chi^2)}{(1-\chi^2)^2} - \frac{4\chi\chi'(1-\chi^2)^2}{(1-\chi^2)^3}\right] \cdot s \tag{A.49}$$

$$= 0 \,. \tag{A.50}$$

A.2.3 Approximation for second order in spin

For the approximation of the relative velocity in second order in s, the second-order derivative of $\mathcal{V}^2$, in terms of the spin s, is used; recall that

$$\partial_s^2\mathcal{V}^2 = \frac{\left(2\left(\partial_s\chi_v\right)^2 + \chi_v\left(\partial_s^2\chi_v\right)\right)(1-\chi_u^2) + \left(2\left(\partial_s\chi_u\right)^2 + \chi_u\left(\partial_s^2\chi_u\right)\right)(1-\chi_v^2)}{(1-\chi_u\chi_v)^2}$$

$$- \frac{\left(2\chi_u(\partial_s^2\chi_v) + 4(\partial_s\chi_u)(\partial_s\chi_v) + 2\chi_v(\partial_s^2\chi_u)\right)(1-\chi_u^2)(1-\chi_v^2)}{(1-\chi_u\chi_v)^3} \tag{A.51}$$

$$+ \frac{(3\chi_u\partial_s\chi_v + 3\chi_v\partial_s\chi_u)(2\chi_u\cdot\partial_s\chi_v + 2\chi_v\cdot\partial_s\chi_u)(1-\chi_u^2)(1-\chi_v^2)}{(1-\chi_u\chi_v)^4} \,. \tag{A.52}$$

We give the partial derivatives with the second-order derivatives of χ_v and χ_u, namely

$$\partial_s^2\chi_v = \frac{1}{2\sqrt{\Delta}}\Bigg[-\frac{2aM^3}{r^2\beta(s)} - \frac{6M^5s + 4aM^6s^2/r^2}{r^2\beta(s)^2} \tag{A.53}$$

$$\pm \frac{13M^4 + 18aM^5s/r^2 - 48M^7s^2/r^3 + 54a^2M^6s^2/r^4}{\alpha(s)\beta(s)} \tag{A.54}$$

$$\pm (6aM^2r + 13M^4s + 9aM^5s^2/r^2 - 16M^7s^3/r^3 + 18a^2M^6s^3/r^4)\cdot \tag{A.55}$$

$$\left(\frac{2M^3s}{r^3\alpha(s)\beta(s)^2} - \frac{6aM^2r + 13M^4s + 9aM^5s^2/r^2 - 16M^7s^3/r^3 + 18a^2M^6s^3/r^4}{2\alpha^3(s)\beta(s)}\right)$$

$$- \frac{4M^3ra + 12M^5s + 6aM^6s^2/r^2 \mp \alpha(s)}{r^2\beta(s)^2} \tag{A.56}$$

$$+ \frac{8M^6s^2(-(2ra + 3M^2s + aM^3s^2/r^2) \pm \alpha(s))}{r^4\beta(s)^3}\Bigg] \tag{A.57}$$

and

$$\partial_s^2\chi_u = -\left(\frac{2M^3}{r^2\gamma(s)} + \frac{4M^3\delta(s)}{r^2\gamma(s)^2}\right)\chi_v + \left(\frac{4M^6+2M^3}{r^4\gamma(s)^2} + \frac{32M^6\delta(s)}{r^4\gamma(s)^3}\right)\chi_v\cdot s^2 \tag{A.58}$$

$$-\left(\frac{2M^3}{r^2\gamma(s)} + \frac{4M^3\delta(s)}{r^2\gamma(s)^2}\right)\partial_s\chi_v\cdot s + \frac{\delta(s)}{\gamma(s)}\partial_s^2\chi_v\,. \tag{A.59}$$

Extending the list of quantities at $s = 0$ in Eqs. (A.11) to (A.14) with the second-order derivatives of the quantities χ_v and χ_u reveals:

$$\partial_s^2\chi_v\big|_{s=0} = -\frac{2aM+4aM^3r}{r^4} \pm \frac{31M^4r - 9a^2M^3}{4r^3\sqrt{Mr}} \tag{A.60}$$

$$\partial_s^2\chi_u\big|_{s=0} = \pm\frac{6M^3}{r^3}\sqrt{\frac{Mr}{r^2-2Mr}} + \partial_s^2\chi_v\big|_{s=0} \tag{A.61}$$

Again, we rewrite the quantities $\chi_v(s=0) = \chi_u(s=0) =: \chi$ and the derivatives $\partial_s\chi_v(s=0) = \partial_s\chi_u(s=0) =: \chi'$, as well as the second-order derivatives $\partial_s^2\chi_v(s=0) = \chi'' =: \partial_s^2\chi_u \mp u(r)$, in order to simplify the second-order approximation of the relative velocity first:

$$\partial_s^2\mathcal{V}\Big|_{s=0} = \frac{24\chi^2(\chi')^2 - \chi(2\chi'' \pm u(r))}{(1-\chi^2)^2}\,. \tag{A.62}$$

Thus, we can write the second-order approximation of the relative velocity for a spinning test-particle in the equatorial plane of a Kerr black hole as

$$\mathcal{V}^2\Big|_{s=0} \approx \Bigg[\frac{108M^3(a\pm\sqrt{Mr})^4}{r^3\left(4\Delta - (a\pm\sqrt{Mr})^2\right)^2} - \frac{4aM+8aM^3r}{r^4} \tag{A.63}$$

$$\pm\frac{31M^4\sqrt{r^2-2Mr} - 9a^2M\sqrt{r^2-2Mr} + 24M^4r}{4r^4\sqrt{M(r-2M)}}\Bigg]\cdot s^2 + \mathcal{O}(s^3) \tag{A.64}$$

A.3 Polarization vector at any point in spacetime

A.3.1 Polarization vector in Schwarzschild spacetime

In this section, the exact formula for the polarization vector f^μ is given, as defined in section 5.3.3. Recall the determining equation for the components of the polarization vector at any point in spacetime, relative to the tangent of the worldline k^μ:

$$\kappa_1 = r\left(k^t f^r - k^r f^t\right) , \tag{A.65}$$

$$\kappa_2 = -r^3\left(k^\varphi f^\vartheta - k^\vartheta f^\varphi\right) , \tag{A.66}$$

$$1 = -g_{tt}\left(f^t\right)^2 + g_{rr}\left(f^r\right)^2 + g_{\vartheta\vartheta}\left(f^\vartheta\right)^2 + g_{\varphi\varphi}\left(f^\varphi\right)^2 , \tag{A.67}$$

$$0 = -g_{tt} f^t k^t + g_{rr} f^r k^r + g_{\vartheta\vartheta} f^\vartheta k^\vartheta + g_{\varphi\varphi} f^\varphi k^\varphi , \tag{A.68}$$

where $\kappa_{1,\,2}$ are the real and imaginary parts of the Penrose-Walker constant, and $g_{\mu\nu}$ are the components of the metric tensor of the Schwarzschild solution, see Eq. (5.1). The computations of the components of the polarization vector become quite unhandy, as this set of equations is non-linear, due to Eq. (A.67). This results in the following components of f^μ:

$$f^t = \frac{T_{\text{nom}} \pm \alpha k^t(\beta(k^\varphi)^2\sqrt{\Xi_{T1}} - (k^\vartheta)^2\sqrt{\Xi_{t2}})}{r \cdot T_{\text{denom}}} , \tag{A.69}$$

$$f^r = \frac{R_{\text{nom}} \pm \alpha k^r(\beta(k^\varphi)^2\sqrt{\Xi_{R1}} - (k^\vartheta)^2\sqrt{\Xi_{R2}})}{r \cdot R_{\text{denom}}} , \tag{A.70}$$

$$f^\vartheta = \frac{\theta_{\text{nom}} \pm k^\vartheta\sqrt{\Xi_\theta}}{r^3 \cdot \theta_{\text{denom}}} , \tag{A.71}$$

$$f^\varphi = \frac{\phi_{\text{nom}} \pm k^\varphi\sqrt{\Xi_\phi}}{r^3 \cdot \phi_{demon}} , \tag{A.72}$$

where the terms, in terms of appearance, are defined as follows:

$$\alpha = 1 - \frac{2M}{r} , \qquad \beta = \sin^2\vartheta .$$

For the t-component:

$$\begin{aligned} T_{\text{nom}} = &+ 2\alpha^3\beta k^\varphi (k^t)^3 k^\vartheta \kappa_2 + \alpha^2\beta(k^\varphi)^2 k^r (k^t)^2 \kappa_1 \quad - \alpha^2 k^r (k^t)^2 (k^\vartheta)^2 \kappa_1 \\ &+ \alpha\beta^2 (k^\varphi)^4 k^r \kappa_1 r^2 \quad + 2\alpha\beta(k^\varphi)^2 k^r (k^\vartheta)^2 \kappa_1 r^2 - 2\alpha\beta k^\varphi (k^r)^2 k^t k^\vartheta \kappa_2 \\ &+ \alpha k^r (k^\vartheta)^4 \kappa_1 r^2 \quad - \beta(k^\varphi)^2 (k^r)^3 \kappa_1 \quad + (k^r)^3 (k^\vartheta)^2 \kappa_1 \end{aligned}$$

$$
\begin{aligned}
\Xi_{T1} = &- \alpha^4\beta(k^\varphi)^2(k^t)^4r^4 && + \alpha^4\beta(k^t)^4\kappa_2^2 && + \alpha^4(k^t)^4(k^\vartheta)^2r^4 \\
&- \alpha^3\beta^2(k^\varphi)^4(k^t)^2r^6 && + \alpha^3\beta^2(k^\varphi)^2(k^t)^2\kappa_2^2r^2 && - 2\alpha^3\beta(k^\varphi)^2(k^t)^2(k^\vartheta)^2r^6 \\
&+ \alpha^3\beta(k^\varphi)^2(k^t)^2\kappa_1^2r^2 && - \alpha^3\beta(k^t)^2(k^\vartheta)^2\kappa_2^2r^2 && - \alpha^3(k^t)^2(k^\vartheta)^4r^6 \\
&- \alpha^3(k^t)^2(k^\vartheta)^2\kappa_1^2r^2 && + \alpha^2\beta^2(k^\varphi)^4\kappa_1^2r^4 && + 2\alpha^2\beta(k^\varphi)^2(k^r)^2(k^t)^2r^4 \\
&+ 2\alpha^2\beta(k^\varphi)^2(k^\vartheta)^2\kappa_1^2r^4 && - 2\alpha^2\beta(k^r)^2(k^t)^2\kappa_2^2 && - 2\alpha^2(k^r)^2(k^t)^{2sq}(k^\vartheta)^2r^4 \\
&+ \alpha^2(k^\vartheta)^4\kappa_1^2r^4 && + \alpha\beta^2(k^\varphi)^4(k^r)^2r^6 && - \alpha\beta^2(k^\varphi)^2(k^r)^2\kappa_2^2r^2 \\
&+ 2\alpha\beta(k^\varphi)^2(k^r)^2(k^\vartheta)^2r^6 && - \alpha\beta(k^\varphi)^2(k^r)^2\kappa_1^2r^2 && + \alpha\beta(k^r)^2(k^\vartheta)^2\kappa_2^2r^2 \\
&+ \alpha(k^r)^2(k^\vartheta)^4r^6 && + \alpha(k^r)^2(k^\vartheta)^2\kappa_1^2r^2 && - \beta(k^\varphi)^2(k^r)^4r^4 \\
&+ \beta(k^r)^4\kappa_2^2 && + (k^r)^4(k^\vartheta)^2r^4
\end{aligned}
$$

$$
\begin{aligned}
\Xi_{T2} = &- \alpha^4\beta(k^\varphi)^2(k^t)^4r^4 && + \alpha^4\beta(k^t)^4\kappa_2^2 && + \alpha^4(k^t)^4(k^\vartheta)^2r^4 \\
&- \alpha^3\beta^2(k^\varphi)^4(k^t)^2r^6 && + \alpha^3\beta^2(k^\varphi)^2(k^t)^2\kappa_2^2r^2 && - 2\alpha^3\beta(k^\varphi)^2(k^t)^2(k^\vartheta)^2r^6 \\
&+ \alpha^3\beta(k^\varphi)^2(k^t)^2\kappa_1^2r^2 && - \alpha^3\beta(k^t)^2(k^\vartheta)^2\kappa_2^2r^2 && - \alpha^3(k^t)^2(k^\vartheta)^4r^6 \\
&- \alpha^3(k^t)^2(k^\vartheta)^2\kappa_1^2r^2 && + \alpha^2\beta^2(k^\varphi)^4\kappa_1^2r^4 && + 2\alpha^2\beta(k^\varphi)^2(k^r)^2(k^t)^2r^4 \\
&+ 2\alpha^2\beta(k^\varphi)^2(k^\vartheta)^2\kappa_1^2r^4 && - 2\alpha^2\beta(k^r)^2(k^t)^2\kappa_2^2 && - 2\alpha^2(k^r)^2(k^t)^2(k^\vartheta)^2r^4 \\
&+ \alpha^2(k^\vartheta)^4\kappa_1^2r^4 && + \alpha\beta^2(k^\varphi)^4(k^r)^2r^6 && - \alpha\beta^2(k^\varphi)^2(k^r)^2\kappa_2^2r^2 \\
&+ 2\alpha\beta(k^\varphi)^2(k^r)^2(k^\vartheta)^2r^6 && - \alpha\beta(k^\varphi)^2(k^r)^2\kappa_1^2r^2 && + \alpha\beta(k^r)^2(k^\vartheta)^2\kappa_2^2r^2 \\
&+ \alpha(k^r)^2(k^\vartheta)^4r^6 && + \alpha(k^r)^2(k^\vartheta)^2\kappa_1^2r^2 && - \beta(k^\varphi)^2(k^r)^4r^4 \\
&+ \beta(k^r)^4\kappa_2^2 && + (k^r)^4(k^\vartheta)^2r^4
\end{aligned}
$$

$$
\begin{aligned}
T_{\text{denom}} = &+ \alpha^4\beta(k^\varphi)^2(k^t)^4 && - \alpha^4(k^t)^4(k^\vartheta)^2 && + \alpha^3\beta^2(k^\varphi)^4(k^t)^2r^2 \\
&+ 2\alpha^3\beta(k^\varphi)^2(k^t)^2(k^\vartheta)^2r^2 && + \alpha^3(k^t)^2(k^\vartheta)^4r^2 && - 2\alpha^2\beta(k^\varphi)^2(k^r)^2(k^t)^2 \\
&+ 2\alpha^2(k^r)^2(k^t)^2(k^\vartheta)^2 && - \alpha\beta^2(k^\varphi)^4(k^r)^2r^2 && - 2\alpha\beta(k^\varphi)^2(k^r)^2(k^\vartheta)^2r^2 \\
&- \alpha(k^r)^2(k^\vartheta)^4r^2 && + \beta(k^\varphi)^2(k^r)^4 - (k^r)^4(k^\vartheta)^2
\end{aligned}
$$

For the r-component:

$$
\begin{aligned}
R_{\text{nom}} = &+ \alpha(\alpha^3\beta(k^\varphi)^2(k^t)^3\kappa_1 && - \alpha^3(k^t)^3(k^\vartheta)^2\kappa_1 && + \alpha^2\beta^2(k^\varphi)^4k^t\kappa_1r^2 \\
&+ 2\alpha^2\beta(k^\varphi)^2k^t(k^\vartheta)^2\kappa_1r^2 && + 2\alpha^2\beta k^\varphi k^r(k^t)^2k^\vartheta\kappa_2 && + \alpha^2k^t(k^\vartheta)^4\kappa_1r^2 \\
&- \alpha\beta(k^\varphi)^2(k^r)^2k^t\kappa_1 && + \alpha(k^r)^2k^t(k^\vartheta)^2\kappa_1 && - 2\beta k^\varphi(k^r)^3k^\vartheta\kappa_2)
\end{aligned}
$$

$$
\begin{aligned}
\Xi_{R1} = &- \alpha^4\beta(k^\varphi)^2(k^t)^4r^4 &&+ \alpha^4\beta(k^t)^4\kappa_2^2 &&+ \alpha^4(k^t)^4(k^\vartheta)^2r^4\\
&- \alpha^3\beta^2(k^\varphi)^4(k^t)^2r^6 &&+ \alpha^3\beta^2(k^\varphi)^2(k^t)^2\kappa_2^2r^2 &&- 2\alpha^3\beta(k^\varphi)^2(k^t)^2(k^\vartheta)^2r^6\\
&+ \alpha^3\beta(k^\varphi)^2(k^t)^2\kappa_1^2r^2 &&- \alpha^3\beta(k^t)^2(k^\vartheta)^2\kappa_2^2r^2 &&- \alpha^3(k^t)^2(k^\vartheta)^4r^6\\
&- \alpha^3(k^t)^2(k^\vartheta)^2\kappa_1^2r^2 &&+ \alpha^2\beta^2(k^\varphi)^4\kappa_1^2r^4 &&+ 2\alpha^2\beta(k^\varphi)^2(k^r)^2(k^t)^2r^4\\
&+ 2\alpha^2\beta(k^\varphi)^2(k^\vartheta)^2\kappa_1^2r^4 &&- 2\alpha^2\beta(k^r)^2(k^t)^2\kappa_2^2 &&- 2\alpha^2(k^r)^2(k^t)^2(k^\vartheta)^2r^4\\
&+ \alpha^2(k^\vartheta)^4\kappa_1^2r^4 &&+ \alpha\beta^2(k^\varphi)^4(k^r)^2r^6 &&- \alpha\beta^2(k^\varphi)^2(k^r)^2\kappa_2^2r^2\\
&+ 2\alpha\beta(k^\varphi)^2(k^r)^2(k^\vartheta)^2r^6 &&- \alpha\beta(k^\varphi)^2(k^r)^2\kappa_1^2r^2 &&+ \alpha\beta(k^r)^2(k^\vartheta)^2\kappa_2^2r^2\\
&+ \alpha(k^r)^2(k^\vartheta)^4r^6 &&+ \alpha(k^r)^2(k^\vartheta)^2\kappa_1^2r^2 &&- \beta(k^\varphi)^2(k^r)^4r^4\\
&+ \beta(k^r)^4\kappa_2^2 &&+ (k^r)^4(k^\vartheta)^2r^4
\end{aligned}
$$

$$
\begin{aligned}
\Xi_{R2} = &- \alpha^4\beta(k^\varphi)^2(k^t)^4r^4 &&+ \alpha^4\beta(k^t)^4\kappa_2^2 &&+ \alpha^4(k^t)^4(k^\vartheta)^2r^4\\
&- \alpha^3\beta^2(k^\varphi)^4(k^t)^2r^6 &&+ \alpha^3\beta^2(k^\varphi)^2(k^t)^2\kappa_2^2r^2 &&- 2\alpha^3\beta(k^\varphi)^2(k^t)^2(k^\vartheta)^2r^6\\
&+ \alpha^3\beta(k^\varphi)^2(k^t)^2\kappa_1^2r^2 &&- \alpha^3\beta(k^t)^2(k^\vartheta)^2\kappa_2^2r^2 &&- \alpha^3(k^t)^2(k^\vartheta)^4r^6\\
&- \alpha^3(k^t)^2(k^\vartheta)^2\kappa_1^2r^2 &&+ \alpha^2\beta^2(k^\varphi)^4\kappa_1^2r^4 &&+ 2\alpha^2\beta(k^\varphi)^2(k^r)^2(k^t)^2r^4\\
&+ 2\alpha^2\beta(k^\varphi)^2(k^\vartheta)^2\kappa_1^2r^4 &&- 2\alpha^2\beta(k^r)^2(k^t)^2\kappa_2^2 &&- 2\alpha^2(k^r)^2(k^t)^2(k^\vartheta)^2r^4\\
&+ \alpha^2(k^\vartheta)^4\kappa_1^2r^4 &&+ \alpha\beta^2(k^\varphi)^4(k^r)^2r^6 &&- \alpha\beta^2(k^\varphi)^2(k^r)^2\kappa_2^2r^2\\
&+ 2\alpha\beta(k^\varphi)^2(k^r)^2(k^\vartheta)^2r^6 &&- \alpha\beta(k^\varphi)^2(k^r)^2\kappa_1^2r^2 &&+ \alpha\beta(k^r)^2(k^\vartheta)^2\kappa_2^2r^2\\
&+ \alpha(k^r)^2(k^\vartheta)^4r^6 &&+ \alpha(k^r)^2(k^\vartheta)^2\kappa_1^2r^2 &&- \beta(k^\varphi)^2(k^r)^4r^4\\
&+ \beta(k^r)^4\kappa_2^2 &&+ (k^r)^4(k^\vartheta)^2r^4
\end{aligned}
$$

$$
\begin{aligned}
R_{\text{denom}} = &+ \alpha^4\beta(k^\varphi)^2(k^t)^4 &&- \alpha^4(k^t)^4(k^\vartheta)^2 &&+ \alpha^3\beta^2(k^\varphi)^4(k^t)^2r^2\\
&+ 2\alpha^3\beta(k^\varphi)^2(k^t)^2(k^\vartheta)^2r^2 &&+ \alpha^3(k^t)^2(k^\vartheta)^4r^2 &&- 2\alpha^2\beta(k^\varphi)^2(k^r)^2(k^t)^2\\
&+ 2\alpha^2(k^r)^2(k^t)^2(k^\vartheta)^2 &&- \alpha\beta^2(k^\varphi)^4(k^r)^2r^2 &&- 2\alpha\beta(k^\varphi)^2(k^r)^2(k^\vartheta)^2r^2\\
&- \alpha(k^r)^2(k^\vartheta)^4r^2 &&+ \beta(k^\varphi)^2(k^r)^4 &&- (k^r)^4(k^\vartheta)^2
\end{aligned}
$$

For the ϑ-component:

$$\theta_{\text{nom}} = k^\varphi\kappa_2(\alpha^2\beta(k^t)^2 + \alpha\beta^2(k^\varphi)^2r^2 + \alpha\beta(k^\vartheta)^2r^2 - \beta(k^r)^2)$$

$$
\begin{aligned}
\Xi_\theta = &- \alpha^4\beta(k^\varphi)^2(k^t)^4r^4 &&+ \alpha^4\beta(k^t)^4\kappa_2^2 &&+ \alpha^4(k^t)^4(k^\vartheta)^2r^4\\
&- \alpha^3\beta^2(k^\varphi)^4(k^t)^2r^6 &&+ \alpha^3\beta^2(k^\varphi)^2(k^t)^2\kappa_2^2r^2 &&- 2\alpha^3\beta(k^\varphi)^2(k^t)^2(k^\vartheta)^2r^6\\
&+ \alpha^3\beta(k^\varphi)^2(k^t)^2\kappa_1^2r^2 &&- \alpha^3\beta(k^t)^2(k^\vartheta)^2\kappa_2^2r^2 &&- \alpha^3(k^t)^2(k^\vartheta)^4r^6\\
&- \alpha^3(k^t)^2(k^\vartheta)^2\kappa_1^2r^2 &&+ \alpha^2\beta^2(k^\varphi)^4\kappa_1^2r^4 &&+ 2\alpha^2\beta(k^\varphi)^2(k^r)^2(k^t)^2r^4\\
&+ 2\alpha^2\beta(k^\varphi)^2(k^\vartheta)^2\kappa_1^2r^4 &&- 2\alpha^2\beta(k^r)^2(k^t)^2\kappa_2^2 &&- 2\alpha^2(k^r)^2(k^t)^2(k^\vartheta)^2r^4\\
&+ \alpha^2(k^\vartheta)^4\kappa_1^2r^4 &&+ \alpha\beta^2(k^\varphi)^4(k^r)^2r^6 &&- \alpha\beta^2(k^\varphi)^2(k^r)^2\kappa_2^2r^2\\
&+ 2\alpha\beta(k^\varphi)^2(k^r)^2(k^\vartheta)^2r^6 &&- \alpha\beta(k^\varphi)^2(k^r)^2\kappa_1^2r^2 &&+ \alpha\beta(k^r)^2(k^\vartheta)^2\kappa_2^2r^2\\
&+ \alpha(k^r)^2(k^\vartheta)^4r^6 &&+ \alpha(k^r)^2(k^\vartheta)^2\kappa_1^2r^2 &&- \beta(k^\varphi)^2(k^r)^4r^4\\
&+ \beta(k^r)^4\kappa_2^2 &&+ (k^r)^4(k^\vartheta)^2r^4
\end{aligned}
$$

$$\begin{aligned}\theta_{\text{denom}} = &+ \alpha^2\beta(k^\varphi)^2(k^t)^2 \quad - \alpha^2(k^t)^2(k^\vartheta)^2 + \alpha\beta^2(k^\varphi)^4r^2 \\ &+ 2\alpha\beta(k^\varphi)^2(k^\vartheta)^2r^2 + \alpha(k^\vartheta)^4r^2 \quad - \beta(k^\varphi)^2(k^r)^2 \\ &+ (k^r)^2(k^\vartheta)^2\end{aligned}$$

For the φ-component:

$$\phi_{\text{nom}} = -k^\vartheta\kappa_2(-\alpha^2(k^t)^2 + \alpha\beta(k^\varphi)^2r^2 + \alpha(k^\vartheta)^2r^2 + (k^r)^2)$$

$$\begin{aligned}\Xi_\phi = &- \alpha^4\beta(k^\varphi)^2(k^t)^4r^4 \quad + \alpha^4\beta(k^t)^4\kappa_2^2 \quad + \alpha^4(k^t)^4(k^\vartheta)^2r^4 \\ &- \alpha^3\beta^2(k^\varphi)^4(k^t)^2r^6 \quad + \alpha^3\beta^2(k^\varphi)^2(k^t)^2\kappa_2^2r^2 - 2\alpha^3\beta(k^\varphi)^2(k^t)^2(k^\vartheta)^2r^6 \\ &+ \alpha^3\beta(k^\varphi)^2(k^t)^2\kappa_1^2r^2 \quad - \alpha^3\beta(k^t)^2(k^\vartheta)^2\kappa_2^2r^2 \quad - \alpha^3(k^t)^2(k^\vartheta)^4r^6 \\ &- \alpha^3(k^t)^2(k^\vartheta)^2\kappa_1^2r^2 \quad + \alpha^2\beta^2(k^\varphi)^4\kappa_1^2r^4 \quad + 2\alpha^2\beta(k^\varphi)^2(k^r)^2(k^t)^2r^4 \\ &+ 2\alpha^2\beta(k^\varphi)^2(k^\vartheta)^2\kappa_1^2r^4 \quad - 2\alpha^2\beta(k^r)^2(k^t)^2\kappa_2^2 \quad - 2\alpha^2(k^r)^2(k^t)^2(k^\vartheta)^2r^4 \\ &+ \alpha^2(k^\vartheta)^4\kappa_1^2r^4 \quad + \alpha\beta^2(k^\varphi)^4(k^r)^2r^6 \quad - \alpha\beta^2(k^\varphi)^2(k^r)^2\kappa_2^2r^2 \\ &+ 2\alpha\beta(k^\varphi)^2(k^r)^2(k^\vartheta)^2r^6 - \alpha\beta(k^\varphi)^2(k^r)^2\kappa_1^2r^2 \quad + \alpha\beta(k^r)^2(k^\vartheta)^2\kappa_2^2r^2 \\ &+ \alpha(k^r)^2(k^\vartheta)^4r^6 \quad + \alpha(k^r)^2(k^\vartheta)^2\kappa_1^2r^2 \quad - \beta(k^\varphi)^2(k^r)^4r^4 \\ &+ \beta(k^r)^4\kappa_2^2 \quad + (k^r)^4(k^\vartheta)^2r^4\end{aligned}$$

$$\begin{aligned}\phi_{\text{denom}} = &+ \alpha^2\beta(k^\varphi)^2(k^t)^2 \quad - \alpha^2(k^t)^2(k^\vartheta)^2 + \alpha\beta^2(k^\varphi)^4r^2 \\ &+ 2\alpha\beta(k^\varphi)^2(k^\vartheta)^2r^2 + \alpha(k^\vartheta)^4r^2 \quad - \beta(k^\varphi)^2(k^r)^2 + (k^r)^2(k^\vartheta)^2\end{aligned}$$

A.3.2 Polarization vector in Kerr spacetime

In this section, the exact formula for the polarization vector f^μ is given, as defined in section 6.3.3. Recall the determining equation for the components of the polarization vector at any point in spacetime, relative to the tangent of the worldline

$$\begin{aligned}
\kappa_1 &= r\left(k^t f^r - k^r f^t\right) + ra\sin^2\vartheta\left(k^r f^\varphi - k^\varphi f^r\right) \\
&\quad - a\cos\vartheta\sin\vartheta\left[(r^2+a^2)\left(k^\varphi f^\vartheta - k^\vartheta f^\varphi\right) - a\left(k^t f^\vartheta - k^\vartheta f^t\right)\right] , \qquad \text{(A.73)} \\
\kappa_2 &= -a\cos\vartheta\left(k^t f^r - k^r f^t\right) - a^2\sin^2\vartheta\cos\vartheta\left(k^r f^\varphi - k^\varphi f^r\right) \\
&\quad - r\sin\vartheta\left[(r^2+a^2)\left(k^\varphi f^\vartheta - k^\vartheta f^\varphi\right) - a\left(k^t f^\vartheta - k^\vartheta f^t\right)\right] , \qquad \text{(A.74)} \\
1 &= -g_{tt}\left(f^t\right)^2 + g_{t\varphi} f^t f^\varphi + g_{rr}\left(f^r\right)^2 + g_{\vartheta\vartheta}\left(f^\vartheta\right)^2 + g_{\varphi\varphi}\left(f^\varphi\right)^2 , \qquad \text{(A.75)} \\
0 &= -g_{tt} f^t k^t + g_{t\varphi}\left(f^t k^\varphi + f^\varphi k^t\right) + g_{rr} f^r k^r + g_{\vartheta\vartheta} f^\vartheta k^\vartheta + g_{\varphi\varphi} f^\varphi k^\varphi , \qquad \text{(A.76)}
\end{aligned}$$

where $\kappa_{1,\,2}$ are the real and imaginary parts of the Penrose-Walker constant, and $g_{\mu\nu}$ are the components of the metric tensor of the Kerr solution, see Eq. (6.1). The computations of the components of the polarization vector become quite unhandy, as this set of equations is non-linear. This results in the following components of f^μ:

$$\begin{aligned}
f^t &= C_{38} \pm \sqrt{C_{39}} , \qquad \text{(A.77)} \\
f^r &= C_{40} \pm \sqrt{C_{41}} , \qquad \text{(A.78)} \\
f^\vartheta &= C_{36} \pm \sqrt{C_{37}} , \qquad \text{(A.79)} \\
f^\varphi &= C_{42} \pm \sqrt{C_{43}} , \qquad \text{(A.80)}
\end{aligned}$$

where the terms, in order of appearance, are defined as follows:

$$\begin{aligned}
C_{36} =& \frac{-2C_{27}C_{28}C_9 - 2C_{29}C_{30}C_7 - 2C_{31}C_{32}C_5 - C_6\left(C_{27}C_{32} + C_{28}C_{31}\right)}{2C_{28}^2C_9 + 2C_{30}^2C_7 + 2C_{30}C_{32}C_6 + 2C_{32}^2C_5 + 2C_8} , \\
C_{37} =& \frac{\left(2C_{27}C_{28}C_9 + 2C_{29}C_{30}C_7 + 2C_{31}C_{32}C_5 + C_6\left(C_{27}C_{32} + C_{28}C_{31}\right)\right)^2}{4C_{28}^2C_9 + 4C_{30}^2C_7 + 4C_{30}C_{32}C_6 + 4C_{32}^2C_5 + 4C_8} \\
& - \frac{C_{27}^2C_9 + C_{27}C_{31}C_6 + C_{29}^2C_7 + C_{31}^2C_5 - 1}{C_{28}^2C_9 + C_{30}^2C_7 + C_{30}C_{32}C_6 + C_{32}^2C_5 + C_8} , \\
C_{38} =& C_{31} + \frac{C_{32}\left(-2C_{27}C_{28}C_9 - 2C_{29}C_{30}C_7 - 2C_{31}C_{32}C_5 - C_6\left(C_{27}C_{32} + C_{28}C_{31}\right)\right)}{2C_{28}^2C_9 + 2C_{30}^2C_7 + 2C_{30}C_{32}C_6 + 2C_{32}^2C_5 + 2C_8} , \\
C_{39} =& \frac{C_{32}^2\left(2C_{27}C_{28}C_9 + 2C_{29}C_{30}C_7 + 2C_{31}C_{32}C_5 + C_6\left(C_{27}C_{32} + C_{28}C_{31}\right)\right)^2}{4C_{28}^2C_9 + 4C_{30}^2C_7 + 4C_{30}C_{32}C_6 + 4C_{32}^2C_5 + 4C_8} \\
& - \frac{C_{32}^2C_{27}^2C_9 + C_{27}C_{31}C_6 + C_{29}^2C_7 + C_{31}^2C_5 - 1}{C_{28}^2C_9 + C_{30}^2C_7 + C_{30}C_{32}C_6 + C_{32}^2C_5 + C_8} , \\
C_{40} =& C_{29} + \frac{C_{30}\left(-2C_{27}C_{28}C_9 - 2C_{29}C_{30}C_7 - 2C_{31}C_{32}C_5 - C_6\left(C_{27}C_{32} + C_{28}C_{31}\right)\right)}{2C_{28}^2C_9 + 2C_{30}^2C_7 + 2C_{30}C_{32}C_6 + 2C_{32}^2C_5 + 2C_8} ,
\end{aligned}$$

with

$$
\begin{aligned}
C_{27} &= \left(-C_{14}C_{18}\kappa_1 - C_{15}\kappa_1 + \kappa_2\left(C_{10}C_{18} + C_{11}\right)\right) , \\
&\quad \cdot \Big(-C_{14}\left(C_{18}\left(C_{10}C_{20} + C_{13}\right) - C_{20}\left(C_{10}C_{18} + C_{11}\right)\right) \\
&\qquad - C_{15}\left(C_{10}C_{20} + C_{13}\right) + C_{17}\left(C_{10}C_{18} + C_{11}\right)\Big)^{-1} , \\
C_{28} &= \frac{-C_{10}C_{15}C_{19} + C_{10}C_{16}C_{18} + C_{11}C_{14}C_{19} + C_{11}C_{16} - C_{12}C_{14}C_{18} - C_{12}C_{15}}{C_{10}C_{15}C_{20} - C_{10}C_{17}C_{18} - C_{11}C_{14}C_{20} - C_{11}C_{17} + C_{13}C_{14}C_{18} + C_{13}C_{15}} \\
C_{29} &= \frac{C_{10}C_{20}\kappa_2 + C_{13}\kappa_2 - C_{14}C_{20}\kappa_1 - C_{17}\kappa_1}{C_{10}C_{15}C_{20} - C_{10}C_{17}C_{18} - C_{11}C_{14}C_{20} - C_{11}C_{17} + C_{13}C_{14}C_{18} + C_{13}C_{15}} , \\
C_{30} &= \frac{-C_{10}C_{16}C_{20} + C_{10}C_{17}C_{19} + C_{12}C_{14}C_{20} + C_{12}C_{17} - C_{13}C_{14}C_{19} - C_{13}C_{16}}{C_{10}C_{15}C_{20} - C_{10}C_{17}C_{18} - C_{11}C_{14}C_{20} - C_{11}C_{17} + C_{13}C_{14}C_{18} + C_{13}C_{15}} , \\
C_{31} &= \frac{-C_{11}C_{20}\kappa_2 + C_{13}C_{18}\kappa_2 + C_{15}C_{20}\kappa_1 - C_{17}C_{18}\kappa_1}{C_{10}C_{15}C_{20} - C_{10}C_{17}C_{18} - C_{11}C_{14}C_{20} - C_{11}C_{17} + C_{13}C_{14}C_{18} + C_{13}C_{15}} , \\
C_{32} &= \frac{C_{11}C_{16}C_{20} - C_{11}C_{17}C_{19} - C_{12}C_{15}C_{20} + C_{12}C_{17}C_{18} + C_{13}C_{15}C_{19} - C_{13}C_{16}C_{18}}{C_{10}C_{15}C_{20} - C_{10}C_{17}C_{18} - C_{11}C_{14}C_{20} - C_{11}C_{17} + C_{13}C_{14}C_{18} + C_{13}C_{15}} .
\end{aligned}
$$

The remaining constants are functions of the metric, or directly translate from the Penrose-Walker constants; in particular,

$$
\begin{aligned}
C_{20} &= -\frac{g_{\varphi\varphi}k^{\varphi} + g_{t\varphi}k^{t}}{-g_{tt}k^{t} + g_{t\varphi}k^{\varphi}} , & C_{19} &= -\frac{g_{\vartheta\vartheta}f^{\vartheta}}{-g_{tt}k^{t} + g_{t\varphi}k^{\varphi}} , \\
C_{18} &= -\frac{g_{rr}f^{r}}{-g_{tt}k^{t} + g_{t\varphi}k^{\varphi}} , & C_{17} &= -a^2\cos\vartheta\sin^2\vartheta k^{r} + (r^2+a^2)r\sin\vartheta k^{\vartheta} , \\
C_{16} &= -(r^2+a^2)r\sin\vartheta k^{\varphi} + ra\sin\vartheta k^{t} , & C_{15} &= -a\cos\vartheta k^{t} + a^2\cos\vartheta\sin^2\vartheta k^{\varphi} , \\
C_{14} &= a\cos\vartheta k^{r} - ra\sin\vartheta k^{\vartheta} , & C_{13} &= ra\sin^2\vartheta k^{r} + (r^2+a^2)a\cos\vartheta\sin\vartheta k^{\vartheta} , \\
C_{12} &= -a\cos\vartheta\sin\vartheta\left[(r^2+a^2)k^{\varphi} - ak^{t}\right] , & C_{11} &= rk^{t} - ra\sin^2\vartheta k^{\varphi} , \\
C_{10} &= -rk^{r} - a^2\cos\vartheta\sin\vartheta k^{\vartheta} , & C_{9} &= g_{\varphi\varphi} , \\
C_{8} &= g_{\vartheta\vartheta} , & C_{7} &= g_{rr} , \\
C_{6} &= 2g_{t\varphi} , & C_{5} &= -g_{tt} , \\
C_{4} &= g_{\varphi\varphi}k^{\varphi} + g_{t\varphi}k^{t} , & C_{3} &= g_{\vartheta\vartheta}k^{\vartheta} , \\
C_{2} &= g_{rr}k^{r} , & C_{1} &= -g_{tt}k^{t} + g_{t\varphi}k^{\varphi} ,
\end{aligned}
$$

Bibliography

[1] A. M. Ghez et al. “Measuring distance and properties of the Milky Way’s central supermassive black hole with stellar orbits”. In: *The Astrophysical Journal* 689 (2 Dec. 2008), pp. 1044–1062. issn: 0004-637X. doi: 10.1086/592738.

[2] S. Gillessen et al. “Monitoring stellar orbits around the massive black hole in the galactic center”. In: *The Astrophysical Journal* 692.2 (2009), pp. 1075–1109. doi: 10.1088/0004-637x/692/2/1075. url: https://doi.org/10.10882F0004-637x2F6922F22F1075.

[3] The Event Horizon Telescope Collaboration. “First M87 Event Horizon Telescope results. IV. Imaging the central supermassive black hole”. In: (June 2019). doi: 10.3847/2041-8213/ab0e85.

[4] The Event Horizon Telescope Collaboration. “First Sagittarius A* Event Horizon Telescope results. III. Imaging of the galactic center supermassive black hole”. In: *The Astrophysical Journal Letters* 930.L14 (2022). url: https://doi.org/10.3847/2041-8213/ac6429.

[5] F. Meyer et al., eds. *Theory of accretion disks*. Springer Netherlands, 1989. isbn: 978-94-010-6958-8. doi: 10.1007/978-94-009-1037-9.

[6] M. A. Abramowicz et al. “X-ray variability power spectra of active galactic nuclei.” In: *Astronomy and Astrophysics* 245 (May 1991), p. 454.

[7] A. V. Mangalam and P. J. Wiita. “Accretion disk models for optical and ultraviolet microvariability in Active Galactic Nuclei”. In: *The Astrophysical Journal* 406 (Apr. 1993), p. 420. doi: 10.1086/172453.

[8] Werner B., ed. *Neutron stars and pulsars*. Vol. 357. Springer Berlin Heidelberg, 2009. isbn: 978-3-540-76964-4. doi: 10.1007/978-3-540-76965-1.

[9] W. Baade and F. Zwicky. “On Super-novae”. In: *Proceedings of the National Academy of Science* 20.5 (May 1934), pp. 254–259. doi: 10.1073/pnas.20.5.254.

[10] A. Hewish et al. “Observation of a rapidly pulsating radio source”. In: *Nature* 217 (5130 Feb. 1968), pp. 709–713. issn: 0028-0836. doi: 10.1038/217709a0.

[11] J. R. Oppenheimer and G. M. Volkoff. “On massive neutron cores”. In: *Phys. Rev.* 55 (4 1939), pp. 374–381. doi: 10.1103/PhysRev.55.374. url: https://link.aps.org/doi/10.1103/PhysRev.55.374.

[12] I. Bombaci. “The maximum mass of a neutron star”. In: *Astronomy and Astrophysics* 305 (Jan. 1996), p. 871.

[13] L. Rezzolla, E. R. Most, and L. R. Weih. “Using gravitational-wave observations and quasi-universal relations to constrain the maximum mass of neutron stars”. In: *The Astrophysical Journal* 852.2 (2018), p. L25. doi: 10.3847/2041-8213/aaa401. url: https://doi.org/10.38472F2041-82132Faaa401.

[14] L. Burderi et al. “Evolution of binary millisecond pulsars with light companions: the case of PSR J1748-2446ad”. In: *36th COSPAR Scientific Assembly* 36 (Jan. 2006), p. 1812.

[15] K. Gendreau and Z. Arzoumanian. "Searching for a pulse". In: *Nature Astronomy* 1 (12 Dec. 2017), pp. 895–895. issn: 2397-3366. doi: 10.1038/s41550-017-0301-3.

[16] S. Bogdanov et al. "Constraining the neutron star mass–radius relation and dense matter equation of state with NICER . II. Emission from hot spots on a rapidly rotating neutron star". In: *The Astrophysical Journal* 887 (1 Dec. 2019), p. L26. issn: 20418213. doi: 10.3847/2041-8213/ab5968.

[17] Slavko B. et al. "Constraining the neutron star mass–radius relation and dense matter equation of state with NICER. III. Model description and verification of parameter estimation codes". In: *The Astrophysical Journal Letters* 914.1 (2021), p. L15. doi: 10.3847/2041-8213/abfb79. url: https://doi.org/10.3847%2F2041-8213%2Fabfb79.

[18] S.A. Kaplan. "On circular orbits in Einsteinian gravitation theory". In: *ZhETF Pisma Redaktsiiu* 19 (Apr. 1949), pp. 951–952.

[19] J. M. Bardeen, W. H. Press, and S. A. Teukolsky. "Rotating black holes: Locally nonrotating frames, energy extraction, and scalar synchrotron radiation". In: *The Astrophysical Journal* 178 (1972), p. 347. issn: 0004-637X. doi: 10.1086/151796. url: http://adsabs.harvard.edu/doi/10.1086/151796.

[20] R. Ruffini and J. A. Wheeler. "Relativistic cosmology and space platforms". In: *ESRO* (1971). url: https://inis.iaea.org/search/search.aspx?orig_q=RN:3024932.

[21] P. I. Jefremov, O. Y. Tsupko, and G. S. Bisnovatyi-Kogan. "Innermost stable circular orbits of spinning test particles in Schwarzschild and Kerr space-times". In: *Physical Review D* 91 (12 Mar. 2015), p. 124030. issn: 1550-7998. doi: 10.1103/PhysRevD.91.124030. url: https://link.aps.org/doi/10.1103/PhysRevD.91.124030http://arxiv.org/abs/1503.07060.

[22] R. Wald. "Gravitational spin interaction". In: *Physical Review D* 6 (2 1972), pp. 406–413. issn: 05562821. doi: 10.1103/PhysRevD.6.406.

[23] W. G. Dixon. "Dynamics of extended bodies in general relativity. I. Momentum and angular momentum". In: *Proceedings of the Royal Society of London. A. Mathematical and Physical Sciences* 314.1519 (Jan. 1970), pp. 499–527. doi: 10.1098/rspa.1970.0020. url: https://doi.org/10.1098/rspa.1970.0020.

[24] J. Ehlers and E. Rudolph. "Dynamics of extended bodies in general relativity center-of-mass description and quasirigidity". In: *General Relativity and Gravitation* 8 (3 1977), pp. 197–217. issn: 00017701. doi: 10.1007/BF00763547.

[25] A. Einstein, L. Infeld, and B. Hoffmann. "The gravitational equations and the problem of motion". In: *The Annals of Mathematics* 39.1 (Jan. 1938), p. 65. doi: 10.2307/1968714. url: https://doi.org/10.2307/1968714.

[26] V.A. Fock. "On motion of finite masses in general relativity". In: *J. Phys. (Moscow)* 1.2 (1939). url: https://www.scopus.com/inward/record.uri?eid=2-s2.0-0004380136&partnerID=40&md5=7a27282e4b13bfe7ef63cc4e9bab6f55.

[27] A. Papapetrou. "Spinning test-particles in general relativity. I". In: *Proceedings of the Royal Society of London. Series A. Mathematical and Physical Sciences* 209.1097 (Oct. 1951), pp. 248–258. doi: 10.1098/rspa.1951.0200. url: https://doi.org/10.1098/rspa.1951.0200.

[28] M. Mathisson. "Neue Mechanik materieller Systeme". In: *Acta Phys. Polon.* 6 (1937), pp. 163–2900.

[29] F. A. E. Pirani. "Invariant formulation of gravitational radiation theory". In: *Physical Review* 105.3 (Feb. 1957), pp. 1089–1099. doi: 10.1103/physrev.105.1089. url: https://doi.org/10.1103/physrev.105.1089.

[30] J. Frenkel. "Die Elektrodynamik des rotierenden Elektrons". In: *Zeitschrift fuer Physik* 37.4-5 (Apr. 1926), pp. 243–262. doi: 10.1007/bf01397099. url: https://doi.org/10.1007/bf01397099.

[31] W. G. Dixon. "The definition of multipole moments for extended bodies". In: *General Relativity and Gravitation* 4.3 (June 1973), pp. 199–209. doi: 10.1007/bf02412488. url: https://doi.org/10.1007/bf02412488.

[32] W. G. Dixon and P. Trans. "Dynamics of extended bodies in general relativity III. Equations of motion". In: *Philosophical Transactions of the Royal Society of London. Series A, Mathematical and Physical Sciences* 277 (1264 1974), pp. 59–119. issn: 0080-4614. doi: 10.1098/rsta.1974.0046.

[33] W. Tulczyjew. "Motion of multipole particles in general relativity theory". In: *Acta Physica Polonia* 18 (1959), pp. 393 –403.

[34] C. Møller. *On the definition of the centre of Gravity of an arbitrary closed system in the theory of relativity*. Dublin, Dublin Institute for Advanced Studies, 1949.

[35] T. Eguchi, P. Gilkey, and A. Hanson. "Gravitation, gauge theories And differential geometry". In: *Physics Reports* 66 (Nov. 1980), pp. 213–393. doi: 10.1016/0370-1573(80)90130-1.

[36] C. W. Misner, K. S. Thorne, and J. A. Wheeler. *Gravitation*. 24. print. XXVI, 1279 S : Ill., graph. Darst. New York, NY: Freeman, 2002. isbn: 0716703343 and 0716703440 and 97807167034410. url: https://suche.suub.uni-bremen.de/peid=B37411870.

[37] T. Tanaka et al. "Gravitational waves from a spinning particle in circular orbits around a rotating black hole". In: *Physical Review D - Particles, Fields, Gravitation and Cosmology* 54 (6 1996), pp. 3762–3777. issn: 15502368. doi: 10.1103/PhysRevD.54.3762.

[38] Arne Grenzebach, Volker Perlick, and Claus Lämmerzahl. "Photon regions and shadows of Kerr-Newman-NUT black holes with a cosmological constant". In: *Physical Review D* 89.12 (June 2014). doi: 10.1103/physrevd.89.124004. url: https://doi.org/10.1103%2Fphysrevd.89.124004.

[39] A. Čadež, C. Fanton, and M. Calvani. "Line emission from accretion discs around black holes: The analytic approach". In: *New Astronomy* 3 (8 1998), pp. 647–654. issn: 13841076. doi: 10.1016/S1384-1076(98)00035-9.

[40] E. Kravchenko et al. "Linear polarization in the nucleus of M87 at 7 mm and 1.3 cm". In: *Astronomy and Astrophysics* 637, L6 (May 2020), p. L6. doi: 10.1051/0004-6361/201937315. arXiv: 2006.07059 [astro-ph.GA].

[41] Y. Tsunetoe et al. "Diverse polarimetric features of AGN Jets from various viewing angles: Towards a unified view". In: *Galaxies* 10.5 (Oct. 2022), p. 103. doi: 10.3390/galaxies10050103. arXiv: 2210.12162 [astro-ph.HE].

[42] Y. Chen et al. "Stringent axion constraints with Event Horizon Telescope polarimetric measurements of M87⋆". In: *Nature Astronomy* 6 (Mar. 2022), pp. 592–598. doi: 10.1038/s41550-022-01620-3. arXiv: 2105.04572 [hep-ph].

[43] Henric Krawczynski et al. "Polarized x-rays constrain the disk-jet geometry in the black hole x-ray binary Cygnus X-1". In: *Science* 378.6620 (2022), pp. 650–654. doi: 10.1126/science.add5399. url: https://doi.org/10.1126%2Fscience.add5399.

[44] M. Walker and R. Penrose. "On quadratic first integrals of the geodesic equations for Type {22} spacetimes". In: *Commun. math. Phys* 18 (1970), p. 19.

[45] P. A. Connors and R. F. Stark. "Observable gravitational effects on polarised radiation coming from near a black hole". In: *Nature* 269 (5624 Sept. 1977), pp. 128–129. issn: 0028-0836. doi: 10.1038/269128a0. url: http://www.nature.com/articles/269128a0.

[46] E. Himwich et al. "Universal polarimetric signatures of the black hole photon ring". In: *Physical Review D* 101 (8 Apr. 2020). issn: 24700029. doi: 10.1103/PhysRevD.101.084020.

[47] B. C. Bromley, K. Chen, and W. A. Miller. "Line emission from an accretion disk around a rotating black hole: Toward a measurement of frame dragging". In: *The Astrophysical Journal* 475 (1 1997), pp. 57–64. issn: 0004-637X. doi: 10.1086/303505.

[48] C. A. Haswell. *Transiting exoplanets*. Cambridge University Press, 2010.

[49] A. Unsöld and R. B. Lindsay. "Der neue Kosmos". In: *Physics Today* 21 (10 Oct. 1968), pp. 71–72. issn: 0031-9228. doi: 10.1063/1.3034553. url: http://physicstoday.scitation.org/doi/10.1063/1.3034553.

[50] R. W. Lindquist. "Relativistic transport theory". In: *Annals of Physics* 37.3 (May 1966), pp. 487–518. doi: 10.1016/0003-4916(66)90207-7. url: https://doi.org/10.1016/0003-4916(66)90207-7.

[51] S. Chandrasekhar. "Ellipsoidal figures of equilibrium-an historical account". In: *Communications on Pure and Applied Mathematics* 20 (2 Sept. 1967), pp. 251–265. issn: 00103640. doi: 10.1002/cpa.3160200203.

[52] J. B. Griffiths and J. Podolsky. *Exact space-times in Einstein's General Relativity*. Cambridge Monographs on Mathematical Physics. Cambridge University Press, 2009. doi: 10.1017/CBO9780511635397.

[53] J. T. Jebsen. "On the general spherically symmetric solutions of Einstein's gravitational equations in vacuo". In: *General Relativity and Gravitation* 37.12 (Nov. 2005), pp. 2253–2259. doi: 10.1007/s10714-005-0168-y. url: https://doi.org/10.1007/s10714-005-0168-y.

[54] G. D. Birkhoff and R. E. Langer. *Relativity and modern physics*. 1923.

[55] R. C. Henry. "Kretschmann scalar for a Kerr-Newman black hole". In: *The Astrophysical Journal* 535 (1 May 2000), pp. 350–353. issn: 0004-637X. doi: 10.1086/308819.

[56] A. S. Eddington. "A comparison of Whitehead's and Einstein's formulae". In: *Nature* 113 (2832 Feb. 1924), pp. 192–192. issn: 0028-0836. doi: 10.1038/113192a0.

[57] D. Finkelstein. "Past-Future asymmetry of the gravitational field of a point particle". In: *Phys. Rev.* 110 (4 1958), pp. 965–967. doi: 10.1103/PhysRev.110.965. url: https://link.aps.org/doi/10.1103/PhysRev.110.965.

[58] R. Penrose. "Gravitational collapse and space-time singularities". In: *Phys. Rev. Lett.* 14 (3 1965), pp. 57–59. doi: 10.1103/PhysRevLett.14.57. url: https://link.aps.org/doi/10.1103/PhysRevLett.14.57.

[59] B. Carter. "Hamilton-Jacobi and Schrodinger separable solutions of Einstein's equations". In: *Communications in Mathematical Physics* 10 (4 Dec. 1968), pp. 280–310. issn: 0010-3616. doi: 10.1007/BF03399503.

[60] R. Penrose. "The apparent shape of a relativistically moving sphere". In: *Mathematical Proceedings of the Cambridge Philosophical Society* 55 (1 1959), pp. 137–139. issn: 14698064. doi: 10.1017/S0305004100033776.

[61] R. Narayan et al. “The polarized image of a Synchrotron-emitting ring of gas orbiting a black hole”. In: *Astrophysical Journal* 912.1, 35 (May 2021), p. 35. doi: 10.3847/1538-4357/abf117. arXiv: 2105.01804 [astro-ph.HE].

[62] R. P. Kerr. “Gravitational field of a spinning mass as an example of algebraically special metrics”. In: *Physical Review Letters* 11 (5 Sept. 1963), pp. 237–238. issn: 0031-9007. doi: 10.1103/PhysRevLett.11.237. url: https://link.aps.org/doi/10.1103/PhysRevLett.11.237.

[63] J. Lense and H. Thirring. “Über den Einfluß der Eigenrotation der Zentralkörper auf die Bewegung der Planeten und Monde nach der Einsteinschen Gravitationstheorie”. In: *Physikalische Zeitschrift* 19 (Jan. 1918), p. 156.

[64] B. Carter. “Global structure of the Kerr family of gravitational fields”. In: *Phys. Rev.* 174 (5 1968), pp. 1559–1571. doi: 10.1103/PhysRev.174.1559. url: https://link.aps.org/doi/10.1103/PhysRev.174.1559.

[65] X. Yang and J. Wang. “YNOGK: A new public code for calculating null geodesics in the Kerr spacetime”. In: *Astrophysical Journal* 6 (2009 2013), p. 207. doi: 10.1088/0067-0049/207/1/6.

[66] C. Cederbaum. “Geometry and topology of the Kerr photon region in the phase space”. In: *General Relativity and Gravitation* (Apr. 2019). doi: 10.1007/s10714-019-2561-y. url: http://arxiv.org/abs/1904.00916http://dx.doi.org/10.1007/s10714-019-2561-y.

[67] C. R. Cramer. “Using the uncharged Kerr black hole as a gravitational mirror”. In: *General Relativity and Gravitation* (Oct. 1995). doi: 10.1023/A:1018878515046. url: http://arxiv.org/abs/gr-qc/9510053http://dx.doi.org/10.1023/A:1018878515046.

[68] S. Chandrasekhar. *The mathematical theory of black holes*. Springer Netherlands, 1984, pp. 5–26. doi: 10.1007/978-94-009-6469-3_2.

[69] H. Quevedo, S. Toktarbay, and A. Yerlan. “Quadrupolar gravitational fields described by the $q-$metric”. In: *International Journal of Mathematics and Physics* (Oct. 2013). url: http://arxiv.org/abs/1310.5339.